

AFAPL-TR-76-48

Volume II

120

**INVESTIGATION OF ROTATING STALL  
PHENOMENA IN AXIAL FLOW COMPRESSORS  
Volume II - INVESTIGATION OF ROTOR-  
STATOR INTERACTION NOISE AND LIFTING  
SURFACE THEORY FOR A ROTOR**

AD A030070

*CALSPAN CORPORATION  
P.O. BOX 285  
BUFFALO, NEW YORK 14221*

D.D.C.  
SEP 24 1976  
RECEIVED

JUNE 1976

TECHNICAL REPORT AFAPL-TR-76-48 Volume II  
FINAL REPORT FOR PERIOD 1 MAY 1973 - 31 MAY 1976

Approved for public release; distribution unlimited

AIR FORCE AERO-PROPULSION LABORATORY  
AIR FORCE WRIGHT AERONAUTICAL LABORATORIES  
AIR FORCE SYSTEMS COMMAND  
WRIGHT-PATTERSON AIR FORCE BASE, OHIO 45433

NOTICE

When Government drawings, specifications, or other data are used for any purpose other than in connection with a definitely related Government procurement operation, the United States Government thereby incurs no responsibility nor any obligation whatsoever; and the fact that the government may have formulated, furnished, or in any way supplied the said drawings, specifications, or other data, is not to be regarded by implication or otherwise as in any manner licensing the holder or any other person or corporation, or conveying any rights or permission to manufacture, use, or sell any patented invention that may in any way be related thereto.

This final report was submitted by the Calspan Corporation, under Contract F33615-73-C-2046. The effort was sponsored by the Air Force Aero-Propulsion Laboratory, Air Force Systems Command, Wright-Patterson AFB, Ohio under Project 3066, Task 306603, and Work Unit 30660334 with Mr. Marvin A. Stibich, AFAPL/TBC, as Project Engineer in charge. Dr. Gary R. Ludwig of the Calspan Corporation was technically responsible for the work.

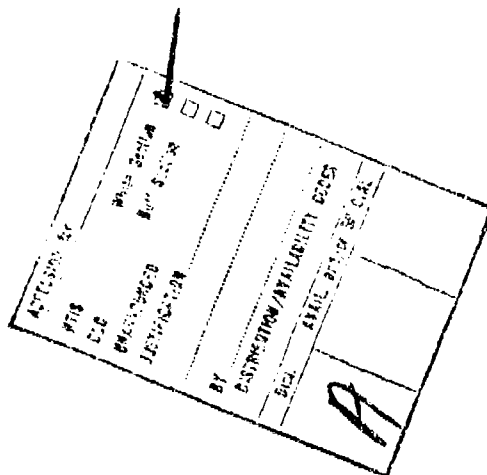
This report has been reviewed by the Information Office, ASD/OIP, and is releasable to the National Technical Information Service (NTIS). At NTIS, it will be available to the general public, including foreign nations.

This technical report has been reviewed and is approved for publication.

  
MARVIN A. STIBICH  
Project Engineer

FOR THE COMMANDER

  
MARVIN F. SCHMIDT  
Tech Area Manager, Compressors



ATTENDED BY    
NTIS  
EIC  
ENGINEERED  
DESCRIPTION  
BY   
DISTRIBUTION/AVAILABILITY CODES  
EIC  
STATE BY   
A

Copies of this report should not be returned unless return is required by security considerations, contractual obligations, or notice on a specific document.

UNCLASSIFIED

SECURITY CLASSIFICATION OF THIS PAGE (When Data Entered)

REPORT DOCUMENTATION PAGE		READ INSTRUCTIONS BEFORE COMPLETING FORM
1. REPORT NUMBER AFAPL-TR-76-48-Vol. II-2	2. GOVT ACCESSION NO.	3. RECIPIENT'S CATALOG NUMBER
4. TITLE and Subtitle Investigation of Rotating Stall Phenomena Axial Flow Compressors • Volume II Vol. II - Investigation of Rotor-Stator Inter- action Noise • Lifting-Plane Theory for a Rotor		5. TYPE OF REPORT & PERIOD COVERED Final, May 73 - May 76
7. AUTHOR(s) John A. Iordis Gregory F. Homicz Gary R. Ludwig		6. PERFORMING ORG. REPORT NUMBER XE-5315-A-12
9. PERFORMING ORGANIZATION NAME AND ADDRESS Calspan Corporation P. O. Box 235 Buffalo, New York 14221		8. CONTRACT OR GRANT NUMBER(s) F33615-73-C-2046
11. CONTROLLING OFFICE NAME AND ADDRESS U.S. Air Force Aero-Propulsion Laboratory Air Force Systems Command Wright-Patterson AFB, OH 45433		10. PROGRAM ELEMENT, PROJECT, TASK AREA & WORK UNIT NUMBERS AF-3000
14. MONITORING AGENCY NAME & ADDRESS (if different from Controlling Office)		12. REPORT DATE June 1976
		13. NUMBER OF PAGES 169
		15. SECURITY CLASS. (of this report) Unclassified
		15a. DECLASSIFICATION DOWNGRADING SCHEDULE
16. DISTRIBUTION STATEMENT (of this Report) Approved for public release; distribution unlimited. DTIC Ref. 1 May 76 - 1 May '76		
17. DISTRIBUTION STATEMENT (of the abstract entered in Block 20, if different from Report) CALISTAN-XE-5315-A-12-VI-2		
18. SUPPLEMENTARY NOTES		
19. KEY WORDS (Continue on reverse side if necessary and identify by block number) Rotating Stall                      Fluid Mechanics Compressor                            Jet Engines Cascade                                Acoustics Control Systems                        Noise		
20. ABSTRACT (Continue on reverse side if necessary and identify by block number) This report presents the results of a research program that had two major objectives. The first objective was the development of a prototype rotating stall control system which was tested both on a low speed rig and a J-85-5 engine. The second objective was to perform fundamental studies of the flow mechanisms that produce rotating stall, surge and noise in axial flow compressors and thereby obtain an understanding of these phenomena that would aid attaining the first objective. The work is reported in three separate volumes. Volume I		

DD FORM 1473 EDITION OF 1 NOV 65 IS OBSOLETE

UNCLASSIFIED

SECURITY CLASSIFICATION OF THIS PAGE (When Data Entered)

UNCLASSIFIED

SECURITY CLASSIFICATION OF THIS PAGE(When Data Entered)

20. (Cont'd)

covers the fundamental theoretical and experimental studies of rotating stall; Volume II covers the theoretical and experimental studies of discrete-tone aerodynamic noise generation mechanisms in axial flow compressors; and Volume III covers the development and testing of a prototype rotating stall control system on both the low speed test rig and the J-85-5 engine.

UNCLASSIFIED

SECURITY CLASSIFICATION OF THIS PAGE(When Data Entered)

## FOREWORD

This is the final Technical Report prepared by the Calspan Corporation. The effort was sponsored by the Air Force Aero-Propulsion Laboratory, Air Force Systems Command, Wright-Patterson AFB, Ohio under Contract F33615-73-C-2046 for the period 1 May 1973 to 31 May 1976. The work herein was accomplished under Project 3066, Task 306603, Work Unit 30660334, "Investigation of Rotating Stall Phenomena in Axial Flow Compressors," with Mr. Marvin A. Stibich, AFAPL/TBC, as Project Engineer. Dr. Gary R. Ludwig of the Calspan Corporation was technically responsible for the work. Other Calspan personnel were: Joseph P. Nouni, John C. Erickson, John A. Lordi, Gregory F. Homicz, and Rudy H. Arendt.

## ABSTRACT

This report presents the results of a research program that had two major objectives. The first objective was the development of a prototype rotating stall control system which was tested both on a low speed rig and a J-85-5 engine. The second objective was to perform fundamental studies of the flow mechanisms that produce rotating stall, surge and noise in axial flow compressors and thereby obtain an understanding of these phenomena that would aid attaining the first objective. The work is reported in three separate volumes. Volume I covers the fundamental theoretical and experimental studies of rotating stall; Volume II covers the theoretical and experimental studies of discrete-tone aerodynamic noise generation mechanisms in axial flow compressors; and, Volume III covers the development and testing of a prototype rotating stall control system on both the low speed test rig and the J-85-5 engine.

Volume I describes the theoretical and experimental investigation of the influence of distortion on the inception and properties of rotating stall for an isolated rotor row, and the effects of close coupling of a rotor and stator row on rotating stall inception. The experiments were conducted in the Calspan/Air Force Annular Cascade Facility, which is a low speed compressor research rig. In addition, the previously developed two dimensional stability theory for prediction of inception conditions was extended to include the effect of compressibility and the development of a three dimensional theory was initiated. These studies led to the following key results. The experimental studies of distortion show that for a single blade row the response of the blade row to the distortion and rotating stall are uncoupled phenomena and may be explained on the basis of a linearized analysis. The experimental studies of a closely coupled rotor-stator pair show that the addition of a closely spaced stator row downstream of a rotor row delays the onset of rotating stall. Moreover, the corresponding theoretical analysis predicts this trend although quantitative agreement is hampered by the lack of appropriate steady-state loss and turning performance for each blade row at the required operating conditions. The theoretical investigation of the effects of compressibility for wholly subsonic flows outside the blade rows indicates that the effects of

compressibility do not alter the mechanisms of rotating stall as deduced from the incompressible theory in that the rate of change of the steady state loss curve with inlet swirl is the dominant blade row characteristic affecting its stability. Therefore, if the steady state losses are known for the compressible flow condition, the linearized stability analysis is expected to apply.

Volume II describes a theoretical and experimental study of discrete-tone noise generation by the interaction of a rotor and a stator, and the development of a direct lifting surface theory for an isolated rotor. An approximate model has been developed to predict the sound pressure level and total power radiated at harmonics of the blade passage frequency for a rotor-stator stage. The analysis matches the duct acoustic modes for an annular duct with an approximate representation of the unsteady blade forces which includes compressibility effects. Measurements were made of the sound pressure levels produced on the duct wall of the annular cascade facility by a rotor-stator pair. Predictions which indicated that only the fourth and higher harmonics could be excited at conditions achievable in the facility, were borne out by the experiments. The calculations of the sound pressure levels for the propagating modes were significantly below the measured values. This discrepancy is believed to result from inaccuracies in existing models of rotor wake velocity profiles, which are shown to have a strong influence on predictions of the sound pressure levels of the higher harmonics. Volume II also contains the formulation of a direct lifting surface theory for the compressible, three-dimensional flow through a rotor row in an infinitely long annular duct. A detailed derivation is given for the linearized equations and the corresponding solutions for the blade thickness and loading contributions to the rotor flow field. The governing integral equation for the blade loading in a lifting surface theory is obtained for subsonic flow and progress on its solution is reported.

Volume III describes the development and testing of a prototype rotating stall control system. The control system was tested on the low speed compressor research rig and on a J-85-5 turbojet engine. On the low speed research compressor, the control was tested in the presence of circumferential inlet distortion. These tests were performed to demonstrate the ability of

the control to operate satisfactorily in the presence of inlet distortion and to aid in the selection of stall sensor configurations for the subsequent engine tests. The control system was then installed on a J-85-5 jet engine and its performance was tested under sea level static conditions, both with and without inlet distortion. On the engine, the stall control was installed to override the normal operating schedule of the compressor bleed doors and inlet guide vanes. The J-85-5 was stalled in two ways, first by closing the bleed doors at constant engine speed, and second by decelerating the engine with the bleed doors partially closed at the beginning of the deceleration. A total of 41 compressor stalls were recorded at corrected engine speeds between 48 and 72 percent of the rated speed. In all cases, the control took successful remedial action which limited the duration of the stall to 325 milliseconds or less.



TABLE OF CONTENTS

<u>Section</u>	<u>Title</u>	<u>Page</u>
I	INTRODUCTION . . . . .	1
II	EXPERIMENTAL ACOUSTICS RESEARCH. . . . .	3
	A. DESCRIPTION OF ANNULAR CASCADE FACILITY . . . . .	4
	B. NOISE GENERATED BY ROTOR-STATOR INTERACTION . . . . .	5
	C. ISOLATED ROTOR MEASUREMENTS . . . . .	11
	D. CONCLUDING REMARKS. . . . .	13
III	APPROXIMATE MODEL OF ROTOR-STATOR INTERACTION NOISE. . . . .	15
	A. ACOUSTIC ANALYSIS . . . . .	18
	B. AERODYNAMIC MODEL . . . . .	20
	C. COMBINED AERO-ACOUSTIC ANALYSIS . . . . .	23
	1. Pressure Mode Amplitudes . . . . .	26
	2. Sound Pressure Level and Total Radiated Power. . . . .	29
	D. COMPARISONS OF THEORY WITH EXPERIMENT AND DISCUSSION. . . . .	34
	E. ADDITIONAL NUMERICAL RESULTS. . . . .	43
	F. CONCLUDING REMARKS. . . . .	46
IV	DIRECT LIFTING SURFACE THEORY FOR A COMPRESSOR ROTOR . . . . .	48
	A. DERIVATION OF MODEL EQUATIONS AND GREEN'S FUNCTION SOLUTION . . . . .	52
	B. MASS SOURCE AND PRESSURE DIPOLE SOLUTIONS . . . . .	58
	C. FLOW FIELD OF A NONLIFTING ROTOR (THICKNESS PROBLEM). . . . .	68
	1. Solution for the Velocity Potential. . . . .	68
	2. Expressions for the Velocity Components and Pressure Perturbation. . . . .	73
	3. Behavior of the Velocity Components at the Blade Surfaces . . . . .	74

TABLE OF CONTENTS (Cont'd.)

<u>Section</u>	<u>Title</u>	<u>Page</u>
IV	DIRECT LIFTING SURFACE THEORY FOR A COMPRESSOR ROTOR	
	D. FLOW FIELD OF A LIFTING ROTOR (LOADING PROBLEM) . . . . .	82
	1. Solution for the Perturbation Pressure . . . . .	82
	2. Expressions for the Velocity Components. . . . .	85
	3. Behavior of the Velocity Components at the Blade Surfaces and Across the Trailing Vortex Wakes. . . . .	88
	E. DIRECT LIFTING SURFACE THEORY . . . . .	102
	1. Formulation of the Integral Equation . . . . .	102
	2. Progress Toward the Solution . . . . .	108
	F. CONCLUDING REMARKS. . . . .	112
V	SUMMARY AND CONCLUSIONS. . . . .	114
APPENDIX A	DEFINITION OF RADIAL EIGENFUNCTIONS . . . . .	116
APPENDIX B	EXPRESSIONS FOR ROTOR-STATOR INTERACTION FORCES . . . . .	118
APPENDIX C	MASS AND MOMENTUM BALANCES FOR SINGULARITY AND ROTOR FLOW FIELDS . . . . .	124
REFERENCES	. . . . .	165

## ILLUSTRATIONS

FIGURE	TITLE	PAGE
1	Test Configuration for Acoustic Studies of Rotor-Stator Interaction . . . . .	139
2	Sketch of Acoustic Probe Calibration Apparatus. . . . .	140
3	Acoustic Probe Calibration Results, Pure Tone Excitation. . .	141
4	Calibration of Microphone in Acoustic Probe . . . . .	142
5	Oscilloscope Records of Noise Signal From Rotor-Stator Interaction . . . . .	143
6	Uncorrected 1/3 Octave Spectrum of Outer Wall Sound Pressure Level From Rotor-Stator Interaction	
	a. Rotor RPM = 1130 . . . . .	144
	b. Rotor RPM = 1155 . . . . .	145
	c. Rotor RPM = 1163 . . . . .	146
	d. Rotor RPM = 1170 . . . . .	147
7	Experimental Outer Wall Sound Pressure Levels From Rotor-Stator Interaction, Stator Stagger Angle = 37.2 Deg . .	148
8	Experimental Outer Wall Sound Pressure Levels From Rotor-Stator Interaction, Stator Stagger Angle = 28.2 Deg . .	149
9	Blade Tip Passage Pressure Signals on Isolated Rotor at Various Rotor Speeds, Chordwise Location = 18%, Axial Velocity, $U_o = 60$ ft/sec	
	a. Rotor RPM = 600, Inlet Swirl Angle, $\beta_{1,TIP} = 52.0$ Deg . .	150
	b. Rotor RPM = 700, Inlet Swirl Angle, $\beta_{1,TIP} = 56.2$ Deg . .	150
	c. Rotor RPM = 800, Inlet Swirl Angle, $\beta_{1,TIP} = 59.7$ Deg . .	151
	d. Rotor RPM = 900, Inlet Swirl Angle, $\beta_{1,TIP} = 62.5$ Deg . .	151

ILLUSTRATIONS (Cont'd.)

FIGURE	TITLE	PAGE
10	Blade Tip Passage Pressure Signals at Various Chordwise Locations on Isolated Rotor During Rotating Stall . . . . .	152
11	Acoustic Model. . . . .	153
12	Aerodynamic Model . . . . .	154
13	Classification of Pressure Waves. . . . .	155
14	Asymmetry in Angular Deviation Between Dipole Axis and Propagation Vectors . . . . .	156
15	RMS Wall Pressure at Fourth Harmonic of Blade Passage Frequency Vs Rotor RPM; Mean Stator Stagger Angle = 37.2 Deg.	157
16	RMS Wall Pressure at Fourth Harmonic of Blade Passage Frequency Vs Rotor RPM; Mean Stator Stagger Angle = 28.2 Deg.	158
17	RMS Wall Pressure at Fifth Harmonic of Blade Passage Frequency; Mean Stator Stagger Angle = 28.2 Deg . . . . .	159
18	Theoretical SPL and Total Radiated Power at Blade Passage Frequency Versus Rotor RPM; Mean Stator Stagger Angle = 37.2 Deg. . . . .	160
19	Blade Geometry and Blade-Fixed Coordinate System. . . . .	161
20	Coordinate System Aligned with Undisturbed Flow Direction . .	162
21	Blade Surface Geometry. . . . .	163
22	Generalized Function, $\zeta_i$ , Defined By Eq. (126) . . . . .	164

TABLES

TABLE	TITLE	PAGE
1	Comparative Influence of Various Wake Profiles on Acoustic Predictions . . . . .	42
2	Comparison of Modal Amplitudes Computed by Clark et al. <sup>19</sup> with Present Theory . . . . .	44
3	Coefficients in the Expression for the Normal Velocity Component of a Lifting Rotor, Equation (172). . . . .	101

## SYMBOLS

Separate lists of symbols are given for Sections III and IV.

### SYMBOLS FOR SECTION III, APPROXIMATE MODEL OF ROTOR-STATOR INTERACTION NOISE

- $a_0$  undisturbed sound speed
- $A_n$  Glauert coefficients, Appendix B
- $A_{nm}^{u,d}$  admittance of  $n,m$  mode, Equation (27)
- $B$  number of rotor blades
- $b$  axial separation of blade row centerlines
- $c_R, c_S$  semi-chord lengths
- $C_D$  drag coefficient per unit span, Equation (37)
- $C_L$  lift coefficient per unit span, Equation (43)
- $\Delta C_{p_T}$  total pressure loss coefficient
- $d_R, d_S$  blade spacing
- $\vec{F}_R, \vec{F}_S$  force per unit volume exerted by blades on the air
- $h$  hub/tip ratio,  $r_H / r_T$
- $k$  acoustic wave number,  $N_f B \Omega / a_0$
- $k_{nm}$  Equation (18)

SYMBOLS, SECTION III (Cont'd.)

- $L_R, L_S$  total unsteady lift per unit span
- $l$  unsteady load harmonic index
- $m$  radial mode index
- $M_x$  axial flow Mach number
- $N_f$  harmonic of blade passage frequency
- $n$  azimuthal mode index
- $p$  pressure perturbation
- $p_{nm}$  Fourier decomposition of pressure field, Equation (6)
- $p_{nm}^{u,d}$  pressure modal amplitude, Equation (18)
- $P^{u,d}$  total sound power radiated along the duct, Equation (28)
- $P_{nm}^{u,d}$  sound power in  $(n,m)$  mode
- $q$  dynamic pressure
- $R_{nm}(r, \sigma)$  radial eigenfunctions, Appendix A
- $r$  cylindrical radius
- $r_H, r_T$  hub, tip radii

SYMBOLS, SECTION III (Cont'd.)

- $S$  acoustic source distribution, Equation (4)
- $S_{nm}$  Fourier decomposition of source distribution, Equation (7)
- $SPL$  sound pressure level, Equation (23)
- $t$  time
- $U_x$  uniform axial velocity
- $U$  tangential velocity,  $\Omega r$
- $u$  axial velocity perturbation, or viscous wake velocity defect
- $u_{nm}^{u.d}$  axial velocity mode amplitude, Equation (27)
- $V_m$  mean velocity relative to blade row
- $v_{nm}$  radial eigenvalue for  $(n,m)$  mode, Appendix A
- $x$  axial coordinate
- $x_R, x_S$  axial location of rows in line dipole model
- $X_l, Y_l, Z_l$  magnitudes of  $l$ th harmonic of unsteady lift per unit span resulting from the three interaction mechanisms, Equation (11)
- $y$  viscous wake half-width
- $\alpha_R, \alpha_S$  blade row stagger angles



SYMBOLS, SECTION III (Cont'd.)

$$\beta \quad (1-M_x^2)^{1/2}$$

$\delta(x)$  Dirac delta function

$\xi$  Fourier transform variable in axial coordinate

$\theta$  azimuthal coordinate

$$\mu_{nm} \quad v_{nm} / r_T$$

$\nu_R, \nu_S$  fundamental blade loading frequency, Equation (12)

$\rho_0$  undisturbed density

$\sigma$  dimensionless radius,  $r/r_T$

$\phi_{nm}^{u,d}$  propagation angle of  $(n,m)$  mode, relative to dipole axis, Figure 14

$\Omega$  rotor angular velocity, radians/sec.

$\omega$  acoustic frequency,  $N_f B \Omega$

$\langle \rangle$  denotes time average over one blade-passing period

$||$  magnitude of a vector or complex number

$*$  complex conjugate

SYMBOLS, SECTION III (Cont'd.)

Subscripts

- $1,2$  refer to upstream or downstream blade row, respectively
- $c$  evaluated on viscous wake centerline
- $l$  refers to  $l$  th loading harmonic
- $m$  refers to  $m$  th radial mode
- $n$  refers to  $n$  th azimuthal mode
- $R,S$  refers to rotor or stator blade rows, respectively

Superscripts

- $u,d$  refer to upstream or downstream propagating waves, respectively

SYMBOLS FOR SECTION IV, DIRECT LIFTING SURFACE THEORY FOR A COMPRESSOR ROTOR

- $a_\infty$  undisturbed sound speed
- $\vec{A}$  vector defined in Equation (63)
- $A_i$  coefficient in polynomial expansion for axial variation of blade loading
- $A_{mBk}^{(1)}$  real part of coefficient defined in Equation (173), see Table 3

SYMBOLS, SECTION IV (Cont'd.)

- $B$  number of blades
- $B_{mbk}^{(l)}$  imaginary part of coefficient defined in Equation (173), see Table 3
- $c$  blade chord
- $c_a$  axial projection of blade chord
- $C_{mbk}^{(l)}$  coefficient defined in Equation (173), see Table 3
- $d_1, d_2$  integrals defined in Equation (C-50), Appendix C.
- $D$  dipole strength
- $D_{mbk}$  quantity defined in Equation (167)
- $\bar{e}_r, \bar{e}_\theta, \bar{e}_z$  unit vectors in cylindrical coordinate system
- $f$  function of radius appearing in blade thickness distribution, Equation (110)
- $\bar{F}$  force per unit volume
- $\bar{f}$  net force on control volume
- $g$  axial dependence of blade thickness distribution, Equation (110)
- $G$  Green's function
- $G_{mbk}^{(l)}$  quantity defined in Equation (178)

SYMBOLS, SECTION IV (Cont'd.)

- $k$  ratio of hub radius to tip radius
- $H(\ )$  Heaviside step function
- $I_1, I_2$  surface integrals in Equation (66)
- $I(z)$  integral of pressure perturbation along streamlines
- $Q_i$  integrals defined in Appendix C
- $k$  radial mode number
- $K_{nk}$  radial eigenvalues
- $L$  operator defined by Equation (58)
- $L_{msk}$  quantity defined in Equation (173)
- $m$  multiple of blade number for azimuthal mode,  $n = mB$
- $\dot{m}$  mass flux to first order in perturbation quantities
- $M$  Mach number of undisturbed axial stream,  $U/a_\infty$
- $M_R$  Mach number based on undisturbed relative velocity in blade fixed coordinates,  $U_R/a_\infty$
- $M_T$  Mach number based on rotor speed at blade tip radius,  $\omega r_T/a_\infty$
- $n$  azimuthal mode number or coordinate mutually normal to undisturbed streamline and radial directions

SYMBOLS, SECTION IV (Cont'd.)

- $\bar{n}$  unit vector normal to undisturbed streamline and radial directions
- $\eta_c$  blade camber line
- $\eta_{u,l}$  distance to upper and lower blade surfaces
- $p$  pressure perturbation
- $p_0$  undisturbed pressure
- $p_i$  terms in expression for pressure perturbation, Equation (148)
- $\Delta p$  local blade loading
- $\overline{\Delta p}$  blade loading averaged over radius
- $P_i$  terms in polynomial representation of blade loading, Equation (190)
- $Q$  source strength
- $q_1, q_2$  integrals defined by Equation (C-39), Appendix C
- $r$  radial coordinate
- $R_{nk}$  normalized radial eigenfunctions
- $S$  distance along undisturbed streamlines
- $\bar{S}$  unit vector along undisturbed streamlines

SYMBOLS, SECTION IV (Cont'd.)

$\text{sgn}(\ )$  +1 for  $\text{arg} > 0$ , -1 for  $\text{arg} < 0$

$S$  surface area

$S(r, z)$  function defined in Equation (121)

$t$  blade thickness

$T_{m8k}$  quantity defined in Equation (131)

$J_z$  axial component of torque exerted on control volume

$U$  undisturbed axial velocity

$U_R$  undisturbed relative velocity in blade-fixed coordinates

$\vec{v}$  perturbation velocity,  $(v_r, v_\theta, v_z)$  or  $(v_r, v_n, v_s)$

$(v_n)_i$  terms in normal component of perturbation velocity, Equations (160) and (168)

$V$  volume

$V_{m8k}$  quantity defined in Equation (117)

$\vec{W}$  total velocity in blade fixed coordinates

$z$  normalized axial coordinate, Equation (179)

$Z$  axial coordinate

SYMBOLS, SECTION IV (Cont'd.)

- $\beta$   $\sqrt{1 - M^2}$
- $\gamma$  local vortex strength
- $\Gamma$  blade circulation
- $\delta(\ )$  Dirac delta function
- $\delta_{nm}$  Kronecker delta
- $\epsilon$  vanishly small quantity
- $\xi$  helical coordinate,  $\xi = \theta - \omega z / U$
- $\xi_j$  generalized function defined in Equation (126)
- $\eta_T$   $c_a / 2r_T$
- $\theta$  azimuthal coordinate
- $\lambda_{nk}$  quantity defined in Equation (71)
- $\Lambda_{mbk}$  quantity defined in Equation (114)
- $\mu$  index of Lommel function
- $\vec{n}$  normal to surface
- $\xi$  Fourier transform variable, or dummy variable for argument of Bessel functions

SYMBOLS, SECTION IV (Cont'd.)

$\xi_{n*}$	poles of integrand in Equation (78)
$\rho$	density perturbation
$\rho_m$	undisturbed density
$\sigma$	normalized radial coordinate, $r/r_T$
$\phi$	velocity potential
$q_{n*}$	coefficient in expansion of $\phi$ in terms of duct eigenfunctions, Equation (72)
$\Phi$	scalar function defined in Equation (62)
$\Phi_T$	$\omega r_T / U$
$\psi$	$\tan^{-1}(\omega r / U)$
$\omega$	angular velocity of rotor
$(\bar{\quad})$	Fourier transform
$(\hat{\quad})$	dimensionless variable, see Equation (186)

Subscripts

D	property of dipole solution
H	evaluated at hub radius



SYMBOLS, SECTION IV (Cont'd.)

$j$	$j$ th blade
$k$	$k$ th radial mode
$n$	$n$ th azimuthal mode
$O$	source coordinates
$S$	property of source solution
$T$	evaluated at tip radius

SECTION I  
INTRODUCTION

The useful operating range of a turbine engine compressor is greatly influenced by its stalling characteristics. The optimum performance of a turbo-propulsion system is usually achieved when the compressor is operating near its maximum pressure ratio. However, this optimum is generally not attainable because it occurs close to compressor stall and unstable flow conditions. Because of the serious mechanical damage that may result during compressor stall cycles, a factor of safety (stall margin) must be provided between the compressor operating line and the stall boundary. This is usually done by prescheduling the primary engine controls. However, the prescheduling approach can lead to the requirement for a large stall margin in order to keep the engine from stalling under all possible transient and steady state flight conditions. It is clear, then, that an engine control system that can sense incipient destructive unsteady flow in a compressor and take corrective action would allow for reduced stall margins in the design and thus lead to large engine performance and/or efficiency gains. Recognition of this fact has been the motivation for a continuing program of research that the AFAPL has sponsored at Calspan dating back to 1962.

The work at Calspan has been both theoretical and experimental in nature and has been aimed at obtaining a sufficient understanding of the rotating stall phenomena such that its onset and its properties can be predicted and controlled. The capability of predicting the onset of rotating stall on isolated blade rows of high hub to tip ratios in low speed flows was demonstrated in Reference 1. In addition, the basic feasibility of developing a rotating stall control system was demonstrated in the Calspan/Air Force Annular Cascade Facility. This present report summarizes the latest three year research program at Calspan. The specific goals of the present program were to extend the fundamental studies of rotating stall to consider the effects of compressibility, blade row interaction and inlet distortion; and to extend the

fundamental aerodynamic and acoustic analysis of flow through a compressor. In addition, the rotating stall control system was validated by successful ground tests on a J-85-5 turbojet engine.

The work is reported in three separate volumes. Volume I entitled, "Basic Studies of Rotating Stall", covers the theoretical and experimental work on the effects of distortion and close coupling of blade rows on rotating stall inception and properties. In addition, the theoretical analysis of compressibility is treated in the two-dimensional approximation and the initial development of a three-dimensional theory is given. Volume II entitled, "Investigation of Rotor-Stator Interaction Noise and Lifting Surface Theory for a Rotor", describes the development of a linearized lifting surface theory for the subsonic compressible flow through an isolated rotor row. In addition, a theoretical and experimental study of the noise generated by the interaction of a rotor and stator is described. Volume III entitled, "Development of a Rotating Stall Control System", describes the development and testing of the control system installed on a low speed research compressor and on a J-85-5 turbojet engine.

In the current three-year segment of the ongoing research program on rotating stall, the scope of the investigation was expanded to include studies of the aerodynamics and acoustics of axial flow compressors. Volume II contains the results of this aspect of the program, which consisted of two basic parts: the theoretical and experimental investigation of discrete-tone noise generation by the interaction of a rotor and stator, and the development of the three-dimensional direct lifting surface theory for a compressor rotor. An approximate model has been developed to predict the sound pressure level and total power radiated at harmonics of the blade passage frequency for a rotor-stator stage. Also, measurements were made of the sound pressure levels produced on the outer duct wall of the annular cascade facility by a rotor-stator pair. In the development of a direct lifting surface theory, the governing integral equation relating the rotor blade loading to prescribed incidence and camber lines has been formulated and progress made toward its numerical solution. The experimental and theoretical studies of rotor-stator interaction noise are reported in Sections II and III, respectively. The direct lifting surface analysis is presented in Section IV.

## SECTION II EXPERIMENTAL ACOUSTICS RESEARCH

As a part of the work under a previous program, Contract AF 33(615)-3357, an annular cascade facility was designed and fabricated. Its principal purpose is to provide fundamental experimental data during and prior to the occurrence of rotating stall in order to improve our understanding of the phenomena and for use as a guide in improving the theoretical analysis. In addition to the study of rotating stall, the facility has also been used to provide acoustic data for comparison with theory and to evaluate the operation of a prototype rotating stall control system. The fundamental experiments on rotating stall are described in Volume I of this report and the control system tests are described in Volume III. This section of Volume II presents the results of the acoustic experiments.

Two sets of experiments were performed in support of the theoretical developments described in Section III and IV of this volume. The first set of experiments were designed to provide data for correlation with the approximate theory of Section III for the prediction of rotor-stator interaction noise. In these experiments, the far-field sound pressure levels generated by rotor-stator interaction were measured in the constant area annulus upstream of a rotor-stator stage. These measurements were performed over a range of rotor speeds for two different stagger angle settings of the stator blades. The second set of experiments were intended to provide a measure of the tip pressure loading on an isolated rotor for comparison with the direct lifting surface theory of Section IV. In these experiments, time-varying records of the outer wall static pressure fluctuations caused by blade tip passage were obtained for a number of different chordwise locations on the rotor blades. The scope of these tip loading experiments was very limited.

The order of presentation of the experimental studies in the remainder of this section is as follows. A brief description of the annular cascade facility is presented in Section II-A. Section II-B presents the results of

the measurements of noise caused by rotor-stator interaction. This is followed by the presentation, in Section II-C, of a typical set of results obtained for the blade passage fluctuations on an isolated rotor. Finally, some concluding remarks on the experimental studies are presented in Section II-D.

#### A. DESCRIPTION OF ANNULAR CASCADE FACILITY

A detailed description of the annular cascade facility has been presented in Reference 1, and further details are given in Volume I of this report. Only a brief description of the facility is given here.

The annular cascade facility consists of a test section built around the outer front casing of a J-79 jet-engine compressor with a Calspan fabricated hub. The facility includes a bell-mouth inlet on the outer casing and a bullet nose on the hub to provide a smooth flow of air to the test section. Outlet ducting is connected to an independently variable source of suction to provide the required flow through the annulus. An electrically powered two-speed axial flow fan is used as the source of suction. Continuous control of the mass flow is achieved through the use of variable inlet guide vanes to the fan and a variable damper in the fan exit flow.

The test section of the annular cascade forms a circular annulus with an outer diameter of 29.35 inches and an inner diameter of 23.35 inches which provides a hub-to-tip ratio of 0.80. The outer casing will accept up to six variable stagger angle stator rows. The hub has provision for two rotor rows at the third- and fifth-stage rotor locations of the J-79 compressor. At the time the acoustic studies were performed, either rotor row could be rotated while the other was held fixed or both rows could be rotated together. The rotor assembly was powered by a 24 horsepower hydraulic motor. Rotational speed was continuously variable in either direction between zero and approximately 1500 rpm. An external hydraulic pump system powered by a 30 horsepower electric motor was used to provide power for the hydraulic motor.

Although the speed range of the rotor was restricted at the time of these tests, it was possible to perform acoustic tests for comparison with the theory of Section III. The flexibility of control and the relative absence of background noise in the facility are features which were highly useful in the performance of the tests.

#### B. NOISE GENERATED BY ROTOR-STATOR INTERACTION

The configuration of the annular cascade used for the rotor-stator interaction studies is shown in Figure 1 along with some details of the microphone-probe assembly used in the acoustic work. The rotor-stator stage studied is designated Rotor Set No. 1 (46 blades) and Stator Set No. 1 (54 vanes) in Reference 1. These are modified blade rows from the fifth stage of a J-79 compressor. Their characteristics and performance when used as isolated blade rows in the annular cascade have been presented in Reference 1. The mean stagger angles (at mid-annulus) were  $\alpha_R = 40^\circ$ ,  $\alpha_S = 37.2^\circ$  or  $28.2^\circ$ , and the semi-chords  $c_R = .0604$  ft. and  $c_S = .054$  ft. The axial separation of the mid-chord planes was  $b = .125$  ft.

The sound pressure levels produced by rotor-stator interaction were measured on the outer casing upstream of the rotor. In taking these data, the fan system downstream of the annular cascade was turned off and the fan was allowed to rotate freely under the influence of the flow generated by the rotor in the annular cascade. In addition, all dampers in the downstream drive system were opened wide. It was convenient to use this wide open configuration because it was found to provide nearly constant inlet swirl angles relative to the rotor. That is, the mean axial velocity in the annular cascade increased in direct proportion to the rotor angular velocity. This feature made application of the rotor-stator interaction theory much simpler because the dimensionless steady state loss and turning performance data for the rotor also remained approximately constant with changing rotor speeds.

A Bruel and Kjaer (B & K) acoustic-probe with its tip flush with the inner surface of the compressor casing was used in combination with a B & K condenser microphone and sound level meter to measure the interaction noise. The sound level meter output was recorded on an instrumentation quality FM tape recorder. The recorded data were processed later on a modified General Radio Type 1921 real time analyzer to obtain one-third octave spectra of the signals.

The tape recording of the noise was necessary because the rotor-stator interaction harmonic frequencies were above the frequency range available on the real time analyzer. The maximum frequency accommodated by the spectrum analyzer is the third octave centered on 2500 Hz while the noise harmonics extended up to approximately 5000 Hz. The effective frequency range of the noise spectrum was reduced by a factor of four by recording at 30 ips and playing back for spectrum analysis at 7-1/2 ips. Absolute calibration of the complete system including the tape recorder was obtained by recording a 114 db signal from a General Radio microphone calibrator at the beginning and end of each tape. These calibration signals were used to set the gain of the overall system when played back through the spectrum analyzer.

Within the frequency range of interest, the response of the microphone-sound level meter system was essentially flat. However, the acoustic probe assembly introduced frequency dependent distortion to this flat response. Thus, it was necessary to obtain a calibration for the complete system including the acoustic probe. A sketch of the acoustic probe calibration apparatus is shown in Figure 2. All of the apparatus shown in the sketch is manufactured by B & K. The calibrator consists of a small cavity into which sound is introduced by an earphone speaker. For a given excitation of the speaker, the sound pressure level in the cavity is measured by the microphone in its reference level location (position #1). The acoustic probe is in place during these measurements with a dummy microphone inserted in its end. Following the reference level measurements, the microphone is inserted in the acoustic probe (position #2) and the dummy microphone inserted in the reference

level location (position #1). The sound pressure levels detected by the microphone in the probe are then determined for the same speaker excitation as used in the reference level measurements. The difference between the two sets of measurements provides a frequency dependent calibration for the probe.

In the current work, the probe was calibrated first without any steel wool damping material in the tube. This calibration showed a rather large (12 db) probe resonant peak at approximately 1900 Hz. The probe was then calibrated with three different degrees of steel wool damping and a final damping configuration was selected for use in the noise measurements. The sound pressure levels measured with pure tone excitation of the earphone speaker are shown in Figure 3 for the frequency range of interest and for both microphone positions in the calibrator. Both curves drop off at high frequency because of frequency response limitations on the earphone speaker. The difference between the two curves provides the calibration of the acoustic probe.

The probe calibration is shown in Figure 4. The circular points were obtained with pure tone excitation of the speaker at the indicated frequencies. These values must be subtracted from the measured noise levels. A second calibration result is also shown on this figure as solid straight line segments. This was obtained by exciting the speaker with pink noise and analyzing the result on the 1/3 octave real time analyzer. The effective 1/3 octave bandwidths of the results are represented by the length of the horizontal portions of the segmented curve. If allowance is made for the larger bandwidth of the 1/3 octave analyzer, the agreement between the two calibration curves is very good. Since the rotor-stator interference noise was very close to a pure tone, the pure tone calibration curve was used in correcting the measured results.

The pure tone nature of the interference noise is illustrated in Figure 5. This figure shows photographic oscilloscope records of the unfiltered output from the sound level meter. In the upper photograph, the top trace is generated by the noise signal and the lower trace is the output from an audio oscillator tuned to the same frequency as the predominant noise harmonic.



The jitter in the upper trace signals is caused by the presence of frequencies other than the predominant harmonic. Tuning of the audio oscillator was accomplished by setting the oscilloscope trigger mechanism to fire on the audio oscillator signal and then adjusting the oscillator frequency until a stationary noise signal was attained. This procedure led to a number of possible oscillator frequencies for the noise harmonic. The correct frequency was difficult to determine because of the jitter in the noise signal. The oscillator frequency was then determined by forming a Lissajous figure from the noise and oscillator signals. The lower photograph in Figure 5 shows the Lissajous figure corresponding to the upper photograph. The multiple ellipses in the lower photograph show that the noise and oscillator signals are correctly matched in fundamental frequency. The multiplicity of ellipses arises from the same reason as the jitter in the upper photograph.

The procedure described in the previous paragraph was used to determine the frequency of the predominant pure tone noise for all tests where a strong blade row interaction signal was obtained. Thus, it was possible to identify accurately which harmonic of rotor blade passage frequency was being excited by the interaction mechanism.

Samples of the one-third octave spectra of the interaction noise are shown in Figures 6a through 6d. These figures are direct reproductions of the output from the spectrum analyzer. Absolute sound pressure level for any one-third octave band is obtained by correcting the relative db levels for system gain and for acoustic probe response. The frequency dependent probe response correction has been discussed previously. The system gain correction is independent of frequency and is noted on the lower right hand side of each figure. For the particular examples of Figure 6, system gain is corrected for by adding 80 db to all relative levels.

Figures 6a through 6d have been chosen to illustrate the extremely sharp rise in interaction noise as rotor speed is increased over a very small range of rpm from below cutoff to above cutoff of the fourth rotor blade passage harmonic. Figures 6a and 6b correspond to conditions slightly below

cutoff. Here the noise spectra are generated primarily by turbulent pressure fluctuations within the boundary layer on the outer wall and by the free-wheeling fan downstream of the annular cascade test section. Figures 6c and 6d show the sharp rise in fourth harmonic interaction noise as the rotor rpm increased to above cutoff conditions. This rise can be seen in the third octave bands centered at  $\text{Hz} \times 1/4 = 800$  and  $1000$ . Both of these third octave bands respond because the pure tone frequency is nearly mid-way between these two bands. The measured pure tone frequency is shown on the lower right hand side of Figures 6c and 6d. It can be seen that the pure tone frequency is approximately  $3600 \text{ Hz}$  for both figures corresponding to  $\text{Hz} \times 1/4 = 900$ .

The correct sound pressure level for the pure tone signal was obtained from spectra such as shown in Figure 6 by combining the two third octave band responses closest to the pure tone frequency and then correcting the indicated SPL for acoustic probe response at the measured pure tone frequency. An example of the procedure for the data of Figure 6d is as follows.

Relative Level for third octave centered at  $\text{Hz} \times 1/4 = 800$  is  $34.75 \text{ db}$

Relative Level for third octave centered at  $\text{Hz} \times 1/4 = 1000$  is  $39.25 \text{ db}$

Combined Relative Level =  $20 \log \left[ \log^{-1} \frac{34.75}{20} + \log^{-1} \frac{39.25}{20} \right] = 43.3 \text{ db}$

Combined Level Corrected for system gain =  $43.3 + 80 = 123.3 \text{ db}$

Probe response at pure tone frequency ( $3610 \text{ Hz}$ ) =  $-4.7 \text{ db}$  (from Figure 4)

Corrected pure tone Sound Pressure Level =  $123.3 - (-4.7) = 128.0 \text{ db}$ .

The pure tone frequency in all cases where it was measurable corresponded very closely to either the calculated fourth or fifth harmonic of rotor blade passage frequency. For the example given above, the calculated fourth harmonic of rotor blade passage frequency is  $3588 \text{ Hz}$  and the measured pure tone frequency is  $3610 \text{ Hz}$ . The difference between the two is within the accuracy of the audio oscillator used in the measurements. For conditions below cutoff such as shown in Figures 6a and 6b, the sound pressure levels for the fourth blade passage harmonic were estimated from the data using the calculated fourth harmonic frequency and the measured levels in the two third octave bands closest to this calculated frequency.

The results of the interaction noise measurements are summarized in Figures 7 and 8 for rotor speeds ranging from below cutoff to the maximum speed available. Figure 7 shows the results obtained for a stator stagger angle of 37.2 degrees and Figure 8 shows the results obtained for 28.2 degrees. In both figures, an estimate of the background level in the third octave band closest to the measured pure tone frequency is also shown. This was obtained by inspection of the third octave bands on each side of the bands used to calculate the pure tone levels and must be considered highly approximate in nature. Any data point for harmonic level of the SPL within about 10 db of the approximate background level probably contains a certain degree of background noise from the mechanical systems or the turbulent wall pressure fluctuations. The closer the data point is to the approximate background level, the larger the contribution will be.

Most of the data shown in Figures 7 and 8 correspond to the fourth harmonic of rotor blade passage frequency. The fifth harmonic was generally masked by the background noise levels and could not be detected. However, for a stator stagger angle of 28.2 degrees, the fifth harmonic was detectable at moderately low rotor speeds, where the background noise level was low but the rotor speed was high enough to allow propagation of this mode in the annular duct system. The results are shown on the left side of Figure 8.

It was not possible to obtain interaction noise signals at harmonics of blade passage frequencies below the fourth harmonic. The generation of lower harmonics would require either a greater rotor speed capability or else blade configurations that are not available to the annular cascade in its present configuration. It is unfortunate that the generation of lower harmonics was not possible because the prediction of harmonics as high as the fourth presents a test for the interaction theory which may be more severe than is warranted in the present state of the theoretical development. Nevertheless, these data have been used for comparison with the theoretical predictions in Section III, and are discussed more fully there.

### C. ISOLATED ROTOR MEASUREMENTS

In addition to the rotor-stator interaction noise experiments described above, measurements were made of the fluctuating wall pressures produced by an isolated rotor. These measurements, which were intended to provide information on the blade tip loading, were taken at six chordwise locations along the outer casing wall.

The configuration of the annular cascade was similar to that shown in Figure 1 but with the stator row removed. Rotor Set No. 1 was used with the blade stagger angle set at 40 degrees at mid-annulus (48 degrees at the tip). As noted earlier, this rotor set had been studied previously to determine its steady state turning and loss performance (Reference 1).

Pressure fluctuations produced by the passage of the blades were obtained at rotor speeds of 600, 700, 800, 900 and 1000 rpm, while the mean axial velocity through the test section was held at 60 ft/sec. At the lowest rotor speed, the rotor blades were very lightly loaded, while at the highest speed the loading was large enough to induce rotating stall.

The pressure signals were measured by a Setra Systems Model 242 TC pressure transducer closely coupled to a hole in the outer casing of the annular cascade. The time-varying pressure signals were recorded photographically from a dual trace oscilloscope. A second signal was used to indicate rotor blade position. This signal was generated by a magnetic pickup which sensed blade tip passage past a point on the outer casing of the annular cascade. Instantaneous blade positions with respect to the pressure signals were calculated from the magnetic pickup signals and the geometric relationship between the magnetic pickup and the pressure tap.

The six axial stations used for the wall pressure measurements were situated at 13, 18, 32, 49, 64 and 79 percent of the rotor chord. A set of results is shown in Figure 9 for the station at 18 percent of the chord.

These results are typical of the measurements at all six chordwise measuring stations. Parts (a) through (d) of Figure 9 show the records obtained at rotor speeds between 600 and 900 rpm. The relative inlet swirl angle at the rotor tip is indicated for each rotor speed. The instantaneous locations of the blade pressure and suction surfaces with respect to the pressure signals are shown also.

As expected, the maximum amplitude of the pressure fluctuations increases with increasing rotor speed. (Note that the scale for pressure signals varies for different rotor speeds. The scale in each case is indicated to the left of the pressure signals.) However, the shapes of the fluctuating pressure signals are unexpected. The data records show that the maximum wall pressure is reached well ahead of the blade pressure surface at all rotor speeds. Moreover, a double pressure peak occurs at the lower rotor speeds, one ahead of the rotor pressure surface and one approximately at the location of the pressure surface. The peak in pressure at the rotor pressure surface begins to disappear as rotor speed is increased. The reason for the unexpected shape of the pressure signals is not definitely known. However, it is speculated that the results may be caused by three-dimensional effects associated with the relatively large clearances between the rotor blades and the outer casing. As explained in Volume I, a blade tip clearance of approximately 0.05 inches was required to compensate for the slightly oval shape of the production J-79 casing which forms the outer wall of the annular cascade.

The fluctuating wall pressures recorded during rotating stall are shown in Figure 10 for all six chordwise locations. Although the rotating stall phenomenon is beyond the scope of the direct lifting surface theory, these data are presented as being of general interest to the overall program; pressure signals such as the ones shown in Figure 10 are used as stall detectors in the rotating stall control system which is described in Volume III of this report.

The rotor speed for the records in Figure 10 was 1000 rpm and the mean axial velocity was 60 ft/sec. The oscilloscope sweep speed in Figure 10 is much slower than in Figure 9 so that the blade passage pressure peaks are highly compressed. The interest here is centered on the pressure fluctuations during passage of a rotating stall cell. Each photograph in Figure 10 shows the passage of two stall cells. The phase relationships between the separate photographs have no meaning since the records were not obtained simultaneously.

Figure 10 illustrates that the character of the stall cell passage signals change considerably with chordwise location on the rotor. Near the leading edge, the stall passage signals coincide with an amplitude reduction in the blade passage signals. In this region the combined maximum amplitude of the pressure signals during stall passage is almost the same as the blade passage pressure amplitude between stall cells. In contrast, near the trailing edge the passage of a stall cell coincides with an increase in amplitude of the blade passage signals and the combined maximum amplitude is larger than the blade passage amplitude between stall cells.

The rotating stall control system detects unusually large peak amplitudes in pressure signals such as shown in Figure 10. Control action is taken when these peak amplitudes reach a predetermined reference value. It is required that only those fluctuating pressure levels associated with rotating stall should initiate control action. Tests of the control have shown that the best performance is obtained when pressure signals, due to blade passage, are removed by low-pass filters. It is clear from Figure 10 that elimination of the blade passage signals will greatly improve the signal to noise ratio for stall detection purposes. This is true even for the pressure tap locations near the blade trailing edge since the blade passage pressure fluctuations still have an appreciable amplitude between the stall cells.

#### D. CONCLUDING REMARKS

The results of two separate experimental investigations have been presented in Section II. In the first investigation, Section II-9, the

far-field noise generated by rotor-stator interaction was measured to provide data for correlation with the approximate theory presented in Section III. In the second study, Section II-C, the fluctuating outer-wall static pressures generated by passage of the blade tips of an isolated rotor were measured to provide data for comparison with the direct lifting surface theory of Section IV.

The rotor-stator interference noise studies presented in Section II-B consisted of measuring the sound pressure levels in the constant area annulus far upstream of a rotor-stator stage. The measurements were made at a series of rotor speeds for two stagger angle settings of the stators. The results contained detectable pure tone components only at the fourth and fifth harmonics of blade passage frequency. The generation of lower harmonics was not possible because the rotor speed capability was limited at the time of the tests. Since the performance of these tests, the rotor speed capability of the test rig has been increased. It is planned to use this capability to perform additional measurements for conditions in which lower harmonics of blade passage frequency are propagating. The results of the current tests are compared with theoretical predictions in Section III.

The isolated rotor studies of Section II-C were intended to provide a measure of the blade tip pressure loading for comparison with the predictions of the direct lifting surface theory of Section IV. However, the theoretical development had not reached the stage where quantitative predictions could be made. Thus, samples of some of the data are presented as of interest in themselves. Inspection of the results suggest the measured pressures may have been influenced by rotor tip clearance effects. As such, the results may not be predictable by the direct lifting surface theory. Nevertheless, a comparison between theory and experiment would still be of interest.

SECTION III  
APPROXIMATE MODEL OF ROTOR-STATOR INTERACTION NOISE

The interactions between rotor and stator blade rows have long been recognized as a major source of noise in subsonic axial flow fans and compressors. The interactions consist of fluctuating forces which arise because of the motion of the blade rows relative to one another, and in turn, act as acoustic sources. Out of practical necessity, little detailed attention can be paid to the interaction noise at the design stage, where each row is usually modeled as an isolated two-dimensional cascade in a steady undisturbed flow. Interactions can be kept to a minimum by spacing the rows several chord lengths apart, but the designer is generally working under size and weight constraints as well. This portion of the report presents the results to date of a combined theoretical and experimental program aimed at a better understanding of rotor-stator noise generation, and methods for its alleviation.

Many investigations have appeared in the literature which treat both the aerodynamic and/or acoustic aspects of the problem, e.g., References 2-26, which is by no means an all-inclusive list. Because of the complexity of the problem, the various theoretical models represent several combinations of simplifying assumptions needed to make them amenable to analysis. These include the use of free-field vs. ducted boundary conditions, two-dimensional vs. axisymmetric blade rows, and various degrees of approximation to the unsteady aerodynamic processes. Probably the most universal approximation, and the most restrictive, has been the use of incompressible flow theory to estimate the fluctuating blade loads. Strictly speaking, this restricts the range of validity of these models to very low flow speeds.

As the speeds of modern turbomachinery are definitely subsonic, and often transonic, the need to include compressibility effects is obvious. The goal of the present theoretical work is to incorporate a compressible flow aerodynamic model into the prediction of rotor/stator interaction noise. Published investigations, which allow for compressibility effects in the prediction of unsteady aerodynamic loads, include those by Kaji and Okazaki,<sup>22</sup> Mami,<sup>23</sup> Osborne,<sup>24</sup> Whitehead<sup>25</sup> and Fleeter.<sup>26</sup>



Kaji and Okazaki treat the near-field aerodynamic and far-field acoustic regions of the flow in a unified linearized treatment. Their analysis is the most complete because it includes the upwash velocities on each blade generated not only by the forces on that same blade, but also by the forces (both steady and unsteady) on all the other blades in that same row, as well as those from blades in the neighboring row. Unfortunately, this requires one to solve simultaneously for the loading distribution on both rows using a pair of coupled singular integral equations. Mani<sup>23</sup> simplified the problem somewhat by neglecting the influence of the unsteady loading on the neighboring row. It is still necessary to solve a pair of integral equations to obtain the unsteady loading on both rows, but the two are no longer coupled. Similarly, the aerodynamic analyses in References 25 and 26 require the numerical solution of an integral equation for the loading on each row. These analyses are all based on two-dimensional cascade models.

It is ultimately hoped that our work on the three-dimensional lifting surface theory for annular blade rows can be applied to the rotor-stator interaction problem. This would amount to the extension of the Kaji and Okazaki analysis to include three-dimensional effects, and is expected to lead again to a pair of coupled integral equations, probably even more complex than theirs. Hence, it is likely that more experience with the problems of steady and unsteady flow through an isolated rotor (reported on in Section IV, below) would be needed before applying such an analysis to rotor-stator interaction. In the interim, however, it was felt that our understanding of the basic mechanisms could benefit greatly from the application of a simpler model, and the comparison of its theoretical predictions against the acoustic data taken in the annular cascade (see Section II).

The theory developed under the current program avoids the necessity of solving integral equations, and thus considerably reduces the complexity of the analysis, as well as computing times. In this simplified model, the aerodynamic and acoustic problems are treated individually and then matched together. The aerodynamic analysis is that published by Osborne,<sup>24,27</sup> which essentially represents the compressible extension of the now classic analysis by Kemp and

Sears.<sup>2,5</sup> Osborne's results are closed form expressions for the unsteady blade loads on both rotor and stator which are easily accommodated in the acoustics calculation, since no numerical techniques are required. The principal features of this model are described in Section III-B below.

The Osborne aerodynamic analysis models each row as a two-dimensional cascade, which is strictly justifiable only at large hub/tip ratios; even then, McCune<sup>28</sup> has shown that in certain types of transonic flow, no logical two-dimensional cascade limit exists. The acoustic analysis described in Section III-A below employs axisymmetric annular blade rows housed in an infinite hard-walled cylindrical duct with a uniform axial flow. Accordingly, Osborne's expressions for the fluctuating loads are applied on a strip theory basis at each radial station. This procedure was followed so that in the event a truly three-dimensional aerodynamic analysis becomes available, it can more easily be incorporated in the model.

The combined aero-acoustic analysis in Section III-C results in easily evaluated expressions for the sound field in terms of the same duct modes studied previously by Tyler and Sofrin and Morfey.<sup>5,6</sup> A computer program has been written to evaluate the modal amplitudes in terms of blade row steady loadings, stagger angles and drag coefficients. From these amplitudes, the total radiated sound power (either upstream or downstream), as well as the mean square pressure at any given point in the duct may be obtained.

Section III-D contains comparisons made between the theoretical predictions and acoustic data taken in the annular cascade facility. Additional numerical results are presented in Section III-E to better illustrate the effects of compressibility. Section III-F summarizes the findings and makes suggestions as to how the theoretical model can be improved.

A. ACOUSTIC ANALYSIS

In the acoustic model studied, the blade rows are assumed to be housed in an infinitely long hard-walled cylindrical duct, as shown in Figure 11. The hub and tip radii are denoted by  $r_H$  and  $r_T$  respectively, and a uniform axial flow at Mach number  $M_x$  is assumed. In describing the flow field, we will use Lighthill's<sup>29</sup> acoustic analogy procedure as later extended by Curle<sup>30</sup> to allow for the presence of solid boundaries. That is, rather than having the blades impose boundary conditions on the equations of motion, we represent them as distributed sources of mass and momentum which arise from the blades' thickness and loading, and imagine the fluid to be otherwise unbounded in the annulus formed by the duct walls. The linearized, inviscid conservation equations of mass, momentum and energy in duct-fixed coordinates are then:

$$\frac{D\rho}{Dt} + \rho \nabla \cdot \vec{v} = Q \quad (1)$$

$$\rho \frac{D\vec{v}}{Dt} = -\nabla p + \vec{F} \quad (2)$$

$$\frac{D\rho}{Dt} = \frac{1}{a_0^2} \frac{Dp}{Dt} \quad (3)$$

Here  $\frac{D}{Dt}$  is the linearized substantial derivative

$$\frac{D}{Dt} \equiv \frac{\partial}{\partial t} + U_x \frac{\partial}{\partial x}$$

and  $\rho$ ,  $p$  and  $v$  are the perturbation density, pressure and velocity fields, respectively. The quantities  $a_0$  and  $U_x$  represent the undisturbed sound speed and the axial flow velocity, respectively.  $Q$  is the rate of introduction of mass per unit volume per unit time, and  $\vec{F}$  is a force per unit volume; both are functions of  $\vec{x}$  and  $t$ . Equations (1)-(3) are easily manipulated into the following form

$$\frac{1}{a_0^2} \frac{D^2 p}{Dt^2} - \nabla^2 p = \frac{DQ}{Dt} - \nabla \cdot \vec{F} \equiv S(\vec{x}, t) \quad (4)$$

The only boundary condition imposed on this equation is that the radial velocity vanish at the duct walls. Using Equation (2), this is expressed in terms of  $p$  as

$$\frac{\partial p}{\partial r} = 0 \quad \text{at} \quad r = r_H, r_T \quad (5)$$

In order for Equations (4) and (5) to be of any use, one must have a priori knowledge of the acoustic source distribution,  $S(\vec{x}, t)$ . This is discussed in the next section; for now we simply observe that solutions of (4) and (5) can be obtained using a number of methods. The present analysis uses a Fourier-Bessel transform decomposition. That is, we define transform variables  $p_{nm}(\zeta, \omega)$  and  $S_{nm}(\zeta, \omega)$ , corresponding to  $p(\vec{x}, t)$  and  $S(\vec{x}, t)$ , which are expressed in the cylindrical polar coordinates of Figure 11 as:

$$p_{nm}(\zeta, \omega) = \frac{1}{2\pi^2} \int_k^1 d\sigma R_{nm}(v_{nm}\sigma) \sigma \int_{-\infty}^{\infty} dt \int_{-\infty}^{\infty} dx e^{-i(\omega t + \zeta x)} \cdot \int_0^{2\pi} d\theta e^{-in\theta} p(r_T \sigma, \theta, x, t) \quad (6)$$

$$S_{nm}(\zeta, \omega) = \frac{1}{2\pi^2} \int_k^1 d\sigma R_{nm}(v_{nm}\sigma) \sigma \int_{-\infty}^{\infty} dt \int_{-\infty}^{\infty} dx e^{-i(\omega t + \zeta x)} \cdot \int_0^{2\pi} d\theta e^{-in\theta} S(r_T \sigma, \theta, x, t) \quad (7)$$

Here  $r = r/r_T$  is a convenient dimensionless radial variable and  $k = r_H/r_T$  is the hub/tip ratio. The functions  $R_{nm}(v_{nm}\sigma)$  are the set of orthonormal radial eigenfunctions imposed on the system by Equation (5); they are a linear combination of the Bessel and Neumann functions, and are described more fully in Appendix A. The corresponding eigenvalues,  $v_{nm}$ , are determined by the condition

$$R'_{nm}(v_{nm}k) = R'_{nm}(v_{nm}) = 0 \quad (8)$$

By substituting for  $p$  and  $S$  in Equation (4) in terms of the inverse transforms appropriate to (6) and (7), one can show that Equation (4) is then automatically satisfied when the transform variables have the following relationship to each other,

$$p_{nm} = S_{nm} (\beta^2 \xi^2 - 2M_x \xi k - k^2 + \mu_{nm}^2)^{-1} \quad (9)$$

where

$$k = \frac{\omega}{a_0} \quad \beta = (1 - M_x^2)^{1/2} \quad \mu_{nm} = \frac{v_{nm}}{r_T}$$

Thus, once  $S$  is known,  $S_{nm}$  and  $p_{nm}$  follow from Equations (7) and (9), respectively. The solution for the pressure field is then obtained as the inverse transform of Equation (6). Combining these steps we obtain,

$$p(\vec{x}, t) = \frac{1}{4\pi} \int_{-\infty}^{\infty} d\omega \int_{-\infty}^{\infty} d\xi e^{i(\omega t + \xi x)} \sum_{n=-\infty}^{\infty} \sum_{m=0}^{\infty} \frac{S_{nm}(\xi, \omega) R_{nm}(v_{nm} \sigma) e^{i n \theta}}{\beta^2 \xi^2 - 2M_x \xi k - k^2 + \mu_{nm}^2} \quad (10)$$

where everything on the right is presumed known. For the present study of rotor-stator interaction noise, we are concerned with the fluctuating forces, and so drop the source term  $Q$  appearing in Equation (4).

#### B. AERODYNAMIC MODEL

It remains then to specify the form of the unsteady forces  $\vec{F}$  exerted by the blades on the air. For the reasons discussed above, the linearized aerodynamic analysis of Osborne<sup>24</sup> was chosen for this purpose. Briefly stated, the principal assumptions in this analysis are:

- (1) Each blade is represented by a two-dimensional cascade in evaluating its induced velocity field.

- (2) The steady part of the circulation about each blade, and hence its influence on a neighboring blade row, is much greater than the unsteady circulation. The latter is neglected, along with any associated shed vorticity.
- (3) Unsteady velocity gusts parallel to the blade chord are neglected. This is safe provided the steady state angle of attack is small,<sup>31</sup> which is implicit in the linearization.
- (4) Isolated two-dimensional airfoil theory is used to estimate blade response to gusts perpendicular to the chord.<sup>27</sup>

As in the original analysis by Kemp and Sears, Osborne considers a single stage consisting of a stator followed by a rotor (see Figure 12a). Since we have assumed a uniform axial velocity in the duct as the undisturbed state in the acoustic model, the linearized analysis is strictly applicable only to stages with small stator stagger angles. Three interaction mechanisms are considered:

- (a) Rotor unsteady lift fluctuations due to its passage by the steady upstream stator loads.
- (b) Rotor unsteady lift due to its passage through the viscous wakes shed by the upstream stator.
- (c) Stator unsteady lift due to the passage of the steady rotor loads.

For brevity, items (a) and (c) are usually referred to as potential interactions since they would be present even if the fluid were ideal. Item (b), referred to as the viscous interaction, requires the presence of fluid friction. The potential interaction analysis involves the blade aerodynamic response to a generalized Kemp-type gust upwash, whereas the viscous interaction is modeled as the superposition of responses to a frozen sinusoidal gust.

The sectional lift per unit span on the zeroth blade given by Osborne for each of the above mechanisms may be symbolically expressed in blade-referenced coordinates as

$$L_R(t) = \frac{1}{2} \sum_{l=-\infty}^{\infty} X_l e^{i l \nu_R t} \quad (11a)$$

$$L_R(t) = \frac{1}{2} \sum_{l=-\infty}^{\infty} Y_l e^{i l \nu_R t} \quad (11b)$$

$$L_S(t) = \frac{1}{2} \sum_{l=-\infty}^{\infty} Z_l e^{i l \nu_S t} \quad (11c)$$

where  $X_{-l} = X_l^*$  and similarly for  $Y_l$  and  $Z_l$ .

The subscripts R and S refer to a blade member of the rotor and stator rows, respectively. Here and through Equation (17), the (a, b, c) suffix on equation numbers refers to their corresponding interactions (a, b, c) above. The  $X_l$ ,  $Y_l$ , and  $Z_l$  are the amplitudes of the fluctuation at each harmonic of the fundamental frequency, whether  $\nu_R$  or  $\nu_S$ . (Note: since we are not explicitly concerned here with the noise field generated by the steady rotor load, the  $l = 0$  term in [11a, b] is ignored.) These coefficients are given explicitly by Osborne as functions of blade row stagger, spacing and operating conditions. The full functional relationships would needlessly confuse the analysis that follows, and so they are given in Appendix B. Since Osborne's model is a two-dimensional one,  $X_l$ ,  $Y_l$  and  $Z_l$  are independent of spanwise location in his analysis; in the strip-wise application of his results to our annular duct model, they are assumed to be implicit functions of the radial coordinate  $r$  shown in Figure 11.

The fundamental frequencies  $\nu_R$  and  $\nu_S$  correspond to the radian frequency with which a rotor blade (stator vane) encounters a stator vane (rotor blade). In the cascade model, this is related to the rotor tangential velocity divided by the stator vane (rotor blade) spacing. In the present circular duct model, this translates into the product of the stator vane (rotor blade) number times the angular velocity of rotation, i.e.,

$$\nu_R = 2\pi \frac{r\Omega}{\alpha_S} = V\Omega, \quad \nu_S = 2\pi \frac{r\Omega}{\alpha_R} = B\Omega \quad (12)$$

where  $V$  and  $B$  are the numbers of vanes and blades, respectively,  $\alpha_S$  and  $\alpha_R$  their spacing, and  $\Omega$  is the shaft frequency in radians/sec.

### C. COMBINED AERO-ACOUSTIC ANALYSIS

Equation (4) shows that the contribution to the source distribution  $S(\vec{x}, \tau)$  from these fluctuating forces per unit span is in the form of minus the divergence of the fluctuating forces per unit volume, expressed in duct-fixed coordinates. That is, the blade rows are imagined replaced by a fictitious distribution of acoustic dipole singularities, stationary in duct coordinates, whose magnitude and phase are in accordance with Equations (11a-c). To determine this distribution, some assumption must be made regarding the spatial distribution of blade forces in the axial ( $x$ ) and azimuthal ( $\theta$ ) coordinates. For simplicity, we have initially assumed each blade (vane) to be represented by a line dipole located at its mid-chord. (More sophisticated models employing a chordwise distribution of loading can be treated, as this assumption is not crucial to the acoustic analysis.) Noting that Osborne takes the rotor as having velocity  $U (= \Omega r)$  in what we define as the negative  $\theta$  direction (Figure 12a), the fluctuating force field corresponding to Equations (11a-c) may then be expressed in duct-fixed coordinates as

$$\vec{F}_R(\vec{x}, t) = \frac{1}{2} \sum_{l=-\infty}^{\infty} x_l e^{-i l V \theta} \sum_{j=0}^{B-1} \delta\left(r\theta + r\Omega t - \frac{2\pi j r}{B}\right) \delta(x - x_R) \quad (13a)$$

$$\vec{F}_S(\vec{x}, t) = \frac{1}{2} \sum_{l=-\infty}^{\infty} y_l e^{-i l V \theta} \sum_{j=0}^{B-1} \delta\left(r\theta + r\Omega t - \frac{2\pi j r}{B}\right) \delta(x - x_S) \quad (13b)$$

$$\vec{F}_S(\vec{x}, \tau) = \frac{1}{2} \sum_{l=-\infty}^{\infty} z_l e^{i l B(\Omega t + \theta)} \sum_{j=0}^{B-1} \delta\left(r\theta - \frac{2\pi j r}{V}\right) \delta(x - x_S) \quad (13c)$$

where  $x_S$ ,  $x_R$  are the axial locations of the stator and rotor dipoles. The dipole axes are perpendicular to the rotor blade (stator vane) chord lines,



which, in turn, are inclined at an angle  $\alpha_R$  ( $\alpha_s$ ) from the axial direction, as in Figure 12a. Hence, the divergence of the forces occurring at the rotor can be shown to be (neglecting any contribution from the radial direction):

$$\nabla \cdot \vec{F}_R = \left( -\frac{\cos \alpha_R}{r} \frac{\partial}{\partial \theta} + \sin \alpha_R \frac{\partial}{\partial x} \right) |\vec{F}_R| \quad (14)$$

and for the stator,

$$\nabla \cdot \vec{F}_s = \left( -\frac{\cos \alpha_s}{r} \frac{\partial}{\partial \theta} - \sin \alpha_s \frac{\partial}{\partial x} \right) |\vec{F}_s| \quad (15)$$

Substitution of Equations (13a-c) into the above expressions gives the following contributions to  $S$  from each mechanism:

$$\begin{aligned} -\nabla \cdot \vec{F}_R &= \frac{1}{2r} \sum_{l=-\infty}^{\infty} X_l e^{ilV\theta} \left[ \frac{i l V \cos \alpha_R}{r} \sum_{j=0}^{B-1} \delta\left(\theta - \Omega t - \frac{2\pi j}{B}\right) \delta(x - x_R) \right. \\ &\quad \left. + \frac{\cos \alpha_R}{r} \sum_{j=0}^{B-1} \delta'\left(\theta - \Omega t - \frac{2\pi j}{B}\right) \delta(x - x_R) - \sin \alpha_R \sum_{j=0}^{B-1} \delta\left(\theta - \Omega t - \frac{2\pi j}{B}\right) \delta'(x - x_R) \right] \end{aligned} \quad (16a)$$

$$\begin{aligned} -\nabla \cdot \vec{F}_R &= \frac{1}{2r} \sum_{l=-\infty}^{\infty} Y_l e^{ilV\theta} \left[ \frac{i l V \cos \alpha_R}{r} \sum_{j=0}^{B-1} \delta\left(\theta - \Omega t - \frac{2\pi j}{B}\right) \delta(x - x_R) \right. \\ &\quad \left. + \frac{\cos \alpha_R}{r} \sum_{j=0}^{B-1} \delta'\left(\theta - \Omega t - \frac{2\pi j}{B}\right) \delta(x - x_R) - \sin \alpha_R \sum_{j=0}^{B-1} \delta\left(\theta - \Omega t - \frac{2\pi j}{B}\right) \delta'(x - x_R) \right] \end{aligned} \quad (16b)$$

$$\begin{aligned} -\nabla \cdot \vec{F}_s &= \frac{1}{2r} \sum_{l=-\infty}^{\infty} Z_l \sum_{j=0}^{B-1} e^{i(lB\Omega t + \frac{2\pi j l B}{V})} \left[ \frac{\cos \alpha_s}{r} \delta'\left(\theta - \frac{2\pi j}{B}\right) \delta(x - x_s) \right. \\ &\quad \left. + \sin \alpha_s \delta\left(\theta - \frac{2\pi j}{B}\right) \delta'(x - x_s) \right] \end{aligned} \quad (16c)$$

Substituting Equations (16a-c) in (7) then gives the expansion coefficients

$$S_{nm} = \frac{B}{2\pi} \int_{\frac{h}{2}}^{\frac{h}{2}} d\sigma R_{nm}(v_{nm}\sigma) \sum_{N=-\infty}^{\infty} x_l(r_T\sigma) e^{-i\zeta x_R} \left( \frac{n \cos \alpha_R}{r_T\sigma} - \zeta \sin \alpha_R \right) \cdot$$

$$\delta(\omega - NB\Omega) \quad l = \frac{NB-n}{V} \quad (17a)$$

$$S_{nm} = \frac{B}{2\pi} \int_{\frac{h}{2}}^{\frac{h}{2}} d\sigma R_{nm}(v_{nm}\sigma) \sum_{N=-\infty}^{\infty} y_l(r_T\sigma) e^{-i\zeta x_R} \left( \frac{n \cos \alpha_R}{r_T\sigma} - \zeta \sin \alpha_R \right) \cdot$$

$$\delta(\omega - NB\Omega) \quad l = \frac{NB-n}{V} \quad (17b)$$

$$S_{nm} = \frac{V}{2\pi} \int_{\frac{h}{2}}^{\frac{h}{2}} d\sigma R_{nm}(v_{nm}\sigma) \sum_{N=-\infty}^{\infty} z_l(r_T\sigma) e^{-i\zeta x_S} \left( \frac{n \cos \alpha_S}{r_T\sigma} + \zeta \sin \alpha_S \right) \cdot$$

$$\delta(\omega - lB\Omega) \quad l = \frac{n+NV}{B} \quad (17c)$$

where the sum over the integer  $N$  has replaced that over  $l$ . The notation  $\Sigma$  indicates that Equation (17) should be viewed as  $n$  being a fixed integer and allowing only those terms in the sum over  $N$  which give integral values of  $l$ . This restriction arises because of the following identity which is used in the derivation of Equations (17a) and (17b).

$$\sum_{j=0}^{B-1} e^{-i(lV+n)\frac{2\pi j}{B}} = \begin{cases} B & \text{WHEN } lV+n = NB \quad N = 0, \pm 1, \pm 2, \dots \\ 0 & \text{OTHERWISE} \end{cases}$$

Similarly, in the case of Equation (17c), use was made of

$$\sum_{j=0}^{V-1} e^{i(lB-n)\frac{2\pi j}{V}} = \begin{cases} V & \text{WHEN } lB-n = NV \quad N = 0, \pm 1, \pm 2, \dots \\ 0 & \text{OTHERWISE} \end{cases}$$

Physically, these identities reflect the phase cancellations in the duct which allow only a restricted set of loading harmonics to generate a given azimuthal mode.

## 1. Pressure Mode Amplitudes

Substitution of Equation (17) into (10) gives the desired solution for the acoustic pressure field. The integral over  $\omega$  is rendered trivial by the presence of the delta functions in Equation (17). The integral over  $\xi$  can be handled in a straightforward manner using contour integration in the complex  $\xi$  plane. The integrand exhibits two simple poles on the real axis. The physical requirement that all waves generated by a row should propagate away from it determines which half-plane the poles should be considered to lie in, and the value of the integral can then be found from residue theory.

For the sake of generality, pressure waves generated in the upstream direction by either row are referred to with a superscript "u", and those in the downstream direction with a "d". A subscript of either 1 or 2 will be used to denote whether they originated at the upstream or downstream blade row (see Figure 13). (In this simplified model, no allowance is made for the reflection or transmission of waves by a neighboring row once they are generated.) This formalism allows us to present results for either the stator-rotor case discussed thus far, or the rotor-stator case to be discussed shortly, within the same context. Then, each harmonic of the pressure field is found to consist of four sets of waves as given below:

$$p_1^d = \operatorname{Re} \sum_{n_1} \sum_{m_1} p_{n_1 m_1}^d R_{n_1 m_1}(v_{n_1 m_1}, \sigma) e^{in_1 \theta + i\omega t - i \left[ k_{n_1 m_1} - \frac{k M_x}{\beta^2} \right] x} \quad (18a)$$

$$p_2^d = \operatorname{Re} \sum_{n_2} \sum_{m_2} p_{n_2 m_2}^d R_{n_2 m_2}(v_{n_2 m_2}, \sigma) e^{in_2 \theta + i\omega t - i \left[ k_{n_2 m_2} - \frac{k M_x}{\beta^2} \right] x} \quad (18b)$$

$$p_1^u = \operatorname{Re} \sum_{n_1} \sum_{m_1} p_{n_1 m_1}^u R_{n_1 m_1}(v_{n_1 m_1}, \sigma) e^{in_1 \theta + i\omega t + i \left[ k_{n_1 m_1} + \frac{k M_x}{\beta^2} \right] x} \quad (18c)$$

$$p_2^u = \operatorname{Re} \sum_{n_2} \sum_{m_2} p_{n_2 m_2}^u R_{n_2 m_2}(v_{n_2 m_2}, \sigma) e^{in_2 \theta + i\omega t + i \left[ k_{n_2 m_2} + \frac{k M_x}{\beta^2} \right] x} \quad (18d)$$

where

$$\omega = N_f B \Omega > 0 \quad k_{nm} = \beta^{-2} \sqrt{k^2 - \beta^2 \mu_{nm}^2}$$

$N_f$  is the particular harmonic of blade passage frequency being considered. The values included in the sum over the azimuthal and radial mode numbers,  $n$  and  $m$ , will be discussed shortly. Equations (18a-d) hold regardless of the relative positions of the rotor and stator. This need not be specified until the mode amplitudes  $p_{n,m}^{u,d}$ , which are in general complex, are calculated. For the stator-rotor case discussed above, these are:

$$p_{n,m}^{u,d} = \frac{V}{4\pi r_T} \frac{e^{\mp i \left( \pm n, m, \pm \frac{M_x}{\beta^2} \right) x_S}}{\beta^2 \pm n, m} \int_{\frac{h}{2}}^1 R_{n,m}(v_{n,m}, \sigma) \left[ \frac{n, \beta^2 \cos \alpha_S}{r_T \sigma} \right. \\ \left. \mp \sin \alpha_S (\beta^2 \pm n, m, \pm M_x) \right] Z_{l_1}(\alpha_S, \alpha_R, U) d\sigma \quad (19a)$$

where

$$n_1 = l_1 \beta - NV; \quad l_1 = N_f; \quad N = 0, \pm 1, \pm 2 \dots$$

and

$$p_{n_2, m_2}^{u,d} = \frac{B}{4\pi r_T} \frac{e^{\mp i \left( \pm n_2, m_2, \pm \frac{M_x}{\beta^2} \right) x_R}}{\beta^2 \pm n_2, m_2} \int_{\frac{h}{2}}^1 R_{n_2, m_2}(v_{n_2, m_2}, \sigma) \left[ \frac{n_2 \beta^2 \cos \alpha_R}{r_T \sigma} \right. \\ \left. \mp \sin \alpha_R (\beta^2 \pm n_2, m_2, \pm M_x) \right] \left[ X_{l_2}(\alpha_S, \alpha_R, U) + Y_{l_2}(\alpha_S, \alpha_R, U) \right] d\sigma \quad (19b)$$

where

$$n_2 = NB - l_2 V; \quad N = N_f; \quad l_2 = \pm 1, \pm 2 \dots$$

The upper signs apply upstream, and the lower signs downstream.

In many applications, particularly high bypass ratio fans, the pertinent geometry is that of a rotor upstream of a stator (outlet guide vanes). The same three interactions (a, b, c) listed at the beginning of Section III-B are still involved, provided one interchanges the words rotor and stator. Rather than having to redo Osborne's entire analysis, the appropriate forces can be obtained from his present expressions using a simple transformation discussed in Appendix B, and the results written down directly:

$$p_{n,m_1}^{u,d} = \frac{B}{4\pi r_T} \frac{e^{\mp i(k_{n,m_1} \pm \frac{k M_x}{\beta^2}) x_R}}{\beta^2 k_{n,m_1}} \int_k^1 R_{n,m_1}(v_{n,m_1}, \sigma) \left[ \frac{n_1 \beta^2 \cos \alpha_R}{r_T \sigma} \right. \\ \left. \mp \sin \alpha_R (\beta^2 k_{n,m_1} \pm k M_x) \right] Z_{l_1}(-\alpha_R, -\alpha_s, -U) d\sigma \quad (19c)$$

where

$$n_1 = NB - l_1 V; \quad N = N_f; \quad l_1 = \pm 1, \pm 2 \dots$$

and

$$p_{n_2, m_2}^{u,d} = \frac{V}{4\pi r_T} \frac{e^{\mp i(k_{n_2, m_2} \pm \frac{k M_x}{\beta^2}) x_S}}{\beta^2 k_{n_2, m_2}} \int_k^1 R_{n_2, m_2}(v_{n_2, m_2}, \sigma) \left[ \frac{n_2 \beta^2 \cos \alpha_s}{r_T \sigma} \right. \\ \left. \pm \sin \alpha_s (\beta^2 k_{n_2, m_2} \pm k M_x) \right] \left[ X_{l_2}(-\alpha_R, -\alpha_s, -U) + Y_{l_2}(-\alpha_R, -\alpha_s, -U) \right] d\sigma \quad (19d)$$

where

$$n_2 = l_2 B - NV; \quad l_2 = N_f; \quad N = 0, \pm 1, \pm 2 \dots$$

Equations (18a-d) express the pressure field as the superposition of the same spiral duct modes studied by Tyler and Sofrin,<sup>4</sup> and Morfey.<sup>5,6</sup> Note that the rotor-generated field is made up of modes with azimuthal order

$N_f B - lV$ , where  $N_f B \Omega$  is the acoustic frequency and  $lV \Omega$  the blade loading frequency. The stator-generated field on the other hand is composed of modes with azimuthal order  $lB - NV$ , where both the acoustic and vane loading frequencies =  $lB \Omega = N_f B \Omega$ . These rules for determining the azimuthal modes over which one must sum in Equations (18a-d) are a result of the delta functions involving  $\omega$  in Equation (17) in conjunction with the special relationships between  $n$ ,  $N$  and  $l$  given there. Interestingly, one can see that the rotor and stator always will each excite the same set of  $\{n, m\}$  modes. These observations hold irrespective of which is the upstream row.

Here we are concerned only with the radiated field, and so only those modes above cut-off, i.e., for which  $k_{nm}$  is real, need be considered. This allows one to put an upper limit on the value of the radial index  $m$ , for a given frequency  $\omega$  and azimuthal mode number  $n$ . (The form of the result for modes which are cut off is the same as (18), except that  $k_{nm}$  is then imaginary; its sign is determined from the physical requirement that the mode decay, rather than grow, exponentially.)

The mode amplitudes given by Equations (19a-d) are singular right at the cutoff condition for any one mode,  $k = k_{nm}$ , as first reported by McCune<sup>28</sup> in his study of the disturbances generated by the steady loading on an isolated rotor. In References 22, 23 and 25, which treat the aerodynamic and acoustic fields simultaneously in a two-dimensional cascade model, no such resonance is predicted since the unsteady loads (which we have assumed as given a priori) apparently vanish at this condition, due to a strong interaction between the two fields. The experimental results discussed below and in Section II, however, indicate that the sound levels are significantly higher near such a condition.

## 2. Sound Pressure Level and Total Radiated Power

Once the pressure mode amplitudes,  $p_{nm}^{u,d}$ , have been determined from Equation (19), expressions for both the mean square pressure at any point in the duct and the total radiated power are easily derived for any given frequency. We denote time averages over one blade passage interval by  $\langle \rangle$ . Then since everything is harmonic in time,

$$\langle p^2 \rangle^{u,d} = \frac{|p_{nm}^{u,d}|^2}{2} \quad (20)$$

where

$$p^{u,d} = p_1^{u,d} + p_2^{u,d} \quad (21)$$

and  $|p^{u,d}|$  is the magnitude of the sum of the signals from both rows, i.e., the coefficient of  $e^{-i\omega t}$  in Equation (21), after substituting from (18) and (19) as appropriate. The result is easily shown to be:

$$\begin{aligned}
 \langle p^2 \rangle^{u,d} &= \frac{1}{2} \left| \sum_{n_1, m_1} p_{n_1, m_1}^{u,d} R_{n_1, m_1}(r_{n_1, m_1}, \sigma) e^{i(n_1 \theta \pm l(\star_{n_1, m_1} \pm \frac{\star M_x}{\beta^2}))} \right. \\
 &\quad \left. + \sum_{n_2, m_2} p_{n_2, m_2}^{u,d} R_{n_2, m_2}(r_{n_2, m_2}, \sigma) e^{i(n_2 \theta \pm l(\star_{n_2, m_2} \pm \frac{\star M_x}{\beta^2}))} \right|^2 \quad (22) \\
 &= \frac{1}{2} \left| \sum_{n_1 = n_2} \sum_{m_1 = m_2} (p_{n_1, m_1}^{u,d} + p_{n_2, m_2}^{u,d}) R_{n_1, m_1}(r_{n_1, m_1}, \sigma) e^{i(n_1 \theta \pm l(\star_{n_1, m_1} \pm \frac{\star M_x}{\beta^2}))} \right|^2
 \end{aligned}$$

The last equality follows from the fact that the two blade rows always excite the same set of  $\{n, m\}$  modes, (but with different amplitudes, of course). Note that  $\langle p^2 \rangle^{u,d}$  is a function of  $x, r = r_r \sigma$ , and  $\theta$ , but is independent of time; the dependence on  $x$  and  $\theta$  will also disappear in situations where only one mode is excited. The sound pressure level, SPL, then follows from

$$SPL = 10 \log_{10} \frac{\langle p^2 \rangle^{u,d}}{p_{REF}^2} \quad (23)$$

where  $p_{REF} = 2 \times 10^{-4}$  dyne/cm<sup>2</sup>

To obtain the total sound power radiated along the duct,  $P^{u,d}$ , we must evaluate (Reference 6)

$$P^{u,d} = r_T^2 \int_0^1 \int_0^{2\pi} \left[ (1 + M_x^2) \langle p u \rangle^{u,d} + \rho_0 a_0 M_x \langle u^2 \rangle^{u,d} + \frac{M_x}{\rho_0 a_0} \langle p^2 \rangle^{u,d} \right] \sigma d\sigma d\theta \quad (24)$$

where  $u$  is the axial component of the acoustic perturbation velocity. The last term is proportional to the integral of Equation (22) over the duct cross-section; it simplifies considerably due to the orthogonality properties of the trigonometric and Bessel functions and the fact that, for two complex quantities,

$$A = |A| \exp(i \arg A) \text{ and } B = |B| \exp(i \arg B)$$

$$AB^* + BA^* = 2 |A| |B| \cos(\arg A - \arg B)$$

The integral of  $\langle p^2 \rangle^{u,d}$  then reduces to

$$\frac{1}{2} \sum_{n_1=n_2} \sum_{m_1=m_2} \left[ |p_{n_1 m_1}^{u,d}|^2 + |p_{n_2 m_2}^{u,d}|^2 + 2 |p_{n_1 m_1}^{u,d}| |p_{n_2 m_2}^{u,d}| \cos(\arg p_{n_1 m_1}^{u,d} - \arg p_{n_2 m_2}^{u,d}) \right] \quad (25)$$

The other terms in Equation (24) involve the axial velocity in some form. For every pressure wave with amplitude  $p_{nm}^{u,d}$  there is a corresponding velocity wave with the same spatial and time dependence and an amplitude of, say,  $u_{nm}^{u,d}$ . The two amplitudes can be related through the axial component of the momentum equation:

$$\frac{\partial u}{\partial t} + a_0 M_x \frac{\partial u}{\partial x} = - \frac{1}{\rho_0} \frac{\partial p}{\partial x} \quad (26)$$

which requires that

$$u_{nm}^{u,d} = \frac{A_{nm}^{u,d}}{\rho_0 a_0} p_{nm}^{u,d} \quad A_{nm}^{u,d} = \frac{\mp \beta^2 k_{nm} - k M_x}{k \pm \beta^2 M_x k_{nm}} \quad (27)$$

The quantity  $A_{nm}^{u,d}$  may be thought of as the dimensionless acoustic admittance of an  $(n,m)$  mode. For the plane wave mode with no axial flow,  $n=m=M_x=0$ , it reduces to  $\mp 1$ , as expected. Since  $A_{nm}^{u,d}$  is a real, constant multiplicative factor independent of  $x, r$  and  $\theta$ , the contributions to  $p^{u,d}$  from the first two terms in Equation (24) can be written down directly from (25).

The complete result can then be reduced to:

$$P^{u,d} = \frac{\pi r_T^2}{\rho_0 a_0} \sum_{n_1=n_2} \sum_{m_1=m_2} \left[ (1 + M_x^2) A_{n_1 m_1}^{u,d} + (1 + A_{n_1 m_1}^{u,d 2}) M_x \right] \left[ |p_{n_1 m_1}^{u,d}|^2 + |p_{n_2 m_2}^{u,d}|^2 + 2 |p_{n_1 m_1}^{u,d}| |p_{n_2 m_2}^{u,d}| \cos(\arg p_{n_1 m_1}^{u,d} - \arg p_{n_2 m_2}^{u,d}) \right] \quad (28)$$

which is written in such a way that  $P^u$  and  $P^d$  are both positive, i.e., power is always radiated away from the stage.



The terms involving the squares of the mode amplitudes represent the power put out independently by each blade row, assuming only its radiation was present. The last term represents an interference between waves emanating from the separate rows; this would be zero if the two blade rows radiated independently of one another, i.e. if  $(\arg p_{n_1, m_1}^{u, d} - \arg p_{n_2, m_2}^{u, d})$  were random.

If the acoustic interference effect is sufficiently strong, it may be possible to "tune" the rotor-stator stage to minimize radiation at a given frequency by adjusting the inter-row separation  $|x_r - x_s|$  (see Equation (19)). To achieve maximum benefit, Equation (28) indicates that  $|p_{n_1, m_1}^{u, d}|$  should approximately equal  $|p_{n_2, m_2}^{u, d}|$ . However, most modern turbofans are designed with maximum rotor-stator separation, subject to size and weight constraints. This usually results in negligible potential interactions between rows (they decay exponentially); practically all the noise then results from the viscous wake impingement on the downstream row, i.e., in our notation,  $|p_{n_2, m_2}^{u, d}| \gg |p_{n_1, m_1}^{u, d}|$ . These arguments suggest that moving the rows closer together until they play roughly equal roles may lead to noise reduction at a given frequency, if their signals can be made to destructively interfere. This would probably be useful only in situations where the acoustic field was dominated by a single mode. Whether the benefits of such a scheme could be realized in practice would depend on several factors not included in the present model. One would also have to consider if such an optimum separation would have an adverse affect on the other harmonics in the spectrum.

Useful qualitative conclusions regarding the variations in upstream and downstream radiated power which result from changes in axial Mach number and frequency can also be drawn from Equation (28). The arguments below apply to radiation from a single rotor as well as from a rotor-stator pair, due to the absence of transmission and reflection effects of the other row. Hence for the sake of simplicity imagine the mode amplitudes of one row, say the rotor, to be dominant over those of the other row. First we consider the situation with no mean flow. In this case, Equation (27) shows

$$\lim_{M_x \rightarrow 0} A_{nm}^{u,d} = \mp \frac{k_{nm}}{k} \quad (29)$$

and the power contained in any one  $n,m$  mode, call it  $P_{nm}^{u,d}$ , is proportional to (from Equation (28)):

$$\lim_{M_x \rightarrow 0} P_{nm}^{u,d} \propto \frac{k_{nm}}{k} |p_{nm}^{u,d}|^2 \quad (30)$$

Now, from Equation (19) we see that the only thing differentiating  $|p_{nm}^{u,d}|$  from  $|p_{nm}^d|$  is the sign of that term in the integrand beginning with  $\sin \alpha_R$ . If the integrand is not very sensitive to variations in radius, Equation (30) can then be written approximately as

$$\lim_{M_x \rightarrow 0} P_{nm}^{u,d} \propto \frac{k_{nm}}{k} \left| \frac{\frac{n \cot \alpha_R}{r_T \sigma} \mp k_{nm}}{k_{nm}} \right|^2$$

which, after some re-arrangement gives

$$\lim_{M_x \rightarrow 0} \frac{P_{nm}^d}{P_{nm}^u} = \left| \frac{\frac{n \cot \alpha_R}{k r_T \sigma} + \sqrt{1 - \left(\frac{\mu_{nm}}{k}\right)^2}}{\frac{n \cot \alpha_R}{k r_T \sigma} - \sqrt{1 - \left(\frac{\mu_{nm}}{k}\right)^2}} \right|^2 \neq 1 \quad (31)$$

This result is in agreement with that of Morfey in Equation (69) of Reference 6, if there one sets  $M_x = 0$ , interchanges  $n$  and  $m$ , and notes that in his notation,  $\epsilon/k a_0$  equals  $\cot \alpha_R / (k r_T \sigma)$  in ours. Equation (31) indicates that even when  $M_x = 0$ , equal amounts of power do not radiate to either side of the blade row. This results from the fact that the relative angle between the dipole axis and the propagation vectors of the acoustic mode, say  $\phi_{nm}^{u,d}$ , is different on the two sides of the blade row. The situation is shown schematically in Figure 14.

The geometry of Figure 14 suggests that this asymmetry in radiated power should disappear for modes propagating very near the duct axis, which happens well above cut-off. In this case

$$\frac{\mu_{nm}}{k} = \frac{v_{nm}}{k r_T} \sim \frac{n}{k r_T} \rightarrow 0 \quad k_{nm} \rightarrow k \quad (32)$$

and the ratio in Equation (31) approaches unity.

In fact, this can be shown to be true in the more general case with axial flow; Equation (27) then yields,

$$\lim_{\beta^2 k_{nm} \rightarrow k} A_{nm}^{u,d} = \mp 1 \quad (33)$$

The first factor in Equation (28) then becomes

$$\lim_{\beta^2 k_{nm} \rightarrow k} \left[ (1 + i^2 M_x^2) A_{nm}^{u,d} + (1 + A_{nm}^{u,d 2}) M_x \right] = (1 \mp M_x)^2$$

and it can be shown, again using Equations (19) and (32), that

$$\lim_{\beta^2 k_{nm} \rightarrow k} p_{nm}^{u,d} \propto (1 - M_x^2)^2 \quad (34)$$

Hence, while  $p_{nm}^u$  and  $p_{nm}^d$  will still depend individually on  $M_x$ , their ratio

$$\lim_{\beta^2 k_{nm} \rightarrow k} \frac{p_{nm}^d}{p_{nm}^u} = 1 \quad (35)$$

will always approach unity for modes well above cut-off, again in agreement with Reference 6. Care should be taken not to apply this result very near the condition of transonic axial flow,  $M_x = 1$ . Here the upstream radiated power will vanish, whereas that in the downstream direction remains finite, in violation of Equation (35). This is because the linearized analysis on which these results are based is invalid right at the transonic condition.

#### D. COMPARISONS OF THEORY WITH EXPERIMENT AND DISCUSSION

This section presents comparisons between numerical predictions from a computer program based on the preceding analysis and the acoustic data described in Section II. Unfortunately, as pointed out in the discussion of Section II, acoustic data could be obtained only for the fourth and fifth

harmonics of blade passing frequency. As seen below, this seriously hampers one's ability to draw meaningful conclusions concerning the model's validity.

The basic inputs required by the computer program are the geometries of the two blade rows, the steady lift on each of the blades, and the drag coefficient of the upstream row, which in the case of the present experiments, is the rotor. Since at the speeds encountered in the experiment compressibility effects should be negligible, and the hub/tip ratio is large, a two-dimensional incompressible theory can be used to relate the lift and drag on each blade to the turning performance and viscous losses across each row. For example, Horlock<sup>32</sup> has shown that the drag coefficient,  $C_D$ , of each blade is related to the total pressure loss coefficient,  $\Delta C_{pT}$ , by the following

$$C_D = \Delta C_{pT} \frac{d}{2c} \cos^3 \beta_m \quad (36)$$

where

$$C_D = \frac{\text{DRAG / SPAN}}{\rho V_m^2 c} \quad (37)$$

$$\Delta C_{pT} = \frac{\text{TOTAL PRESSURE LOSS ACROSS ROW}}{\frac{1}{2} \rho U_x^2} \quad (38)$$

$\beta_m$  is the mean flow angle,  $d$  the blade spacing,  $c$  the semi-chord, and  $\rho$  the fluid density. It is important to note that  $\beta_m$  and the total pressure loss must be measured in coordinates fixed to the blade row. Since  $\cos \beta_m = \frac{U_x}{V_m}$ ,  $V_m$  being the vector mean of the velocities upstream and downstream of the blade row, and  $d = \frac{2\pi r}{B}$  Equation (36) becomes:

$$C_D = \frac{\pi \Delta C_{pTR} r}{Bc} \left( \frac{U_x}{V_m} \right)^3 \quad (39)$$

where  $B$  is the number of blades and everything on the right hand side is either known or measured.

Also, the lift coefficient on each blade,  $C_L$ , can be obtained from the turning performance through:

$$C_L = \frac{d}{c} (\tan \beta_1 - \tan \beta_2) \cos \beta_m - C_D \tan \beta_m \quad (40)$$

where  $\beta_1$  and  $\beta_2$  are the upstream and downstream flow angles, respectively.

Letting

$$v_{1,2} = U_x \tan \beta_{1,2} \quad v_m = \frac{v_1 + v_2}{2} \quad (41)$$

where  $v_1$  and  $v_2$  are the tangential flow velocities, again measured relative to the row, and substituting for  $d$ ,  $\beta_m$  and  $C_D$  from above, we obtain

$$C_L = \frac{\pi r}{Bc} \left[ \frac{2(v_1 - v_2)}{v_m} - \frac{v_m U_x^2}{v_m^3} \Delta C_{Pr} \right] \quad (42)$$

Now the lift force is actually put into the rotor-stator interaction noise program in the form of the Glauert coefficients  $A_n$ , required by Osborne's theory (see Appendix B). The first two of these,  $A_0$  and  $A_1$ , are respectively the blade angle of attack and the ratio of maximum camber to blade semi-chord, assuming a circular-arc profile. They are related to  $C_L$  by

$$C_L = 2\pi (A_0 + A_1) \quad (43)$$

Since the angle of attack  $A_0$  is simply the mean flow angle minus the known geometric blade stagger angle, Equations (42) and (43) are sufficient to determine  $A_1$ ; for  $n$  greater than one, the  $A_n$  are assumed to be zero. In this way the  $A_n$  are computed in such a manner as to use the actually measured steady loads in the Osborne theory.

For the present acoustic experiments all quantities on the right hand side of Equations (39)-(43) are either known or measured in the case of the rotor, for which data were taken over a wide range of conditions in the previous program.<sup>1</sup> Unfortunately, since stator performance data were obtained near rotating stall inception, they do not include the range of inlet conditions covered by the present experiments. Consequently, stator turning performance was inferred from design data made available by the manufacturer for the corresponding stator in the complete J-79 engine. The outlet flow

angle at design was assumed to apply for all incidence angles away from the design value (corresponding to a high solidity approximation). The outlet angles at the off-design stator stagger angles used here were assumed to differ from the design value by the same amount as the stagger angle differed from the design stagger angle. Viscous losses were assumed negligible for the stator; this is a safe assumption since  $\Delta C_{p_r}$  has a relatively weak influence in Equation (42) and the  $C_D$  of Equation (39) is not needed for the downstream row. The rotor mid-chord location was chosen as  $\chi_R = 0$ . Hence, the coordinates of the probe in Figure 1 were  $\chi = -.979$  ft.,  $r = r_r = 1.223$  ft., and  $\theta = 0^\circ$ .

Due to the large hub/tip ratio of about 0.8, the dimensionless steady lift and drag coefficients used by the program were input as constants independent of radius. These were computed from the radially averaged turning and loss data of Reference 1. The lift and drag forces do, of course, vary with radius, because all the velocities scale with the rotational speed,  $\Omega r$ . To check the validity of using the radially averaged coefficients, one case was also run with a four-point radial distribution of these coefficients (also measured in Reference 1). This produced only minor differences in the results.

Figure 15 compares the experimental measurements of r.m.s. wall pressure described in Section 11 for the fourth harmonic of blade passage frequency with the computer predictions for the mean stator stagger angle of  $37.2^\circ$ . The axial flow velocity and rotor rpm were varied in such a way that the relative rotor inlet angle, and hence also turning performance, of both rows was held constant for all conditions shown. Figure 16 shows the same comparison for a mean stator stagger angle of  $28.2^\circ$ .

The comparison of absolute levels is seen to be rather poor, although the shapes of both curves are in general agreement. For example, in Figure 15 both experimental and theoretical curves are characterized by two rather well defined peaks, at approximately 1170 and 1445 rpm in the experiment, and 1150 and 1415 rpm in the theory. Similar behavior is exhibited in Figure 16. As

explained under the discussion of Section II, discrete-tone noise signals could be obtained only at the fourth and higher harmonics of blade passage frequency in the accessible rpm range of the annular cascade experiments. The left hand peak in the theoretical curve corresponds to the operating point where the  $n = 22$  azimuthal and  $m = 1$  radial order mode for the fourth harmonic of blade passage frequency exceeds the theoretical cut-off condition and begins to propagate. The peak at the higher rpm corresponds to where the  $n = 22$ ,  $m = 2$  mode begins to propagate. These peaks are a result of the acoustic resonance that occurs at the cut-off frequency of any mode, due to the vanishing of  $k_{nm}$  in the denominator of the modal amplitudes  $p_{nm}^{u,d}$  (see Equation (19)). The height of the theoretical curve is limited only by the precision of the computer. The level and shape of the experimental peaks in these regions are heavily influenced by factors not included in the idealized model, e.g., non-linearities, viscous effects, and radial variations in axial velocity. In view of this a small discrepancy between the locations of the experimental and theoretical peaks, here about 20 rpm, is to be expected.

Note that the pressure levels rose slightly from Figure 15 to Figure 16, probably a result of tilting the stator load vector closer to the angle of propagation of the acoustic mode, as well as a modest increase in flow velocity. Again, it is encouraging to note in this regard that theory and experiment rose by roughly the same amount.

Figure 17 contains limited data for the fifth harmonic noise of the same rotor-stator pair as Figure 16. The fifth harmonic excites propagating modes at a much lower rpm. In this case only the  $n = 14$ ,  $m = 1$  mode is present, the rpm at which it theoretically exceeds cut-off being just to the left of that shown in the figure. Here, the shapes of the two curves are only marginally similar, and the discrepancy in absolute levels is even wider than in Figures 15 and 16.

This discrepancy in absolute level between theory and experiment bears further discussion. For the experimental rotor-stator stage having 46 blades in the rotor and 54 blades in the stator, the  $n = 22$ ,  $m = 1$ ,

2 modes in Figures 15 and 16 are generated by the third loading harmonic on the rotor in concert with the fourth loading harmonic on the stator (see Equations (19c, d)). Moreover, computer results indicate that at these conditions the potential interactions between rows are negligibly small in comparison with the viscous interaction. Hence, the question is reduced to how well the model can predict the noise resulting from the fourth loading harmonic on the stator induced by its passage through the rotor viscous wakes. (Figure 17 involves the fifth harmonic of stator loading, and hence is an even more severe test of the model.) Since the velocities involved are all low enough to be considered incompressible, we are essentially dealing with the original Kemp-Sears model<sup>2,3</sup> to which Osborne's analysis reduces in this limit. It is felt that the following are the most likely sources of the discrepancy:

- Poor modeling of the viscous wake defect at the higher harmonics
- Inaccuracies in turning performance and loss data used as inputs
- Inadequacy of strip-wise application of isolated airfoil theory in predicting unsteady loads

Each of these is discussed individually below, beginning with the last.

The ad hoc application of a strip theory aerodynamic analysis for predicting unsteady loads in a three-dimensional annular flow is open to question, although the large hub/tip ratio and large number of blades in this case would seem to justify it. Also, since the solidity ratio,  $2c/a$  is near unity, the use of isolated airfoil theory in estimating these loads introduces some error. These questions are particularly crucial with respect to phase variations in loading along the span, as these critically affect the radial integration involved in the modal pressure amplitudes,  $p_{nm}^{u,d}$  in Equation (19). It is difficult to assess the importance of these approximations in the absence of any experimental data on the load fluctuations, or a truly three-dimensional annular cascade theory for unsteady flow through a blade row.



The inaccuracy involved in estimating the steady loading and viscous losses on the rows is also difficult to assess. The principle reason is that such data as were obtained were measured with the row operating in isolation, since at the time their use in the present investigation was not envisioned. Hence, the performance of both rows may have been somewhat different from that assumed. This could significantly affect the potential interactions. Since these were found to be negligible as noise sources at these conditions, a strong variation in loading would probably be needed to appreciably change the acoustic predictions. The prediction of viscous wake interaction, however, might have been considerably improved if more detailed knowledge of the blade wake structure had been available. This is discussed at more length below.

With regard to the wake modeling, both Osborne's analysis and the previous work of Kemp and Sears made use of empirical laws for the wake width and velocity defect suggested by Silverstein et al,<sup>33</sup> based on isolated air-foil data. In particular the decay of the wake centerline dynamic pressure,  $q_c$ , is assumed to follow

$$\frac{q_c}{q_\infty} = 1 - \frac{4.84 \sqrt{C_D}}{\frac{x}{c} - 0.4} \quad (44)$$

where  $q_\infty$  is the free-stream dynamic pressure,  $x$  the distance downstream of the blade mid-chord position, and  $c$  the semi-chord. From this, the centerline velocity defect,  $u_c$ , was inferred, assuming it to be a small perturbation of the free-stream flow. In the present experimental configuration, there is roughly a one semi-chord separation between the rotor trailing edge and the leading edge of the stator. Equation (39), in conjunction with the loss data, indicates a rotor  $C_D$  of 0.16. For such a high drag coefficient, Equation (44) predicts a negative value of dynamic pressure, and is clearly inapplicable.

Partially for this reason, and also because it was felt that the radially averaged loss data were perhaps unduly influenced by viscous losses at the inner and outer duct walls, the value of  $C_D$  used in the calculations presented here was lowered to 0.10. To indicate the uncertainty involved in

estimating  $u_c$ , an alternate correlation proposed by Dittmar (Reference 17 Equation (7)), and based in part on the cascade data of Lieblein and Roudebush,<sup>34</sup> was evaluated for the same conditions. It indicated an increase in  $u_c$  by a factor of about 1.6. Since the unsteady loading is proportional to  $u_c$ , and only one mode is propagating over most of Figures 15 and 16, one would expect this to raise the theoretical SPL by about 4 dB.

In addition to this uncertainty, a surprising variation was noted in the calculations. That is, when  $C_D$  was lowered from .16 to .10, there was a rise in the predicted viscous interaction force, and hence duct wall pressure, in sharp contrast to the conclusion of Kemp and Sears<sup>3</sup> that such loading appears to be linearly proportional to  $C_D$ . The observed behavior can be traced to an exponential factor in the load prediction (see Appendix B (c)) whose argument is proportional to minus the product of  $C_D$  times the square of the load harmonic index. Clearly, for the high drag coefficient and load harmonic index of interest here, this exponential decay dominates any linear variation.

The above anomalous behavior strongly suggests that the viscous wakes are not modeled accurately enough to predict the higher loading harmonics on the downstream row when the rotor and stator are in close proximity to one another, and the wake structure is accordingly changing rapidly. Table I further supports this contention. The first two entries in the first column give the velocity defect profile assumed by Kemp-Sears-Osborne,<sup>3,24</sup> and that originally suggested by Silverstein et al, as a fit to their isolated airfoil data. Here  $u$  is the velocity defect at any distance  $y$  from the wake centerline, and  $Y$  is the wake half-width. The last entry is suggested by the present authors as fitting the Silverstein data nearly as well, at least within the experimental scatter of about  $\pm 10$  in  $u/u_c$  shown in Figure 42 of Reference 33. All three are normalized in such a way as to produce the same total momentum defect in the wake flow. The second column gives the relative magnitude of the  $l$ th harmonic in the Fourier expansion of an infinite train of such pulses spaced a distance  $d_s$  apart. Since this is the only change that would be involved if a different profile were assumed, the influence on the theoretical predictions can be easily assessed. The first entry is the exponential discussed

Table 1  
COMPARATIVE INFLUENCE OF VARIOUS WAKE PROFILES ON ACOUSTIC PREDICTIONS

Source	Profile	Harmonic Factor	Relative Change in SPL From Kemp-Sears-Osborne Model
Kemp-Sears <sup>3</sup> Osborne <sup>24</sup>	$e^{-\pi (y/Y)^2}$	$e^{-\pi \left( \frac{dY}{d_s \cos \alpha_s} \right)^2}$	$\ell = 1$ (dB)      4      10 (dB)      (dB)      (dB)
Silverstein et al <sup>33</sup>	$\cos^2 \left( \frac{\pi}{2} \frac{y}{Y} \right)$	$\sin \frac{2\pi dY}{d_s \cos \alpha_s} / \frac{2\pi dY}{d_s \cos \alpha_s} \left( 1 - \frac{2.0Y}{d_s \cos \alpha_s} \right)^2$	+3      -5.2      +137
Alternate	$\text{sech} \pi \frac{y}{Y}$	$\text{sech} \frac{\pi dY}{d_s \cos \alpha_s}$	-0.8      +7.8      +126

above, but written in terms of  $Y$  rather than  $C_D$  for the sake of simplicity. The next two entries show how this factor would change if one or the other of the substitute profiles had been assumed. The resulting changes in the predictions are shown in the last column for  $Y/\alpha_s \cos \alpha_s$  (actually  $Y/\alpha_R \cos \alpha_R$  for the present case of a rotor-stator) = .2653 appropriate to the present conditions, and the first, fourth, and tenth loading harmonics. Note that the first harmonic is relatively insensitive to the choice of profile, but at higher values of  $l$  such as needed here, the choice is critical. Had the last profile been used in the calculations, in conjunction with the alternate estimate of  $\omega_c$  discussed above, it is seen that the theoretical curve in Figure 15 would be almost 12 dB higher.

It would be presumptuous to suggest that this constitutes a better model for the wake properties in the present case, or any other, simply because it correlates better with our acoustic data. But it is clear that the prediction of higher harmonics is too sensitive to the details of wake structure to be reliable, and for these we have had to rely on isolated airfoil data. Moreover, recent experimental work<sup>20,35,56</sup> has shown that the wake properties for cascaded airfoils and rotor blades can differ significantly from those for an isolated airfoil. Hence it is felt likely that the theory could benefit from a refined viscous wake model which better reflects the true situation. Also, if they should prove possible, comparisons of the theory against acoustic data for the lower harmonics in the spectrum would be very valuable. These are less sensitive to detailed changes in wake structure, and would allow a better assessment of the validity of other portions of the theoretical model.

#### E. ADDITIONAL NUMERICAL RESULTS

In addition to the above comparisons with experiment, which all involve incompressible flow, some calculations have been performed to show the influence of compressibility on the radiated noise. One of the test cases presented by Clark, et al. (Reference 19, Vol. III, p. 59) involved the calculation of the upstream pressure amplitudes generated by the potential interaction on the upstream stator of an inlet stator-rotor pair. The present

program was run using the same input conditions as given there (see test case #2, subroutine package AAB/A). Briefly, the stator and rotor were housed in an annular duct with hub/tip ratio of .35, and axial Mach number of 0.5. The rotor (15 blades) had a tip Mach number of .875 and was located a distance  $r_1/5$  downstream of the stator (10 vanes). In this case the potential interaction on the upstream stator was dominant. The amplitudes

$$2\pi^2 |p_{n,m}^{u,d}| / \rho_0 a_0^2$$

as used by Clark, et al.<sup>19</sup> are compared with the present predictions in Table 2.

Table 2

COMPARISON OF MODAL AMPLITUDES COMPUTED BY CLARK ET AL.<sup>19</sup>  
WITH PRESENT THEORY

n	m	Clark et al. <sup>19</sup>	Present Theory
-5	1	$4.72 \times 10^{-3}$	$8.92 \times 10^{-3}$
	2	$3.14 \times 10^{-2}$	$2.05 \times 10^{-2}$
	3	$7.46 \times 10^{-2}$	$3.83 \times 10^{-2}$
+5	1	$1.54 \times 10^{-2}$	$5.36 \times 10^{-3}$
	2	$5.07 \times 10^{-2}$	$1.91 \times 10^{-2}$
	3	$8.94 \times 10^{-2}$	$3.84 \times 10^{-2}$

This particular calculation in Reference 19 also assumed a line dipole model for the blades, and so the differences in the predicted values are largely a result of using the Osborne rather than Kemp-Sears aerodynamic analysis. As one might expect, the inclusion of compressibility (the relative Mach number at the stator was about 0.5) had a noticeable effect, generally decreasing the modal amplitudes.

In the acoustic experiments performed under the current program, the fundamental blade passing tone could not propagate owing to power constraints in the annular cascade (see Section II). However, calculations indicate that it should begin to propagate above roughly 1700 rpm. To study its behavior, and give some idea of how the theoretical predictions vary over a wider range of conditions than those above, the calculations in Figure 18 are presented. The inputs are the same as in Figure 15, except that the rpm and  $M_x$  were increased, again proportionately, into the subsonic regime. Thus, when this tone first begins to propagate at the left of the figure, the relative Mach numbers of the rotor and stator are approximately .15 and .11, respectively. When 8700 rpm is reached, these are .77 and .56, and the first four radial modes of the  $n = -8$  circumferential mode are propagating. The rpm at which each of these starts to propagate is shown at the bottom of the figure.

The upper curve gives the variation in SPL at the same location as before. As expected, there is a large increase in signal over the fourth harmonic of Figure 15. The lower curve in Figure 18 is the total power radiated in the upstream direction. Straight line segments have been used to connect the computed points for ease of visualization only, and should not be assumed to accurately depict the true curve. The curves exhibit a rise just above each cut-off frequency, due to the acoustic resonance for that mode, as discussed previously; again it should be emphasized that the levels computed very near these frequencies are open to question because they represent singular points in the solution. In fact, the rise becomes harder to resolve as rpm is increased. This results because as increasingly higher order radial modes get turned on, the integrand in the radial integration in Equation (19) oscillates more. The value of the integral itself thus approaches zero, and so one must be extremely close to the cut-off frequency before the pressure amplitude begins to diverge.

The behavior of the SPL curve in Figure 18 is much more unpredictable than that in Figure 15. This is because over most of the rpm range more than one mode is propagating, and so the interference between modes described by Equation (22) comes into play. No doubt at some other point in the duct this

curve would look quite different, due to its complicated dependence on observer position and frequency. At the higher rpm values the curve begins to smooth out somewhat, probably because as the signal is distributed amongst more modes, the constructive and destructive interferences tend to cancel one another.

The curve representing total radiated power is much more well behaved, since it represents an integral over the duct cross section, thus removing any dependence on position. With the exception of the resonance peaks, it exhibits a smooth rise as relative velocity is increased, as expected. The interference effects between waves from the rotor and stator described by Equation (28) do not arise, since the computer results again indicate that  $p_{n_2, m_2}^4 \gg p_{n_1, m_1}^4$ . The leveling off and subsequent decay of the curve in the higher rpm region is not surprising. Upstream radiated power must go to zero as a sonic axial flow velocity is approached; hence the presence of a maximum in the subsonic regime is to be expected. However, as Osborne's theory becomes more approximate as the relative Mach number is increased, whether the location of the peak is accurately predicted is open to question. Subsequent to the completion of the present work, Amiet<sup>37</sup> presented an approximate analysis of compressible unsteady airfoil theory which also makes use of asymptotic techniques. His analysis complements Osborne's in that it becomes more exact as the Mach number and/or reduced frequency increases, and so should prove useful in the higher subsonic regime.

The computing time needed to generate the numerical results in Sections III-D, E above on an IBM 370/168 varied between approximately 1 and 10 seconds per point, depending primarily on the number of propagating modes.

#### F. CONCLUDING REMARKS

A compressible two-dimensional analysis of the aerodynamic forces generated by rotor-stator interaction has been matched, on a strip-theory basis, to the well known three-dimensional annular duct acoustic modes. Expressions have been derived for both the mean square pressure at any position in the duct

and the total power radiated at harmonics of blade passage frequency. The mean square pressure signal is seen to be subject to interferences between the various propagating modes. The total radiated power is the sum of independent contributions from each mode, but is still subject to interference effects between waves generated by each row within the same mode. These are evaluated easily on a computer in terms of stage operating conditions and geometry.

Experimental acoustic data were taken in the annular cascade facility, as described under Section II, to provide a means of assessing the validity of the theoretical model. Data on blade row steady-state performance and losses had been taken in the annular cascade facility under a previous program. These were used as inputs to the theory to calculate SPL at the outer wall, and the results were compared with the acoustic data for two configurations of a rotor-stator pair. Unfortunately, power constraints in the rig allowed only the fourth and higher harmonics to be studied, which is felt to be a rather severe test of the theory. Although it was able to predict cutoff frequencies and follow trends in the data adequately, the theory significantly underestimated absolute levels.

The most likely source for the discrepancy is felt to be in the viscous wake modeling, which at present is based on isolated airfoil data. Recent experimental work by others has suggested that the structure of cascade and rotor wakes can be significantly different, and this is expected to have a strong influence on the higher harmonics. It is felt that the theoretical model could benefit from a closer examination of such cascade or rotor wake data as are available, as well as an improved aerodynamic load model at high reduced frequencies and Mach numbers.<sup>37</sup> It is also hoped to obtain more acoustic data in the annular cascade facility, which has been repowered and will now allow the propagation of lower harmonics in the spectrum.



SECTION IV  
DIRECT LIFTING SURFACE THEORY FOR A COMPRESSOR ROTOR

Increased emphasis on reduction of the size, weight, and noise output of axial flow turbomachinery demands improved understanding of the flow through high-speed fan and compressor blade rows. As more detailed questions are asked about modern blade row performance, the essentially three-dimensional character of the flow takes on increased importance. The task of calculating the fully nonlinear, three-dimensional, viscous flow through interacting blade rows is a formidable one indeed. Consequently, some approximations are required in order to obtain a tractable model, the most familiar being the idealization of inviscid flow through a two-dimensional cascade. A linearized analysis of the steady, inviscid, three-dimensional flow through an isolated rotor contains important features not present in the corresponding two-dimensional cascade approximation. For example, though restricted to lightly loaded, thin blades, it does include disturbances induced by the trailing vortex wakes which result from spanwise variations in the blade circulation. Also, modern fans and compressors often operate with a transonic inflow that is subsonic over the inner portion of the blade span and supersonic over the outer portion. At Mach numbers where shock losses are small, the linearized, three-dimensional analysis remains valid, but it does not have a well-defined two-dimensional limit.<sup>28</sup>

The small-perturbation approach to three-dimensional compressor flows was pioneered by McCune<sup>28,41</sup> who, in the spirit of linearized wing theory, separated the thickness and loading contributions to the rotor disturbance field. In his original papers, McCune treated the thickness problem for the subsonic, transonic, and supersonic flow regimes. Later, Okurounmu and McCune<sup>42,43</sup> employed a vortex representation of the blade row to solve the indirect lifting problem, i.e., that in which the disturbance field, along with the blade geometry needed to produce it, are determined from a prescribed distribution of blade loading. Lordi<sup>44,45</sup> has investigated the acoustic implications of both of these analyses; the sound radiation from an isolated rotor operating at supersonic tip speeds was evaluated for various thickness and loading distributions.

While the thickness and loading contributions to the rotor disturbance field can be treated separately in the linearized analysis, they are not entirely independent. In order that there be no loading contribution to the flow field associated with a given distribution of blade thickness, this thickness must be distributed about an unknown camber line. The camber lines required for the rotor to be unloaded must be determined as part of the solution to the thickness problem, in much the same way as the camber lines corresponding to a specified loading distribution are computed. Erickson, Lordi, and Rae<sup>46</sup> presented results for thickness-induced camber lines at high subsonic tip speeds. They also have computed the camber lines required to produce given loading distributions, as have Okurcunmu and McCune.<sup>43</sup>

A major objective of the present program has been to develop a linearized analysis of the direct lifting surface problem for the compressible, three-dimensional flow through a rotor row. In contrast to the indirect loading problem, the direct problem refers to the situation where the blade incidence and camber lines are given, and the resulting blade loading must be determined. Once the blade loading is known, the evaluation of the rotor flow field is accomplished in the same way as in the indirect case. The solution of the direct problem, together with the existing solution of the thickness problem, would permit computation of the aerodynamic and acoustic performance for a rotor row of given geometry at specified operating conditions. In addition to providing a predictive capability for steady flow at off-design conditions, the successful analysis of the direct lifting surface problem provides the basis for examining three-dimensional flows which are unsteady in rotor coordinates.

In the thickness and indirect-loading analyses, the flow field quantities are found by evaluation of integrals which express the superposition of the appropriate singularity solutions e.g., sources in the thickness case and vortices in the loading case. However, direct lifting surface calculations entail the solution of an integral equation, which for a ducted rotor has a very complicated kernel function. Some progress on the direct

loading problem has been reported by other investigators. Dharwadkar and McCune<sup>47</sup> have obtained a solution using a lifting-line approximation. Namba<sup>48,49</sup> has reported a direct lifting surface analysis including some numerical examples. Namba's approach closely parallels that presented here and frequent reference to it is made throughout the report.

Our initial approach to the direct lifting surface problem was to generalize the formal relationships between the blade camber lines and the blade loadings which were derived in Reference 46. In this way, an integral equation for the blade loading was obtained in the framework of the vortex theory of Okurounmu and McCune.<sup>42</sup> This formulation of the direct lifting surface theory produced an integral equation which not only contained the expected complexities in the kernel function, but moreover would require repeated evaluations of both ordinary and modified Bessel functions of large order. The appearance of both kinds of Bessel functions is a consequence of the way in which the trailing vortex wakes are handled separately from the bound vorticity at the blade surfaces.

At this point, an alternative formulation of the lifting surface problem was sought by using a pressure dipole rather than a vortex representation of the blade surfaces. In principle, the two approaches should result in the same governing integral equation for the blade loading. However, it was felt that an alternative derivation, as is often the case in potential theory for complicated geometries, would yield an alternative form for the result. A simpler form did indeed result from the pressure dipole approach, the main difference being the absence of the modified Bessel functions of large order which appear in the vortex formulation.

At about the time we began to pursue the pressure dipole representation, Namba's initial report<sup>48</sup> appeared. There are important differences between our formulation and his. Furthermore, the initial solution for the

pressure field which we obtained with the dipole representation failed to yield correct limits. In particular, the pressure rise between points far upstream and downstream of the rotor did not agree with that from the vortex theory, or with Namba's version of the dipole formulation. These discrepancies prompted a complete review of our analysis. A crucial revision has been made in the pressure dipole solution which led to a limiting pressure rise across a lifting rotor that now agrees with the vortex theory result, but still differs from Namba's.

In the material which follows, a detailed account is given of the linearized solution for the three-dimensional, compressible flow through a rotor. This formalism is presented not only because of its relevance to establishing the correct integral equation in a direct lifting surface theory, but also because of its general importance to other aspects of the flow through rotating blade rows. In Section IV-A, the derivation of the linearized equations is reviewed and a formal solution of them is obtained based on Green's theorem. In Section IV-B solutions are found for the disturbance fields of a point source of mass and a pressure dipole. Next these singularity solutions are used as the Green's functions to determine the flow fields produced by rotor thickness and loading distributions. Discussion of the thickness contribution is included here because of its role in deriving a correct solution for the entire flow field, and also to point out omissions in earlier results. In the respective presentations of the thickness and loading solutions in Sections IV-C and IV-D, the flow fields are shown to display the correct discontinuous behavior across the blade surfaces and trailing vortex wakes. Demonstrations that the results for a mass source, a pressure dipole, and the thickness and loading problems satisfy global mass and momentum balances appropriate to the noninertial reference frame are collected in Appendix C. In the final part of the main text, Section IV-E, the governing integral equation for the direct lifting surface theory is derived and the progress made on its solution is reported.

A. DERIVATION OF MODEL EQUATIONS AND GREEN'S FUNCTION SOLUTION

In this section, the linearized equations and a formal integral representation of their solution are developed for the flow through an isolated rotor row in an infinitely long annular duct. The key assumptions in the analysis are that the undisturbed axial velocity is uniform and subsonic, and that the disturbance field of the rotor is a small perturbation about the resulting helical inflow seen by an observer in blade-fixed coordinates. Both compressibility and three-dimensional effects are included. While not a fundamental restriction in the analysis, attention is confined to subsonic relative tip speeds. The required extensions to supersonic tip speeds are indicated at several points in the derivations. As a consequence of the linearization, the blade surface boundary conditions can be separated into thickness and camber line contributions and their associated flow field solutions superimposed to find the overall disturbance field. This separation is effected by requiring the rotor blades to be locally unloaded in the thickness case and by assuming that the blades have vanishing thickness in the loading case.

The geometry of the blade-fixed coordinates is illustrated in Figure 19 for a rotor rotating in the negative  $\theta$  direction with angular velocity  $\omega$ . The full nonlinear equations for the flow through such a blade row in a cylindrical coordinate system fixed to the rotor have been given by Wu.<sup>50</sup> These equations can be linearized by writing the velocity in blade-fixed coordinates as

$$\vec{W} = \vec{U}_R + \vec{v} \quad (45)$$

where  $\vec{U}_R$  is the undisturbed velocity,

$$\vec{U}_R = U \vec{e}_z + \omega r \vec{e}_\theta \quad (46)$$

and  $\vec{v}$  is the perturbation velocity with components  $v_r$ ,  $v_\theta$ ,  $v_z$ . The fluid pressure and density are expanded in a similar way; the undisturbed quantities are denoted by  $p_\infty$  and  $\rho_\infty$ , the perturbation quantities by  $p$  and  $\rho$ . Substituting these definitions into Wu's equations and linearizing the result by

neglecting the products of perturbation quantities leads to the following vector forms of the steady flow continuity and momentum equations, to first order.

$$\bar{U}_R \cdot \nabla \rho + \rho_\infty (\nabla \cdot \bar{v}) = 0 \quad (47)$$

$$(\bar{v} \cdot \nabla) \bar{U}_R + (\bar{U}_R \cdot \nabla) \bar{v} + 2\omega (v_\theta \bar{e}_r - v_r \bar{e}_\theta) = -\frac{1}{\rho_\infty} \nabla p \quad (48)$$

Paying careful attention to the proper differentiation of the unit vectors, the component form of the momentum equation can be expressed as

$$\rho_\infty U_R \frac{\partial v_r}{\partial S} = -\frac{\partial p}{\partial r} \quad (49a)$$

$$\rho_\infty U_R \frac{\partial v_\theta}{\partial S} = -\frac{1}{r} \frac{\partial p}{\partial \theta} \quad (49b)$$

$$\rho_\infty U_R \frac{\partial v_z}{\partial S} = -\frac{\partial p}{\partial z} \quad (49c)$$

where  $U_R = \sqrt{U^2 + \omega^2 r^2}$  and  $S$  is the coordinate along the helical undisturbed streamlines.

From this basic set of conservation equations, we can develop the governing equations for either the perturbation pressure or the velocity potential, the solutions of which can then be used to obtain the remaining flow field quantities. First, the  $\theta$  and  $z$  components of the momentum equations are cast in terms of distance along the undisturbed streamlines and the direction normal to the streamline and radial directions. Unit vectors in these directions, which are illustrated in Figure 20, are

$$\bar{s} = \bar{e}_\theta \sin \psi + \bar{e}_z \cos \psi \quad (50a)$$

$$\bar{n} = \bar{e}_\theta \cos \psi - \bar{e}_z \sin \psi \quad (50b)$$

where  $\psi = \tan^{-1} \omega r / U$ . The directional derivatives along  $\bar{s}$  and  $\bar{n}$  are related to the partial derivatives with respect to  $\theta$  and  $z$  by

$$\frac{\partial}{\partial s} = \frac{1}{\sqrt{1 + \left(\frac{\omega r}{U}\right)^2}} \left( \frac{\omega}{U} \frac{\partial}{\partial \theta} + \frac{\partial}{\partial z} \right) \quad (51a)$$

$$\frac{\partial}{\partial n} = \frac{1}{\sqrt{1 + \left(\frac{\omega r}{U}\right)^2}} \left( \frac{1}{r} \frac{\partial}{\partial \theta} - \frac{\omega r}{U} \frac{\partial}{\partial z} \right) \quad (51b)$$

With these results the  $s$  and  $n$  components of the linearized momentum equations become

$$\rho_{\infty} U_R \frac{\partial v_s}{\partial s} = - \frac{\partial p}{\partial s} \quad (52a)$$

$$\rho_{\infty} U_R \frac{\partial v_n}{\partial s} = - \frac{\partial p}{\partial n} \quad (52b)$$

This form of the linearized momentum equations is useful in relating results for the pressure and velocity fields. For subsonic flow where disturbances decay far upstream, Eq. (52a) can be integrated along the streamlines to obtain

$$p = -\rho_{\infty} U_R v_s \quad (53)$$

The normal momentum equation, Eq. (52b), plays a central role in the direct lifting surface theory. It contains the upwash velocity,  $v_n$ , which is related to the blade camber line in order to derive the integral equation for the blade loading. The above equations have the same appearance as their counterparts in isolated airfoil theory because the linearized substantial derivative,  $U_R \frac{\partial}{\partial s}$ , is independent of radius. It should be noted that the noninertial acceleration terms enter only through the curvature of the undisturbed streamlines.

The governing equation for the perturbation pressure is derived by introducing the assumption that the disturbance flow is isentropic so that

$$p = a_{\infty}^2 \rho \quad (54)$$

where  $a_\infty$  is the undisturbed sound speed. Using this relationship to eliminate the density, and then combining  $U_R \frac{\partial}{\partial S}$  of the linearized continuity equation with the divergence of the momentum equation leads to

$$\nabla^2 p - \frac{U_R^2}{a_\infty^2} \frac{\partial^2 p}{\partial S^2} = 0 \quad (55)$$

There are several ways to demonstrate that the velocity potential satisfies the same governing differential equation. McCune,<sup>41</sup> starting in fluid-fixed coordinates where the disturbance potential satisfies the wave equation, obtains this result by transformation to the blade-fixed system. Wu<sup>50</sup> derives the nonlinear potential equation which, when linearized, reduces to the same result. Here we note that the linearized momentum equations, in the streamline-normal coordinates, indicate that the velocity components are proportional to the gradient of the integral of the pressure along the undisturbed streamlines, a scalar function. Accordingly, a scalar velocity potential, defined such that  $\vec{v} = \nabla \phi$ , is introduced into Eqs. (47) and (52a), the results may be combined with Eq. (54) to obtain

$$\nabla^2 \phi - \frac{U_R^2}{a_\infty^2} \frac{\partial^2 \phi}{\partial S^2} = 0 \quad (56)$$

This equation is the same as that given for  $p$  in Eq. (55), and when expressed in cylindrical coordinates leads to the same form of the governing equation for the velocity potential that McCune<sup>41</sup> obtained.

The formal solution of the governing differential equation for  $\phi$  (or  $p$ ) is derived from Green's theorem, which states that<sup>51</sup> for two scalar functions  $\phi$  and  $G$ ,

$$\int_S \left( G \frac{\partial \phi}{\partial \nu} - \phi \frac{\partial G}{\partial \nu} \right) dS = - \int_V (G \nabla^2 \phi - \phi \nabla^2 G) dV \quad (57)$$

where the surface  $S$  encloses the volume  $V$  and  $\vec{\nu}$  is the normal to the surface  $S$  directed into  $V$ . The following development, while carried out for the velocity potential applies as well to the pressure perturbation. As shown



above,  $\phi$  satisfies the equation  $L\phi = 0$  where the operator  $L$  is defined by

$$L = \nabla^2 - M_R^2 \frac{\partial^2}{\partial s^2} \quad (55)$$

and where we have introduced the undisturbed relative Mach number seen in blade-fixed coordinates,  $M_R = U_R/a_\infty$ . If we eliminate  $\nabla^2$  in terms of the operator  $L$  in Green's theorem, we get

$$\int_S \left( G \frac{\partial \phi}{\partial \nu} - \phi \frac{\partial G}{\partial \nu} \right) dS = - \int_V (GL\phi - \phi LG) dV - \int_V \left( GM_R^2 \frac{\partial^2 \phi}{\partial s^2} - \phi M_R^2 \frac{\partial^2 G}{\partial s^2} \right) dV \quad (59)$$

The second volume integral on the right-hand side can be rewritten as

$$\int_V \left( GM_R^2 \frac{\partial^2 \phi}{\partial s^2} - \phi M_R^2 \frac{\partial^2 G}{\partial s^2} \right) dV = \int_V M_R \frac{\partial}{\partial s} \left( GM_R \frac{\partial \phi}{\partial s} - \phi M_R \frac{\partial G}{\partial s} \right) dV \quad (60)$$

In this form, the volume integral can be converted to a surface integral by applying the divergence theorem to the product of a scalar function  $\Phi$  and a vector  $\vec{A}$ .

$$\int_V (\nabla \cdot \vec{A}) \Phi dV + \int_V (\vec{A} \cdot \nabla) \Phi dV = - \int_S \vec{\nu} \cdot (\vec{A} \Phi) dS \quad (61)$$

The volume integrals in the divergence theorem can be identified with the volume integral on the right-hand side of Eq. (60) if

$$\Phi = GM_R \frac{\partial \phi}{\partial s} - \phi M_R \frac{\partial G}{\partial s} \quad (62)$$

and

$$\vec{A} = M_R \vec{s} \quad (63)$$

where the cylindrical-coordinate form of Eq. (63) readily shows that  $\nabla \cdot \vec{A}$  vanishes. Using Eqs. (61)-(63) in Eq. (60), Green's theorem takes the form

$$\int_S \left( G \frac{\partial \phi}{\partial \nu} - \phi \frac{\partial G}{\partial \nu} \right) dS = - \int_V (GL\phi - \phi LG) dV + \int_S \vec{\nu} \cdot (\vec{A} \Phi) dS \quad (64)$$

where  $\vec{\Phi}$  and  $\vec{A}$  are given by Eqs. (62) and (63).

This relationship can be used to express the velocity potential in terms of surface integrals which bound the region of solution by the usual Green's function technique. The scalar function  $G$  in Eq. (64) is chosen to be the Green's function having the property that it is the solution to the governing differential equation for a point disturbance. If  $\vec{r}$  and  $\vec{r}_0$  denote the observation point and the source point,  $G(\vec{r}, \vec{r}_0)$  satisfies the equation

$$L G(\vec{r}, \vec{r}_0) = \delta(\vec{r} - \vec{r}_0) \quad (65)$$

where  $\delta$  denotes the Dirac delta function. If the integrations in Eq. (64) are taken to be over the source coordinates, and within the region of interest  $L_0 \phi(\vec{r}_0) = 0$ , then the following integral expression is obtained for the velocity potential.

$$\phi(\vec{r}) = \int_V \left[ G(\vec{r}, \vec{r}_0) \frac{\partial \phi}{\partial \nu_0} - \phi(\vec{r}_0) \frac{\partial G}{\partial \nu_0} \right] dS_0 - \int_S [\vec{\nu}_0 \cdot (A \vec{\Phi})_0] dS_0 \quad (66)$$

The term  $\phi(\vec{r})$  is the result of integrating  $\phi(\vec{r}_0) L_0 G(\vec{r}, \vec{r}_0)$  over the volume, which requires that the Green's function determined from Eq. (65) also has the property

$$L_0 G(\vec{r}, \vec{r}_0) = \delta(\vec{r}_0 - \vec{r}) \quad (67)$$

An alternative approach to the integration over the region containing the singular point, which may be more rigorous, is to exclude this point from the volume integral by surrounding it with a vanishingly small surface. Then the functions  $\phi$  and  $G$  are continuous and differentiable throughout the region of interest, and the volume integral in Eq. (64) vanishes. However, there would then be a contribution from the integration over the surface enclosing the point  $\vec{r} = \vec{r}_0$ . It has been demonstrated, using the Green's function determined in the subsequent section, that the integral over such a surface yields the same result as the volume integral over the delta function. Throughout the derivations which follow, the generalized function approach is used to handle point singularities because the presentations are thereby shortened considerably.

In the present application, the surfaces over which the integrations must be done in Eq. (66) include the blade surfaces, the duct walls, and the surfaces normal to the duct axis at large distances upstream and downstream of the blade row. The evaluation of the surface integrals is simplified considerably through the use of a Green's function which satisfies the same boundary conditions at the duct walls as the velocity potential. Then the surface integrals over the duct walls vanish identically and, in a direct parallel with isolated wing theory, the velocity potential for a rotor can be found by superimposing the solutions for singularities which are distributed only over the blade surfaces. The Green's function  $G(\vec{r}, \vec{r}_0)$  can be identified with a mass source, and then  $\frac{\partial G}{\partial \nu_0}$  corresponds to a fluid doublet. In the linearized analysis, where thickness and loading effects are separable, the source solutions can be used to represent the flow about a nonlifting rotor and the doublet solutions employed for a lifting rotor. However, it is more convenient to treat the loading case in terms of the perturbation pressure because the blade boundary conditions are expressed in a simpler form and further, integration over the blade wakes is avoided. Since the perturbation pressure satisfies the same equation as the velocity potential, the formal solution given in Eq. (66) also applies to the pressure field. Here the Green's function is interpreted as a pressure monopole and it, in turn, is differentiated to find the disturbance field of a pressure dipole. The pressure field of a lifting rotor can then be found by superposition of the pressure dipole solution.

In the next section, the solutions for a point source of mass and a pressure dipole are found for the ducted geometry.

#### B. MASS SOURCE AND PRESSURE DIPOLE SOLUTIONS

The governing differential equation for the velocity potential given in Eq. (56) can be expressed in cylindrical coordinates by using Eq. (51a). Then, the velocity potential due to a source located at  $r_0, \theta_0, z_0$  in a

rotating reference frame and having a mass addition rate of  $\rho_\infty Q$  satisfies the equation

$$\beta^2 \frac{\partial^2 \phi}{\partial z^2} + \frac{1}{r} \frac{\partial}{\partial r} \left( r \frac{\partial \phi}{\partial r} \right) + \left( \frac{1}{r^2} - \frac{\omega^2}{a_\infty^2} \right) \frac{\partial^2 \phi}{\partial \theta^2} - \frac{2\omega M}{a_\infty} \frac{\partial^2 \phi}{\partial z \partial \theta} \quad (68)$$

$$= Q \frac{\delta(r-r_0) \delta(\theta-\theta_0) \delta(z-z_0)}{r}$$

where  $M$  is the Mach number based on the undisturbed axial velocity,  $U/a_\infty$ , and  $\beta^2 = 1 - M^2$ . In this form the homogeneous equation is separable and, as originally shown by McCune,<sup>41</sup> it possesses the following eigenfunction solutions when the boundary condition of no flow through the walls is enforced.

$$\phi_n = e^{in\theta} e^{in \frac{M^2 \omega z}{\beta^2} \pm \lambda_{n\pm} \frac{\omega z}{U}} R_{n\pm}(K_{n\pm} \sigma) \quad (69)$$

The quantity  $R_{n\pm}$  is a normalized combination of the Bessel and Neumann functions of order  $n$  as described in Appendix A and  $\sigma = r/r_T$ .  $K_{n\pm}$  is the  $n^{\text{th}}$  eigenvalue of the equations which result from the boundary condition that  $\partial \phi / \partial r$  vanish at the duct walls,

$$R'_{n\pm}(K_{n\pm}) = R'_{n\pm}(1) = 0 \quad (70)$$

where  $K_{n\pm} = \lambda_{n\pm} r_T$ . The quantity  $\lambda_{n\pm}$  is defined by

$$\lambda_{n\pm} = \frac{nU}{\omega r_T \beta^2} \sqrt{\beta^2 \left( \frac{K_{n\pm}}{n} \right)^2 - M_T^2} \quad (71)$$

with  $M_T = \omega r_T / a_\infty$ . Transformed to duct-fixed coordinates, these homogeneous solutions represent the duct acoustic modes; Eq. (71) contains the so-called cutoff condition for the propagation of these modes. When  $M_T > \beta(K_{n\pm}/n)$ ,  $\lambda_{n\pm}$  becomes imaginary and the solutions in Eq. (69) correspond to propagating waves. The cutoff condition can be stated approximately as requiring that the relative Mach number at the tip radius must be supersonic for the source to excite propagating modes. Here we restrict attention to the subsonic case where the modes decay with distance from the source.

In order to solve Eq. (68) the form of Eq. (69) suggests we assume an expansion for  $\varphi$  of the form

$$\varphi_s = \sum_{n=-\infty}^{\infty} \sum_{k=k_1}^{\infty} \varphi_{nk}(z) e^{in(\theta-\theta_0)} R_{nk}(K_{nk}\sigma) \quad (72)$$

where  $\varphi_s$  will denote the solution for a mass source. Here  $k_1 = 1$  for  $n > 0$  but  $k_1 = 0$  for  $n = 0$  in order to include the nontrivial zero eigenvalue required to make the zeroth-order Bessel functions a complete set. In addition we introduce the expansions of the delta functions in terms of the azimuthal and radial eigenfunctions.

$$\delta(\theta - \theta_0) = \frac{1}{2\pi} \sum_{n=-\infty}^{\infty} e^{in(\theta-\theta_0)} \quad (73a)$$

$$\frac{\delta(r - r_0)}{r} = \frac{1}{r_T^2} \sum_{k=1}^{\infty} R_{nk}(K_{nk}\sigma_0) R_{nk}(K_{nk}\sigma) \quad n \neq 0 \quad (73b)$$

$$\frac{\delta(r - r_0)}{r} = \frac{2}{(1 - k^2)r_T^2} + \frac{1}{r_T^2} \sum_{k=1}^{\infty} R_{0k}(K_{0k}\sigma_0) R_{0k}(K_{0k}\sigma) \quad n = 0 \quad (73c)$$

Substituting these expansions into Eq. (68), using the differential equation satisfied by the radial eigenfunctions,

$$\frac{1}{r} \frac{d}{dr} \left( r \frac{dR_{nk}}{dr} \right) + \left( \frac{K_{nk}^2}{r_T^2} - \frac{n^2}{r^2} \right) R_{nk} = 0 \quad (74)$$

and making use of the orthogonality properties of the azimuthal and radial eigenfunctions leads to

$$\beta^2 \frac{\partial^2 \varphi_{nk}}{\partial z^2} - \frac{2in\omega M}{a_m} \frac{\partial \varphi_{nk}}{\partial z} + \left( \frac{n^2 \omega^2}{v_{s0}^2} - \frac{K_{nk}^2}{r_T^2} \right) \varphi_{nk} = \frac{Q R_{nk}(\sigma_0)}{2\pi r_T^2} \delta(z - z_0) \quad (75)$$

where  $R_{nk}(\sigma_0)$  is introduced as a shortened notation for  $R_{nk}(K_{nk}\sigma_0)$ .

The solution of this equation for  $\varphi_{nk}(z)$  can be found using Fourier transform techniques. With the following definition of a transform pair

$$\bar{\varphi}_{n\star}(\xi) = \frac{1}{2\pi} \int_{-\infty}^{\infty} e^{-i\xi z} \varphi_{n\star}(z) dz \quad (76a)$$

$$\varphi_{n\star}(z) = \int_{-\infty}^{\infty} e^{i\xi z} \bar{\varphi}_{n\star}(\xi) d\xi \quad (76b)$$

taking the transform of Eq. (75) yields

$$\left[ -\beta^2 \xi^2 + \frac{2n\omega M}{a_\infty} \xi + \left( \frac{n^2 \omega^2}{a_\infty^2} - \frac{K_{n\star}^2}{r_T^2} \right) \right] \bar{\varphi}_{n\star} = Q \frac{R_{n\star}(\sigma_0) e^{-i\xi z_0}}{4\pi^2 r_T^2} \quad (77)$$

Solving for  $\bar{\varphi}_{n\star}$  and taking the inverse transform,

$$\varphi_{n\star}(z) = -\frac{Q R_{n\star}(\sigma_0)}{4\pi^2 r_T^2 \beta^2} \int_{-\infty}^{\infty} \frac{e^{i\xi(z-z_0)}}{\xi^2 - \frac{2n\omega M}{\beta^2 a_\infty} \xi + \frac{1}{\beta^2} \left( \frac{K_{n\star}^2}{r_T^2} - \frac{n^2 \omega^2}{a_\infty^2} \right)} d\xi \quad (78)$$

The integral in Eq. (78) can be evaluated by residue theory, the roots of the denominator being

$$\xi_{n\star}^{\pm} = \frac{n\omega M}{\beta^2 a_\infty} \pm i \frac{n}{\beta^2 r_T} \sqrt{\beta^2 \left( \frac{K_{n\star}}{n} \right)^2 - \left( \frac{\omega r_T}{a_\infty} \right)^2} \quad (79)$$

For  $z > z_0$ , the contour is closed in the upper half-plane and encloses the pole at  $\xi = \xi_{n\star}^+$ , for  $z < z_0$ , the contour is closed in the lower half-plane and encloses the pole at  $\xi = \xi_{n\star}^-$ . This procedure ensures that the solution decays rather than diverging for  $z \rightarrow \pm\infty$  (or for supersonic tip speeds, corresponds to outward moving waves).

The case  $n=0, k=c$  deserves special attention. For these values of  $n$  and  $k$  the integrand in Eq. (78) has a second-order pole at  $\xi = 0$ . The contribution from this pole is included in the contour which encloses the upper half-plane (corresponding to  $z > z_0$ ) and excluded from the contour enclosing the lower half-plane (corresponding to  $z < z_0$ ). This choice is made on the grounds that there can be no steady perturbation at upstream infinity. The integrated results for  $\varphi_{n\star}$  are

$$\begin{aligned} \Phi_{n\neq}(z) &= - \frac{Q R_{n\neq}(\sigma_0)}{4\pi \beta^2 r_T^2} \frac{e^{\left[ \frac{i n \omega M}{\beta^2 a_\infty} (z - z_0) - \frac{n}{\beta^2 r_T} \sqrt{\beta^2 \left(\frac{K_{n\neq}}{n}\right)^2 - \left(\frac{\omega r_T}{a_\infty}\right)^2} |z - z_0| \right]}}{\frac{n}{\beta^2 r_T} \sqrt{\beta^2 \left(\frac{K_{n\neq}}{n}\right)^2 - \left(\frac{\omega r_T}{a_\infty}\right)^2}} \\ \Phi_{0,0}(z) &= \frac{Q R_{0,0}(\sigma_0)}{2\pi \beta^2 r_T^2} (z - z_0) H(z - z_0) \end{aligned} \quad (80)$$

where  $H(z - z_0)$  is the Heaviside step function and  $R_{0,0} = \sqrt{\frac{z}{1-k^2}}$ .  
 With this result for  $\Phi_{n\neq}$  and the definition of  $\lambda_{n\neq}$  in Eq. (71), Eq. (72) becomes

$$\begin{aligned} \Phi_0(\hat{r}, \hat{r}_0) &= \frac{Q}{2\pi r_T^2 \beta^2} \left( \frac{z}{1-k^2} \right) (z - z_0) H(z - z_0) - \frac{Q}{4\pi \beta^2 r_T^2} \sum_{n=-\infty}^{\infty} \sum_{k=1}^{\infty} \frac{R_{n\neq}(\sigma_0) R_{n\neq}(\sigma)}{\omega \lambda_{n\neq}} \\ &\cdot \exp \left[ i n (\theta - \theta_0) + \frac{i n M^2}{\beta^2} \frac{\omega}{U} (z - z_0) - \frac{\omega \lambda_{n\neq}}{U} |z - z_0| \right] \end{aligned} \quad (81)$$

The first term in the source solution has been omitted in previous treatments.<sup>41,44-46</sup> Except for the presence of this term, the above result can be integrated in the radial direction to recover the line source solution which McCune used to solve the rotor thickness problem. The omission of this term in the mass source (or pressure monopole) solution also affects the fluid doublet (or pressure dipole) solution. The implications that omitting this term from the source and dipole solutions would have to the results for the rotor thickness and loading problems are elaborated upon below where those solutions are presented.

As a result of discovering the omission of this term in previous analyses, several checks were made on the revised source solution. The first test made on the solution for  $\Phi_0$  was to substitute it back into Eq. (68), and to verify that it was indeed the correct solution. In addition, the pressure and velocity fields associated with the mass source solution were obtained from the velocity potential, and it has been verified that the solution displays the properties of a mass source. The flow field quantities required for this

demonstration are the perturbation pressure,  $p_s$ , and the axial and tangential velocity components  $(v_z)_s$  and  $(v_\theta)_s$ . The velocity components are just the appropriate derivatives of the velocity potential. The pressure perturbation can be expressed in terms of  $v_\theta$  and  $v_z$  by using Eqs. (51a) and (53) together with the definition of  $\phi$ .

$$p = -\rho_\infty (U v_z + \omega r v_\theta) \quad (82)$$

The resulting expressions for the flow field variables are

$$(v_\theta)_s = -\frac{Q}{4\pi\beta^2 r_r^2} \sum_{n=-\infty}^{\infty} \sum_{k=1}^{\infty} \frac{R_{n\neq}(\sigma_0) R_{n\neq}(\sigma)}{\omega \lambda_{n\neq}} (in) \cdot \exp \left[ in(\theta - \theta_0) + in \frac{M^2}{\beta^2} \frac{\omega}{U} (z - z_0) - \lambda_{n\neq} \frac{\omega}{U} |z - z_0| \right] \quad (83a)$$

$$(v_z)_s = \frac{Q}{2\pi\beta^2 r_r^2} \left( \frac{z}{1-k^2} \right) H(z - z_0) - \frac{Q}{4\pi\beta^2 r_r^2} \sum_{n=-\infty}^{\infty} \sum_{k=1}^{\infty} \frac{R_{n\neq}(\sigma_0) R_{n\neq}(\sigma)}{\lambda_{n\neq}} \cdot \left[ in \frac{M^2}{\beta^2} - \lambda_{n\neq} \operatorname{sgn}(z - z_0) \right] \exp \left[ in(\theta - \theta_0) + in \frac{M^2}{\beta^2} \frac{\omega}{U} (z - z_0) - \lambda_{n\neq} \frac{\omega}{U} |z - z_0| \right] \quad (83b)$$

$$p_s = -\rho_\infty U \left\{ \frac{Q}{2\pi\beta^2 r_r^2} \left( \frac{z}{1-k^2} \right) H(z - z_0) - \frac{Q}{4\pi\beta^2 r_r^2} \sum_{n=-\infty}^{\infty} \sum_{k=1}^{\infty} \frac{R_{n\neq}(\sigma_0) R_{n\neq}(\sigma)}{\lambda_{n\neq}} \cdot \left[ \frac{in}{\beta^2} - \lambda_{n\neq} \operatorname{sgn}(z - z_0) \right] \exp \left[ in(\theta - \theta_0) + in \frac{M^2}{\beta^2} \frac{\omega}{U} (z - z_0) - \lambda_{n\neq} \frac{\omega}{U} |z - z_0| \right] \right\} \quad (83c)$$

where  $\operatorname{sgn}(z - z_0)$  is +1 for  $z > z_0$  and -1 for  $z < z_0$ .

Now consider a control surface which encloses the point source and is bounded by planes normal to the duct axis at  $z = z_0 \pm \epsilon$  and by the duct walls. Next, the linearized perturbation in the mass flow rate through the surfaces bounded by this control volume is computed. Since the source solution satisfies the boundary conditions of no flow through the duct wall, the only mass flux is through the surfaces normal to the duct axis. Letting  $\dot{m}$



represent the first order terms in the axial component of the mass flux,

$$\dot{m} = \rho_{\infty} v_z + \rho U \quad (84)$$

The density perturbation can be expressed in terms of  $v_{\theta}$  and  $v_z$  using Eqs. (54) and (82). As a result  $\dot{m}$  becomes

$$\dot{m} = \rho_{\infty} \beta^2 v_z - \rho_{\infty} M^2 \left( \frac{\omega r}{U} \right) v_{\theta} \quad (85)$$

If  $\mathcal{M} = \rho_{\infty} Q$  is the rate of introduction of mass by the source then we must have for this control volume

$$\mathcal{M} = \int_{r_n}^{r_r} \int_0^{2\pi} [\dot{m}(\varepsilon) - \dot{m}(-\varepsilon)] r dr d\theta \quad (86)$$

Taking the limit of this expression as  $\varepsilon \rightarrow 0$  and  $z \rightarrow z_0$ , and noting that  $v_{\theta}$  is continuous at  $z_0$ , then

$$\mathcal{M} = \int_{r_n}^{r_r} \int_0^{2\pi} [\rho_{\infty} \beta^2 \Delta v_z] r dr d\theta \quad (87)$$

where

$$\Delta v_z \equiv \lim_{\varepsilon \rightarrow 0} [v_z(z_0 + \varepsilon) - v_z(z_0 - \varepsilon)]$$

From Eq. (83b),

$$\Delta v_z = \frac{Q}{2\pi \beta^2 r_r^2} \left[ \left( \frac{2}{1-k^2} \right) + \sum_{n=-\infty}^{\infty} \sum_{k=1}^{\infty} \varepsilon^{in(\theta-\theta_0)} R_{n,k}(\sigma_0) R_{n,k}(\sigma) \right] \quad (88)$$

Using the series expansions for the delta functions given in Eq. (73), this last equation can be written

$$\Delta v_z = \frac{Q}{\beta^2} \frac{\delta(r-r_0) \delta(\theta-\theta_0)}{r} \quad (89)$$

and hence the mass balance in Eq. (87) is satisfied.

In addition to the demonstration of mass conservation for the above control volume, a similar check has been made for the control volume obtained by withdrawing the surfaces normal to the duct axis to the location  $z = \pm \infty$ . It also has been shown that the results for the flow field of a point source

satisfy the axial component of the linear and angular momentum balances for this latter control volume. These tests on the source solution are given in Appendix C together with comparable tests for the pressure dipole and rotor flow field solutions.

The velocity potential of a fluid doublet can be obtained from that for a source in the conventional way, and the flow field produced by rotor loading could be found by superimposing these doublet solutions. However, as discussed in the previous section, it is more convenient to work with the perturbation pressure in the loading problem. Such an approach is analogous to the acceleration potential method in isolated airfoil theory where the disturbance field of an infinitesimally thin, lifting surface is constructed by the superposition of pressure dipoles.

Since the rotor pressure field satisfies the same equation as the velocity potential, the solution for a pressure monopole is mathematically the same as the solution for a mass source. The corresponding dipole solution is found by differentiating the monopole solution. If the pressure monopole is to be used as the Green's function in the formal solution for the pressure, then the required orientation of the dipoles is normal to the blade surfaces, or in the linearized analysis, to the undisturbed stream direction. For a dipole of strength  $D$  located at the point  $\vec{r}_0$  and oriented in the positive  $\vec{n}_0$  direction shown in Figure 20, the pressure field,  $p_0$ , is given by

$$p_0 = D \frac{\partial G(\vec{r}, \vec{r}_0)}{\partial n_0} \quad (90)$$

where  $G(\vec{r}, \vec{r}_0)$  is the source (or monopole) solution given in Eq. (81) with unit strength. Performing the indicated operations in Eq. (90),

$$p_0 = \frac{D}{4\pi\beta^2 r_r^2 \sqrt{1 + \left(\frac{\omega r_0}{U}\right)^2}} \left\{ 2 \left(\frac{\omega r_0}{U}\right) \left(\frac{z}{1-k^2}\right) H(z-z_0) + \sum_{n=1}^{\infty} \sum_{n^*}^{\infty} \frac{R_{n^*}(\sigma_0) R_{n^*}(\sigma)}{\frac{\omega \lambda_{n^*}}{U}} \right. \\ \cdot \left[ \frac{\ln}{r_0} - \frac{\omega^2 r_0}{U^2} \left(\frac{\ln M^2}{\beta^2}\right) + \frac{\omega^2 r_0}{U^2} \lambda_{n^*} \operatorname{sgn}(z-z_0) \right] \quad (91) \\ \cdot \exp \left[ \ln(\theta - \theta_0) + \frac{\ln M^2}{\beta^2} \frac{\omega}{U} (z-z_0) - \frac{\omega \lambda_{n^*}}{U} |z-z_0| \right] \left. \right\}$$

As with the result for  $\phi_s$ , this solution for  $p_o$  has been substituted into the governing differential equation to verify that it is the correct solution. Forming the quantity  $L p_o$ , where  $L$  is the operator defined by Eq. (58), yields the result

$$L p_o = D \frac{\partial}{\partial n_o} \left[ \frac{\delta(r-r_o) \delta(\theta-\theta_o) \delta(z-z_o)}{r_o} \right] \quad (92)$$

when the series expansions in Eq. (73) are used for the delta functions.

The velocity components associated with the dipole field are obtained by integrating the momentum equations, Eq. (49), along the undisturbed streamlines. Consistent with our generalized function approach in treating singular points, a delta-function body force is included in the momentum equations. Then, the resulting expressions for the velocities are valid everywhere in the duct, including points which lie on the streamline that passes through the dipole location. Otherwise, the expressions would not be valid in a small region enclosing this streamline.

It is convenient to work with the streamwise and normal velocity components, both because fewer integrals have to be evaluated and because the body force term appears only in the normal momentum equation. The dipole exerts a force per unit volume on the fluid,  $\vec{F}_o$ , which is in the negative  $\vec{n}$  direction and expressed by

$$\vec{F}_o = -\vec{n} D \frac{\delta(r-r_o) \delta(\theta-\theta_o) \delta(z-z_o)}{r_o} \quad (93)$$

The streamwise velocity component is simply proportional to the pressure by Eq. (53), which was derived by integrating the streamwise momentum equation. Integrating the radial and normal momentum equations along the undisturbed streamlines yields

$$(U_r)_o = -\frac{1}{\rho_\infty U_R} \int_{-\infty}^s \frac{\partial p_o(s')}{\partial r} ds' \quad (94)$$

$$(U_n)_o = -\frac{1}{\rho_\infty U_R} \int_{-\infty}^s \frac{\partial p_o(s')}{\partial n} ds' + \frac{1}{\rho_\infty U_R} \int_{-\infty}^s F_o(s') ds' \quad (95)$$

The integrations along the undisturbed streamlines can be done by expressing  $ds$  in terms of  $dZ$ . Along these streamlines,  $r$  and the helical variable,  $\zeta$  which is defined by

$$\zeta = \theta - \frac{\omega z}{U} \quad (96)$$

remain constant, and the arc length along the streamlines is

$$ds = \sqrt{1 + \left(\frac{\omega r}{U}\right)^2} dz' \quad (97)$$

Making this change in the integrals, Eqs. (94) and (95) become

$$(v_r)_0 = -\frac{1}{\rho_\infty U} \frac{\partial}{\partial r} \int_{-\infty}^z p_0(r, \theta' = \frac{\omega z'}{U} + \zeta, z') dz' \quad (98)$$

$$(v_n)_0 = -\frac{1}{\rho_\infty U} \frac{\partial}{\partial n} \int_{-\infty}^z p_0(r, \theta' = \frac{\omega z'}{U} + \zeta, z') dz' + \frac{1}{\rho_\infty U} \int_{-\infty}^z F_0(r, \theta' = \frac{\omega z'}{U} + \zeta, z') dz' \quad (99)$$

We need to evaluate two integrals, the streamwise integrals of  $p_0$  and  $F_0$ .

The results are

$$\begin{aligned} \int_{-\infty}^z p_0(r, \theta' = \frac{\omega z'}{U} + \zeta, z') dz' &= \frac{D}{2\pi\beta^2 r^2} \frac{(\omega r_0/U)}{\sqrt{1 + (\frac{\omega r_0}{U})^2}} \left(\frac{\lambda}{1-k}\right) (z-z_0) H(z-z_0) \\ &+ \frac{D}{4\pi\beta^2 r^2 \sqrt{1 + (\frac{\omega r_0}{U})^2}} \sum_{n=-\infty}^{\infty} \sum_{k=1}^{\infty} \frac{R_{nk}(\theta_0) R_{nk}(\theta)}{\left(\frac{\omega \lambda_{nk}}{U}\right)} e^{in(\zeta - \zeta_0)} \\ &\cdot \left[ \frac{\left[1 + \left(\frac{\omega r_0}{U}\right)^2\right]}{\left(\frac{\omega r_0}{U}\right)} \frac{2in\lambda_{nk} H(z-z_0)}{n^2 + \lambda_{nk}^2} + \frac{\left[\frac{in}{r_0} - \frac{\omega^2 r_0}{U^2} \left(\frac{inM^2}{\beta^2}\right) + \frac{\omega^2 r_0}{U^2} \lambda_{nk} \operatorname{sgn}(z-z_0)\right]}{\frac{\omega}{U} \left[\frac{in}{\beta^2} - \lambda_{nk} \operatorname{sgn}(z-z_0)\right]} \right] \\ &\cdot \exp \left[ \frac{in}{\beta^2} \frac{\omega}{U} (z-z_0) - \frac{\omega \lambda_{nk}}{U} |z-z_0| \right] \end{aligned} \quad (100a)$$

$$\begin{aligned} \int_{-\infty}^z F_0(r, \theta' = \frac{\omega z'}{U} + \zeta, z') dz' &= -D \int_{-\infty}^z \frac{\delta(r-r_0) \delta\left(\frac{\omega z'}{U} + \zeta - \theta_0\right) \delta(z'-z_0)}{r_0} dz' \\ &= -D \frac{\delta(r-r_0) \delta(\zeta - \zeta_0)}{r_0} H(z-z_0) \end{aligned} \quad (100b)$$

These expressions can be substituted into those for  $(v_r)_0$  and  $(v_n)_0$  to complete the derivation of the velocity components. Also, the velocity components  $(v_\theta)_0$  and  $(v_z)_0$  are related to  $(v_s)_0$  and  $(v_n)_0$  by

$$v_\theta = v_s \sin \psi + v_n \cos \psi \quad (101a)$$

$$v_z = v_s \cos \psi - v_n \sin \psi \quad (101b)$$

These results for the flow field of a pressure dipole have been shown to satisfy the mass and momentum balances given in Appendix C. The dipole solution possesses the appropriate properties that it does not introduce any mass into the flow, and exerts a force  $D$  on the fluid. In the next two sections, the source and dipole solutions in Eqs. (81) and (91) are used as the Green's functions to construct the flow field produced by a rotor with distributed thickness and loading.

### C. FLOW FIELD OF A NONLIFTING ROTOR (THICKNESS PROBLEM)

#### 1. Solution for the Velocity Potential

In the previous two sections, the foundation has been laid to develop the solution for the thickness contribution to the flow field of a rotor in an annular duct. The source solution given in Eq. (81) can be used as the Green's function,  $G(\vec{r}, \vec{r}_0)$  in the integral representation of the velocity potential in Eq. (66). The solution for a source of unit strength ( $Q = 1$ ) satisfies Eq. (65) and also has the property required by Eq. (67). The integrations in Eq. (66) must be done over the following surfaces: (i) the duct walls, (ii) the surfaces normal to the duct axis at large distance from the rotor, and (iii) the blade surfaces. In describing the integrations over each of these subsurfaces,  $I_1$  and  $I_2$  will refer to the first and second surface integrals in Eq. (66), respectively.

- (i) Along the inner and outer duct walls the boundary condition on  $\varphi(\vec{r}_0)$  is that the normal derivative vanish corresponding to no flow through the walls. Since the Green's function we have found satisfies the same boundary condition,  $I_1$  vanishes for this surface. For the outer wall  $\vec{v}_0 = -\vec{e}_r$  while for the inner wall  $\vec{v}_0 = \vec{e}_r$ . From Eq. (63) we see that  $\vec{v}_0 \cdot \vec{A} = 0$  along both the inner and outer walls, and so  $I_2$  also vanishes at the duct walls.
- (ii) For the surfaces normal to the duct axis at  $z_0 \rightarrow +\infty$  and  $z_0 \rightarrow -\infty$ ,  $\vec{v}_0$  is  $-\vec{e}_z$  and  $+\vec{e}_z$  respectively. Over these two surfaces the sum of the integrals  $I_1$  and  $I_2$  become

$$\begin{aligned}
 I_1 + I_2 = & \left\{ \int_{r_h}^{r_1} \int_0^{2\pi} \left[ - \left( G \frac{\partial \varphi}{\partial z_0} - \varphi \frac{\partial G}{\partial z_0} \right) + MG \left( M \frac{\partial \varphi}{\partial z_0} + \frac{\omega}{a_\infty} \frac{\partial \varphi}{\partial \theta_0} \right) \right. \right. \\
 & \left. \left. - M \varphi \left( M \frac{\partial G}{\partial z_0} + \frac{\omega}{a_\infty} \frac{\partial G}{\partial \theta_0} \right) \right] \right|_{z_0 \rightarrow +\infty} r_0 d\theta_0 dr_0 \\
 & + \int_{r_h}^{r_1} \int_0^{2\pi} \left[ \left( G \frac{\partial \varphi}{\partial z_0} - \varphi \frac{\partial G}{\partial z_0} \right) - MG \left( M \frac{\partial \varphi}{\partial z_0} + \frac{\omega}{a_\infty} \frac{\partial \varphi}{\partial \theta_0} \right) \right. \\
 & \left. \left. + M \varphi \left( M \frac{\partial G}{\partial z_0} + \frac{\omega}{a_\infty} \frac{\partial G}{\partial \theta_0} \right) \right] \right|_{z_0 \rightarrow -\infty} r_0 dr_0 d\theta_0 \left. \right\} \quad (102)
 \end{aligned}$$

Consider the integrand at  $z_0 \rightarrow +\infty$  first. In this case  $z < z_0$  and so the first term ( $n=0, k=0$ ) in  $G(\vec{r}, \vec{r}_0)$  is zero. The remaining terms in  $G(\vec{r}, \vec{r}_0)$  decay exponentially. The same behavior holds for  $\frac{\partial G}{\partial \theta_0}$  and  $\frac{\partial G}{\partial z_0}$ . Since  $\varphi(\vec{r}_0)$  and its derivatives must be bounded, the integrand vanishes as  $z_0 \rightarrow +\infty$ . Next, consider the integrand evaluated at  $z_0 \rightarrow -\infty$ . Here  $z > z_0$  and the  $n=0, k=0$  term contributes to both  $G$  and  $\frac{\partial G}{\partial z_0}$ ; the remaining terms in  $G$ ,  $\frac{\partial G}{\partial \theta_0}$ , and  $\frac{\partial G}{\partial z_0}$  decay exponentially. For subsonic flow,  $\varphi$  and the velocity components obtained from its derivatives are required to vanish far upstream of

the blade row. Note that  $G$  diverges linearly as  $Z_0 \rightarrow \infty$  and so the velocity field must fall off faster than this in order for the integrand to vanish. We shall see that the velocity field decays exponentially upstream of the rotor. Hence, the integrands vanish for  $Z_0 \rightarrow -\infty$  also, and the integrals  $I_1$  and  $I_2$  make no contribution along the surfaces normal to the duct axis. For supersonic tip speeds, acoustic waves propagate away from the blade row and these surface integrals should be re-examined.

- (iii) In the linearized analysis, the blade row is assumed to make only a slight perturbation of the free-stream flow. Consistent with this assumption, the blade surface boundary conditions are applied along the undisturbed stream direction. In this approximation, the normals to the upper and lower blade surfaces are, respectively,

$$\vec{n}_0 = \pm \vec{n} = \pm (\cos \psi_0 \vec{e}_\theta - \sin \psi_0 \vec{e}_z) \quad (103)$$

where  $\psi_0 = \tan^{-1}(\omega r_0 / U)$ . From Eqs. (63) and (103) it can be seen that  $\vec{v}_0 \cdot \vec{n}$  vanishes and thus, in the linearized approximation,  $I_2$  contains no contribution from the blade surfaces.

The separation of the rotor flow field into the thickness and loading contributions is made by prescribing that there be no pressure difference across the blade surfaces in the thickness case, or that the blades are locally unloaded. If the pressure is continuous across the blade surface, then  $v_z$  and  $\phi$  are also. Hence, because of the opposite signs of  $\frac{\partial G}{\partial n_0}$  on the upper and lower surfaces, only the part of the integrand in  $I_1$  containing  $G \frac{\partial \phi}{\partial n_0}$  contributes to the integration over the blade surfaces.

Except for this contribution from integrating  $I_1$  over the blade surfaces, all the surface integrals in Eq. (66) vanish. Thus, the expression for  $\phi$  has been reduced to

$$\phi(\vec{r}) = \int_{S_B} G(\vec{r}, \vec{r}_0) \Delta \left( \frac{\partial \phi}{\partial n_0} \right) dS_0 \quad (104)$$

where  $S_b$  denotes the surface area of the rotor blades projected on the undisturbed stream surface, and  $\Delta \left( \frac{\partial \phi}{\partial n_i} \right)$  represents the difference in normal velocity across each blade surface. This expression is the same as the familiar result in isolated airfoil theory that the effects of wing thickness can be represented by the superposition of sources whose strength is equal to the discontinuity in  $v_n$  at each point.

The linearized form of the blade boundary conditions is

$$v_n^u = U_R \frac{\partial \eta_u}{\partial S} \quad v_n^l = U_R \frac{\partial \eta_l}{\partial S} \quad (105)$$

where  $\eta_u$  and  $\eta_l$  are the distances to the upper and lower surfaces, measured normal to the undisturbed stream direction,  $S$ . The quantities  $\eta_u$  and  $\eta_l$  can be expressed in terms of a blade thickness and a blade incidence plus camber line in the conventional way as illustrated in Figure 21. However, for a rotor the blade thickness and camber are not independent because, as noted earlier, in order for the blades to be unloaded, they must be cambered to account for loadings which would otherwise be induced by blade interference effects. If  $t(s, r)$  represents  $\eta_u(s, r) - \eta_l(s, r)$  then,

$$\begin{aligned} \eta_u(s, r) &= \eta_c(s, r) + \frac{1}{2} t(s, r) \\ \eta_l(s, r) &= \eta_c(s, r) - \frac{1}{2} t(s, r) \end{aligned} \quad (106)$$

where  $\eta_c(s, r)$  is the camber line, which consists of two parts, a thickness part,  $\eta_{ct}$  and a loading part,  $\eta_{cl}$ . From Eqs. (105) and (106), the discontinuity in the normal velocity across the blade surface is then related to the thickness distribution by

$$\Delta v_n = U_R \frac{\partial t}{\partial S} \quad (107)$$

For a rotor with  $B$  equally spaced blades, the blades lie on the surfaces  $\xi = 2j\pi/B$ ,  $j = 0, 1, \dots, B-1$  where  $\xi$  is the helical variable defined



by Eq (96). It is convenient to do the integration over these surfaces by projecting them on the  $r_0, z_0$  plane so that

$$dS_B = \sqrt{1 + \left(\frac{\omega r_0}{U}\right)^2} dr_0 dz_0 \quad (108)$$

With the blade leading edges located at  $z_0 = 0$ , the velocity potential is

$$\begin{aligned} \phi(r, \theta, z) = & \sum_{j=0}^{B-1} \int_{r_h}^{r_r} \int_0^{c(z)} \Delta v_n(r_0, z_0) G(r, \zeta, z; r_0, \zeta_0 = \frac{2j\pi}{B}, z_0) \\ & \cdot \sqrt{1 + \left(\frac{\omega r_0}{U}\right)^2} dz_0 dr_0 \end{aligned} \quad (109)$$

While not crucial to the ensuing analysis, it is convenient to assume that the axial projection of the blade chord is a constant,  $c_a$ , and that the radial and axial variations of  $\Delta v_n$  (and  $\tau$ ) are factorable so that

$$f(r_0) g(z_0) = \sqrt{1 + \left(\frac{\omega r_0}{U}\right)^2} \Delta v_n = \sqrt{1 + \left(\frac{\omega r_0}{U}\right)^2} U \frac{\partial \tau}{\partial S} \quad (110)$$

With these assumptions, the expression for the velocity potential becomes

$$\begin{aligned} \phi(r, \zeta, z) = & \sum_{j=0}^{B-1} \int_{r_h}^{r_r} \int_0^{c_a} \left\{ \frac{1}{2\pi\beta^2 r_r^2} \left(\frac{\lambda}{1-k^2}\right) (z-z_0) H(z-z_0) - \frac{1}{4\pi\beta^2 r_r^2} \right. \\ & \cdot \sum_{n=0}^{\infty} \sum_{k=1}^{\infty} \frac{R_{n,k}(z_0) R_{n,k}(r)}{\frac{\omega \lambda_{n,k}}{U}} \exp \left[ i n \left( \zeta - \frac{2j\pi}{B} \right) + \frac{i n}{\beta^2} \frac{\omega}{U} (z-z_0) \right. \\ & \left. \left. - \frac{\omega \lambda_{n,k}}{U} |z-z_0| \right] \right\} f(r_0) g(z_0) dz_0 dr_0 \end{aligned} \quad (111)$$

The summation over the number of blades can be done by using the identity

$$\sum_{j=0}^{B-1} e^{-in \left(\frac{2j\pi}{B}\right)} = \begin{cases} 0 & n \neq mB \\ B & n = mB \end{cases} \quad (112)$$

where  $m$  is an integer. The result for the velocity potential becomes

$$\begin{aligned}
\varphi(r, \xi, z) = & \frac{B}{2\pi\beta^2 r_T^2} \int_{r_n}^{r_T} \int_0^{z_n} \left\{ \left( \frac{z}{1-k} \right) (z-z_0) H(z-z_0) \right. \\
& - \frac{1}{2} \sum_{m=-\infty}^{\infty} \sum_{k=1}^{\infty} \frac{R_{mBk}(\sigma_0) R_{mBk}(\sigma)}{\frac{\omega \lambda_{mBk}}{U}} \exp [imB\xi + \Lambda_{mBk}(z, z_0)(z-z_0)] \Big\} \\
& \cdot f(r_0) g(z_0) dz_0 dr_0
\end{aligned} \tag{113}$$

where we have introduced the notation

$$\Lambda_{mBk}(z, z_0) = \frac{\omega}{U} \left[ \frac{imB}{\beta^2} - \lambda_{mBk} \operatorname{sgn}(z-z_0) \right] \tag{114}$$

## 2. Expressions for the Velocity Components and Pressure Perturbation

Having this solution for the velocity potential, the other flow field variables can be found by taking the appropriate derivatives. The results for the velocity components are given in terms of  $v_s$ ,  $v_n$ , and  $v_r$ , which are related to  $\varphi$  by

$$v_s = \frac{\partial \varphi}{\partial \xi} = \frac{1}{\sqrt{1+(\omega r/U)^2}} \left. \frac{\partial \varphi}{\partial z} \right)_{r, \xi} \tag{115a}$$

$$v_n = \frac{\partial \varphi}{\partial n} = \frac{\sqrt{1+(\omega r/U)^2}}{r} \left. \frac{\partial \varphi}{\partial \xi} \right)_{r, z} - \frac{\omega r}{U} v_s \tag{115b}$$

$$v_r = \frac{\partial \varphi}{\partial r} \tag{115c}$$

The pressure is simply proportional to  $v_s$  by Eq. (53). The resulting expressions for the velocity components are

$$\begin{aligned}
v_s = & \frac{B}{2\pi\beta^2 r_T^2 \sqrt{1+(\omega r/U)^2}} \int_{r_n}^{r_T} \int_0^{z_n} \left\{ \left( \frac{z}{1-k} \right) H(z-z_0) - \frac{1}{2} \sum_{m=-\infty}^{\infty} \sum_{k=1}^{\infty} \frac{R_{mBk}(\sigma) R_{mBk}(\sigma_0)}{\frac{\omega}{U} \lambda_{mBk}} \right. \\
& \cdot \Lambda_{mBk}(z, z_0) \exp [imB\xi + \Lambda_{mBk}(z, z_0)(z-z_0)] \Big\} f(r_0) g(z_0) dz_0 dr_0
\end{aligned} \tag{116a}$$

$$v_n = \frac{B}{2\pi\beta^2 r_T^2 \sqrt{1 + \left(\frac{\omega r}{U}\right)^2}} \int_{r_H}^{r_1} \int_0^{c_a} \left\{ -\left(\frac{z}{r}\right) \left(\frac{\omega r}{U}\right) H(z-z_0) - \frac{1}{2} \sum_{m=-\infty}^{\infty} \sum_{k=1}^{\infty} \frac{R_{mBk}(\sigma) R_{mBk}(\sigma_0)}{\frac{\omega}{U} \lambda_{mBk}} \right. \\ \left. \cdot V_{mBk}(r, z, z_0) \exp [imB\zeta + \Lambda_{mBk}(z, z_0)(z-z_0)] \right\} f(r_0) g(z_0) dr_0 dz_0 \quad (116b)$$

$$v_r = -\frac{B}{4\pi\beta^2 r_T^2} \int_{r_H}^{r_1} \int_0^{c_a} \left\{ \sum_{m=-\infty}^{\infty} \sum_{k=1}^{\infty} \frac{R'_{mBk}(\sigma) R_{mBk}(\sigma_0)}{\frac{\omega}{U} \lambda_{mBk}} \left(\frac{\kappa_{mBk}}{r_T}\right) \right. \\ \left. \cdot \exp [imB\zeta + \Lambda_{mBk}(z, z_0)(z-z_0)] \right\} f(r_0) g(z_0) dz_0 dr_0 \quad (116c)$$

where the prime on  $\kappa_{mBk}$  denotes differentiation with respect to the argument and

$$V_{mBk}(r, z, z_0) = \frac{imB}{r} - \frac{\omega^2 r}{U^2} \left[ imB \frac{M^2}{\beta^2} - \lambda_{mBk} \operatorname{sgn}(z-z_0) \right] \quad (117)$$

also has been introduced.

These results for the flow field of a nonlifting rotor are shown to satisfy the mass and momentum balances in Appendix C. For subsonic flow, there should be no net force or work done by the rotor. The derivations presented in the appendix have verified that this is so. Another check which has been made on these expressions is that they display the correct behavior at the blade surfaces

### 3. Behavior of the Velocity Components at the Blade Surfaces

The expressions given for the disturbance velocity field contain doubly infinite series expansions in the duct eigenfunctions. In order to demonstrate that the velocity components display the correct behavior at the blade surfaces, the convergence properties of these series need to be considered. Terms in the  $m$  summations which are of order  $(mB)^{-1}$  are expected to lead to divergent series, or series which do not converge uniformly. The manipulations performed below are aimed at identifying those terms which are  $O(mB)^{-1}$  and hence are potentially divergent. Furthermore, within the group of terms, we wish to isolate a series for which the  $k$  summation can be

done analytically and for which the  $m$  summation does not converge uniformly for all values of the  $\zeta$  coordinate. It can be anticipated that such a series produces the discontinuities in the surface quantities which occur as changes in  $\zeta$  are made which correspond to crossing a blade surface. For the remainder of this section our attention is confined to points within the blade row, i.e., for  $0 \leq z \leq C_a$ .

First we wish to show that  $v_s$  is continuous across the blade surfaces. This demonstration also provides a check on the assumption that the blades are locally unloaded by virtue of the relationship between  $p$  and  $v_s$ .

The first step in examining the value of  $v_s$  at the blade surfaces is to carry out an integration by parts in the integral over  $z_0$ . After the first integration by parts the expression for  $v_s$  is

$$\begin{aligned}
 v_s = & \frac{B}{2\pi\beta^2 r_T^2 \sqrt{1 + \left(\frac{\omega r}{U}\right)^2}} \int_{r_h}^{r_T} \left\{ \frac{2}{1-k^2} \int_0^{C_a} g(z_0) H(z-z_0) dz_0 - \frac{1}{2} \sum_{m=1}^{\infty} \sum_{k=1}^{\infty} \frac{R_{mBk}(\sigma) R_{mBk}(\sigma_0)}{\frac{\omega^2 m B k}{U}} \right. \\
 & - e^{imB\zeta} \left[ g(0) e^{\Lambda_{mBk}(z,0)z} - g(C_a) e^{\Lambda_{mBk}(z,C_a)(z-C_a)} \right. \\
 & \left. \left. + \int_0^{C_a} e^{\Lambda_{mBk}(z,z_0)(z-z_0)} \frac{dg}{dz_0} dz_0 \right] \right\} f(r_0) dr_0
 \end{aligned} \tag{118}$$

Were it not for the  $k$ -dependence of the factors other than  $R_{mBk}$ , the  $k$ -summations in this expression would be just the Fourier-Bessel series expansion of the form (see Appendix A)

$$f(r) = \sum_{k=1}^{\infty} R_{mBk}(\sigma) \int_{r_h}^r f(r_0) R_{mBk}(\sigma_0) \sigma_0 d\sigma_0$$

Since  $f(r)$  must be independent of the order of the Bessel functions in this expansion, the product  $R_{mBk}(\sigma) R_{mBk}(\sigma_0)$  need not be considered in determining the  $m$ -dependence of each term in the double series. The coefficients in the series containing  $q(0)$  and  $q(c_a)$  are inversely proportional to  $\lambda_{mBk}$  which is  $O(mB)$ , but the exponential factors in these terms prevent the series from diverging, except as the leading or trailing edge is approached. There, unless the slope of the thickness profile vanishes, the series diverge. The divergence of these series produces the singularities in the pressure which typically occur at the leading and trailing edges of subsonic airfoils. The divergence of the surface pressure at these points is evident in the original results of McCune,<sup>41</sup> as well as in the surface pressure results accompanying the thickness-induced camber lines presented in Reference 46.

Each integration by parts over  $Z_0$  introduces another factor of  $(mB)^{-1}$  in each term of the double series. A second integration by parts in the  $v_s$  expression produces the following results.

$$\begin{aligned}
 v_s = & \frac{B}{2\pi\beta^2 r^2 \sqrt{1 + \left(\frac{\omega r}{U}\right)^2}} \int_{r_u}^{r_r} \left\{ \frac{2}{1-k^2} \int_0^{c_a} q(Z_0) H(Z-Z_0) dZ_0 - \frac{1}{2} \sum_{m=-\infty}^{\infty} \sum_{k=1}^{\infty} \frac{R_{mBk}(\sigma) R_{mBk}(\sigma_0)}{\frac{\omega}{U} \lambda_{mBk}} \right. \\
 & \cdot e^{imBk} \left[ q(0) e^{\lambda_{mBk}(Z,0)Z} - q(c_a) e^{\lambda_{mBk}(Z,c_a)(Z-c_a)} \right. \\
 & + \frac{q'(0)}{\lambda_{mBk}(Z,0)} e^{\lambda_{mBk}(Z,0)Z} - \frac{q'(c_a)}{\lambda_{mBk}(Z,c_a)} e^{\lambda_{mBk}(Z,c_a)(Z-c_a)} \\
 & \left. \left. + 2 \frac{q'(Z) \frac{\omega \lambda_{mBk}}{U}}{\left(\frac{\omega}{U}\right)^2 \left(\frac{mB}{\beta}\right)^2 + \lambda_{mBk}^2} + \int_0^{c_a} \frac{e^{\lambda_{mBk}(Z,Z_0)(Z-Z_0)}}{\lambda_{mBk}} \frac{d^2 q}{dZ_0^2} dZ_0 \right] \right\} f(r_0) dr_0
 \end{aligned}
 \tag{119}$$

The second integration by parts yields integrated terms which are proportional to  $q'(z_0)$ , evaluated at  $z_0 = 0, z$ , and  $C_2$ . These terms are  $O(mB)^{-2}$  and so the corresponding series are uniformly convergent. Hence, away from the leading and trailing edges, all the series in  $v_s$  are uniformly convergent for all values of  $\zeta$ , including those at the blade surfaces. It can therefore be concluded that  $v_s$  and  $p$  are continuous across these surfaces. The same is not true of  $v_n$ , however, which must be discontinuous at  $\zeta = \frac{2j\pi}{\rho}$  by an amount dictated by the boundary condition, Eq. (107).

We have already evaluated the  $v_s$  contribution to the expression given for  $v_n$  in Eq. (115b), and shown it to be continuous. Any discontinuity in  $v_n$  must then come from the  $\frac{\partial q}{\partial \zeta}$  contribution. After performing a single integration by parts on the  $z_0$  integral, the expression for  $\frac{\partial q}{\partial \zeta}$  becomes

$$\begin{aligned} \left. \frac{\partial q}{\partial \zeta} \right)_{r, z} = & -\frac{B}{4\pi\beta^2 r_T^2} \int_{r_H}^{r_T} \left\{ \sum_{m=-\infty}^{\infty} \sum_{k=1}^{\infty} R_{mBk}(\sigma) R_{mBk}(\sigma_0) e^{imB\zeta} \right. \\ & \cdot (imB) \left[ \frac{2q(z)}{\left(\frac{\omega}{U}\right)^2 \left(\frac{mB}{\beta^2} + \lambda_{mBk}^2\right)} + \frac{q(0)}{\omega\lambda_{mBk}} \frac{e^{-\lambda_{mBk}(z,0)z}}{\lambda_{mBk}(z,0)} \right. \\ & \left. \left. - \frac{q(C_2)}{\omega\lambda_{mBk}} \frac{e^{-\lambda_{mBk}(z,C_2)(z-C_2)}}{\lambda_{mBk}(z,C_2)} + \frac{1}{\omega\lambda_{mBk}} \int_0^{C_2} \frac{e^{-\lambda_{mBk}(z,z_0)}}{\lambda_{mBk}(z,z_0)} \frac{dq}{dz_0} dz_0 \right] \right\} f(r_0) dr_0 \end{aligned} \quad (120)$$

where the prime on the summation indicates the  $m=0$  term is excluded. The leading and trailing-edge terms behave as discussed above, while the remaining integral is  $O(mB)^{-2}$  as in the  $v_s$  expression. However, the first of the integrated terms is  $O(mB)^{-1}$  and does not contain the exponential factors which appear in the leading and trailing edge terms. This term, which may diverge, or at best not converge uniformly, will be found to produce a discontinuity in  $v_n$ .

Next we consider the behavior of the first term in  $\frac{\partial \varphi}{\partial \xi}$ , by defining the double series  $S(r, \xi)$  to which this term is proportional.

$$S(r, \xi) = \frac{B}{\pi} \frac{1}{\left(\frac{\omega r_T}{U}\right)^2} \int_{r_H}^{r_T} \sum_{m=1}^{\infty} \sum_{k=1}^{\infty} R_{mBk}(\sigma) R_{mBk}(\sigma_0) \frac{\sin(mB\xi)}{mB} \cdot \left[ \frac{1}{\beta^2 + \beta^2 \left(\frac{\lambda_{mBk}}{mB}\right)^2} \right] f(r_0) d r_0 \quad (121)$$

Substituting Eq. (71) for  $\lambda_{mBk}$  in the bracketed factor yields

$$\frac{1}{\beta^2 + \beta^2 \left(\frac{\lambda_{mBk}}{mB}\right)^2} = \frac{\left(\frac{\omega r_T}{U}\right)^2}{\left(\frac{K_{mBk}}{mB}\right)^2 + \left(\frac{\omega r_T}{U}\right)^2} \quad (122)$$

If the quantity  $(\omega r_0 / U)^2 / [1 + (\omega r_0 / U)^2]$  is added and subtracted to this term in brackets, and the  $r_0$  integration is done term by term, the function  $S(r, \xi)$  becomes

$$S(r, \xi) = \frac{B}{\pi} \sum_{m=1}^{\infty} \frac{\sin(mB\xi)}{mB} \sum_{k=1}^{\infty} R_{mBk}(\sigma) \int_{r_H}^{r_T} R_{mBk}(\sigma_0) \left[ \frac{r_0 f(r_0)}{1 + \left(\frac{\omega r_0}{U}\right)^2} \right] \sigma d \sigma_0 + \frac{B}{\pi} \sum_{m=1}^{\infty} \sum_{k=1}^{\infty} R_{mBk}(\sigma) \frac{\sin(mB\xi)}{mB} \frac{1}{\left[\left(\frac{K_{mBk}}{mB}\right)^2 + \left(\frac{\omega r_T}{U}\right)^2\right]} \int_{r_H}^{r_T} \frac{1}{r_T^2} \left[ r_T^2 - r_0^2 \left(\frac{K_{mBk}}{mB}\right)^2 \right] R_{mBk}(\sigma_0) f(r_0) d r_0 \quad (123)$$

The  $k$  summation in the first line of Eq. (123) is just the Fourier-Bessel expansion for the bracketed function in terms of the radial eigenfunctions. Performing this summation and using the equation satisfied by the radial eigenfunctions, Eq. (74), to substitute in the second integral,  $S(r, \xi)$  can be written

$$S(r, \zeta) = \frac{r f(r)}{1 + \left(\frac{\omega r}{U}\right)^2} \frac{B}{\pi} \sum_{m=1}^{\infty} \frac{\sin(mB\zeta)}{mB} + \frac{B}{\pi} \sum_{m=1}^{\infty} \sum_{k=1}^{\infty} R_{mBk}(r) \frac{\sin(mB\zeta)}{(mB)^2} \\ \cdot \frac{1}{\left[\left(\frac{K_{mBk}}{mB}\right)^2 + \left(\frac{\omega r}{U}\right)^2\right]} \int_{r_H}^{r_r} \frac{d}{dr_0} \left( r_0 \frac{dR_{mBk}}{dr_0} \right) \frac{f(r_0) r_0}{1 + \left(\frac{\omega r_0}{U}\right)^2} dr_0 \quad (123)$$

Now, the eigenvalues  $K_{mBk}$  are all greater than  $mB$ , being  $O(mB)$  for large  $mB$ , and the remaining integral can be integrated by parts.

$$\int_{r_H}^{r_r} \frac{d}{dr_0} \left( r_0 \frac{dR_{mBk}}{dr_0} \right) \frac{f(r_0) r_0}{1 + \left(\frac{\omega r_0}{U}\right)^2} dr_0 = \frac{f(r_0) r_0^2}{1 + \left(\frac{\omega r_0}{U}\right)^2} \frac{dR_{mBk}}{dr_0} \Big|_{r_H}^{r_r} \\ - \int_{r_H}^{r_r} \frac{dR_{mBk}}{dr_0} r_0 \frac{d}{dr_0} \left[ \frac{f(r_0) r_0}{1 + \left(\frac{\omega r_0}{U}\right)^2} \right] dr_0 \quad (125)$$

The integrated term vanishes because each radial eigenfunction identically satisfies the boundary conditions at the duct walls. Another integration by parts could be done but it does not appear worthwhile. The important point to make is that each  $m, k$  term of the double series in Eq. (124) is at most of order  $(mB)^{-2}$ . Here again this series is then a regular series, and the first series in Eq. (124) is the only remaining contribution to  $S(r, \zeta)$  which could contain a discontinuity. The single summation on the right-hand side of Eq. (124) is proportional to the Fourier series expansion of the generalized function,  $\zeta_j$ , which is defined by

$$\zeta_j = \zeta - \frac{(2j+1)\pi}{B} \quad \frac{2\pi j}{B} \leq \zeta \leq \frac{2\pi(j+1)}{B} \quad j = 0, 1, \dots, B-1 \quad (126)$$

This function, illustrated in Figure 22 was first used by Reissner<sup>52</sup> in his representation of a propeller wake. It can be shown that the Fourier series representation of  $\zeta_j$  is



$$\zeta_j = -2 \sum_{m=1}^{\infty} \frac{\sin(mB\zeta)}{mB} \quad (127)$$

With these results, the expression for  $S(r, \zeta)$  becomes

$$S(r, \zeta) = -\left(\frac{B}{2\pi}\right) \zeta_j \frac{r f(r)}{1 + \left(\frac{\omega r}{U}\right)^2} - \frac{B}{\pi} \sum_{m=1}^{\infty} \sum_{k=1}^{\infty} R_{mk}(\sigma) \frac{\sin(mB\zeta)}{(mB)^3} \quad (128)$$

$$\cdot \left[ \frac{1}{\left[ \left(\frac{k}{mB}\right)^2 + \left(\frac{\omega r}{U}\right)^2 \right]} \int_{r_0}^{r_1} r_0 \frac{dR_{mk}}{dr_0} \frac{d}{dr_0} \left[ \frac{f(r_0) r_0}{1 + \left(\frac{\omega r_0}{U}\right)^2} \right] dr_0 \right]$$

As can be seen from Figure 22, the generalized function  $\zeta_j$  has a jump of  $(-\frac{2\pi}{B})$  as  $\zeta$  crosses a blade location moving in the direction of increasing  $\zeta$ . The contribution to  $\frac{\partial q}{\partial z} \Big|_{r, \zeta}$  from the term containing  $S(r, \zeta)$  is simply  $g(z) S(r, \zeta)$ . Combining this result with Eq. (115b) to find the corresponding term in  $v_n$  and then forming the difference  $v_n(r, z, \zeta = \frac{2\pi j^+}{B}) - v_n(r, z, \zeta = \frac{2\pi j^-}{B})$ , the contribution of that term is

$$v_n \left( r, z, \zeta = \frac{2\pi j^+}{B} \right) - v_n \left( r, z, \zeta = \frac{2\pi j^-}{B} \right) = \frac{f(r) g(z)}{\sqrt{1 + \left(\frac{\omega r}{U}\right)^2}} \quad (129)$$

and the definition of the functions  $f$  and  $g$  in terms of  $\Delta v_n$  given in Eq. (110) is retrieved. Since the other contributions to  $v_n$  are continuous for all values of  $\zeta$ , and for values of  $z$  away from the leading and trailing edges, we have succeeded in showing analytically that our result for the velocity field does in fact contain the correct jump in normal velocity across the blade surfaces.

If the results for  $v_s$  and  $\frac{\partial q}{\partial z}$  are collected to find the whole expression for  $v_n$  according to Eq. (115b), the answer is

$$\begin{aligned}
v_n = & -\frac{B}{2\pi} \zeta_j \Delta v_n(r, z) - \frac{B}{\pi} q(z) \frac{\sqrt{1 + \left(\frac{\omega r}{U}\right)^2}}{r} \sum_{m=1}^{\infty} \sum_{k=1}^{\infty} \frac{R_{mBk}(\sigma)}{\left[\left(\frac{K_{mBk}}{mB}\right)^2 + \left(\frac{\omega r}{U}\right)^2\right]} \\
& \cdot \frac{\sin(mBz)}{(mB)^2} \int_{r_H}^{r_T} \frac{dR_{mBk}}{dr_0} \frac{d}{dr_0} \left[ \frac{r_0 f(r_0)}{1 + \left(\frac{\omega r_0}{U}\right)^2} \right] dr_0 - \frac{B}{2\pi \beta^2 r_T^2} \frac{\left(\frac{\omega r}{U}\right)}{\sqrt{1 + \left(\frac{\omega r}{U}\right)^2}} \left(\frac{2}{1-k^2}\right) \\
& \cdot \int_{r_H}^{r_T} \int_0^{c_a} f(r_0) q(z_0) H(z-z_0) dz_0 dr_0 + \frac{B}{4\pi \beta^2 r_T^2 \sqrt{1 + \left(\frac{\omega r}{U}\right)^2}} \quad (130) \\
& \cdot \int_{r_H}^{r_T} \sum_{m=-\infty}^{\infty} \sum_{k=1}^{\infty} \frac{R_{mBk}(\sigma) R_{mBk}(\sigma)}{\frac{\omega}{U} \lambda_{mBk} \left[ \left(\frac{mB}{\beta^2}\right)^2 + \lambda_{mBk}^2 \right]} e^{imBz} \left\{ q(0) T_{mBk}(r, z, 0) e^{\lambda_{mBk}(z, 0)z} \right. \\
& - q(c_a) T_{mBk}(r, z, c_a) e^{\lambda_{mBk}(z, c_a)(z-c_a)} + \int_0^{c_a} e^{\lambda_{mBk}(z, z_0)(z-z_0)} \\
& \left. \cdot T_{mBk}(r, z, z_0) \frac{dq}{dz_0} dz_0 \right\} f(r_0) dr_0
\end{aligned}$$

where

$$\begin{aligned}
T_{mBk}(r, z, z_0) = & -\frac{1}{\frac{\omega r}{U}} \left[ \frac{(mB)^2}{\beta^2} - imB \lambda_{mBk} \operatorname{sgn}(z-z_0) \right] \\
& + \frac{\omega r}{U} \left[ \frac{M^2(mB)^2}{\beta^4} + imB \lambda_{mBk} \operatorname{sgn}(z-z_0) + \lambda_{mBk}^2 \right] \quad (131)
\end{aligned}$$

The first term in  $v_n$  contains only the symmetric discontinuity and hence makes no contribution to the continuous part of  $v_n$  at the blade surfaces. When evaluated at a blade surface the second term in  $v_n$  vanishes and the remaining terms represent the continuous part of  $v_n$ , or the thickness-induced camber lines. The third term in the above expression, and the first term in Eq. (119), come from the  $n=0, k=r$  term omitted from previous treatments of the thickness problem. The camber line calculations of Ref. 46 and the surface

pressure calculations of Reference 41 should be corrected for the presence of these terms. Since  $U_R \frac{\partial c(r, s)}{\partial s}$ , which may be written as  $U \frac{\partial c(r, z)}{\partial z}$ , is proportional to  $q(z)$ , these contributions to both  $v_n$  and  $p$  are proportional to the chordwise variation in the local thickness distribution. Furthermore, these terms make no contribution to the disturbance field upstream or downstream of the blade row, and therefore, the acoustic calculations of References 44 and 45 are unaffected by their inclusion.

The above manipulations of the expressions for the perturbation velocities apply for points within the confines of the rotor row, i.e., for  $0 \leq z \leq c_d$ . If the integrations by parts are done for field points upstream and downstream of the blade row the singularities encountered at the leading and trailing edges remain but the velocities everywhere else in the flow are found to be continuous.

The final expressions presented for  $v_s$  and  $v_n$  in Eqs. (119) and (130) have been shown to have the correct behavior at the blade surfaces. Moreover, in the course of demonstrating this, these results have been put in a form which should facilitate the computation of the surface pressure and the thickness-induced camber lines for nonlifting rotor blades.

#### D. FLOW FIELD OF A LIFTING ROTOR (LOADING PROBLEM)

##### 1. Solution for the Perturbation Pressure

The determination of the pressure field produced by a lifting rotor closely parallels the solution procedure for the velocity potential in the thickness problem. The Green's function is the same, though now its interpretation is in terms of a pressure monopole. The formal solution for  $p$  is identical to that given in Eq. (66) for  $\phi$ , except for the replacement of  $\phi$  with  $p$ . In addition, both of the integrations over the duct walls and the surfaces at  $r_0 = r_\infty$  vanish as before, as does the integration of  $\vec{v} \cdot (\vec{A} \vec{\phi})$  over the blade

surfaces. The remaining integral over the blade surfaces distinguishes the lifting case from the thickness case. Here the magnitude of  $\frac{\partial \psi}{\partial n_0}$  is the same on both sides of the blades because  $v_n$  must be continuous. Since the normals to the upper and lower surfaces lie in opposite directions and  $G(\vec{r}, \vec{r}_0)$  is continuous across the blades, the integral of  $G \frac{\partial \psi}{\partial n_0}$  over the blade surfaces vanishes. Thus the integral representation of the solution for the pressure field reduces to

$$p(\vec{r}) = \int_{S_0} \Delta p(\vec{r}_0) \frac{\partial G}{\partial n_0} dS_0 \quad (132)$$

where  $S_0$  is the projection of the blade surface on the undisturbed stream direction and

$$\Delta p \equiv p\left(r_0, z_0, \zeta_0 = \frac{2\pi j^-}{B}\right) - p\left(r_0, z_0, \zeta_0 = \frac{2\pi j^+}{B}\right) \quad (133)$$

The sign of the integrand in Eq. (132) has been reversed from that in Eq. (66) so that  $\Delta p$  is defined as a positive number.

If we substitute the pressure dipole solution (Eq. (91)) with unit strength for  $\frac{\partial G}{\partial n_0}$  and, exactly as was done for  $\psi$  in the thickness problem, carry out the summation over the number of blades, we get the following result for the pressure field of the rotor:

$$\begin{aligned} p = & \frac{\omega B}{2\pi\beta^2 U} \int_0^{c_h} \Delta p(z_0) H(z-z_0) dz_0 \\ & + \frac{B}{4\pi\beta^2 r^2} \int_{r_h}^{r_t} \int_0^{c_h} \sum_{m=-\infty}^{\infty} \sum_{k=1}^{\infty} \frac{R_{m\theta k}(\sigma) R_{m\theta k}(\sigma_0)}{\omega \lambda_{m\theta k} U} \\ & \cdot \exp\left[imB\zeta + \lambda_{m\theta k}(z, z_0)(z-z_0)\right] V_{m\theta k}(r_0, z, z_0) \Delta p(r_0, z_0) dz_0 d\sigma_0 \end{aligned} \quad (134)$$

where we have introduced

$$\overline{\Delta p}(z_0) = \frac{2}{1-\lambda^2} \int_k^1 \Delta p(r_0, z_0) \sigma_0 d\sigma_0 \quad (135)$$

and the quantities  $A_{mBk}(z, z_0)$  and  $V_{mBk}(r_0, z, z_0)$  are defined in Eqs. (114) and (117).

The first property of this solution to be examined is the limiting pressure rise between points far upstream and far downstream of the blade row. Since for subsonic flow the solution decays as  $z \rightarrow -\infty$ , the limiting value of the static pressure rise is simply the limiting value of  $p$  for  $z \rightarrow +\infty$ . All terms except the first decay and so

$$p(z \rightarrow \infty) = \frac{\omega B}{2\pi\beta^2 U} \int_0^{c_*} \Delta p(z_0) dr_0 \quad (136)$$

This result agrees with that obtained from the vortex theory of Okurounmu and McCune.<sup>42</sup> In the present formulation its origin is in the  $n=0, k=0$  term in the dipole solution. When we initially considered the pressure dipole formulation of the loading problem, this term was omitted, and the erroneous result of no limiting pressure rise was found. After tracing the difficulty to a missing term in the source or monopole solution, that solution was revised as discussed in Section IV-B. When the corresponding correction was made in the dipole solution, the result for the pressure rise given in Eq. (136) was obtained.

Namba<sup>49</sup> reports a limiting static pressure rise even though his monopole and dipole expressions do not contain the  $n=0, k=0$  terms found here. However, his result for the pressure rise differs from Eq. (136) in two respects. First of all, he finds a nonvanishing pressure perturbation for  $z \rightarrow -\infty$ , one half of the static pressure rise occurring between upstream infinity and the rotor with the other half occurring downstream. Also, his result contains a "scale factor" which introduces an additional radial dependence into the integrations over radius in Eqs. (134) to (136). Based on the tests we have made on the singularity solutions, and those described below for the flow field of a lifting rotor, we have concluded that this factor should not be present.

## 2. Expressions for the Velocity Components

In the pressure dipole representation of the blade row, the velocity field must be found by integrating the momentum equations along the undisturbed stream direction. This situation in the dipole approach somewhat compensates for avoiding the distribution of singularities over the blade wakes, as would be necessary if fluid doublets were used to find the velocity potential. As for the thickness case the velocity field will be found in terms of the components  $v_z$ ,  $v_n$ , and  $v_r$ .

For subsonic flow the streamwise velocity perturbation,  $v_z$ , is found from Eq. (53). If  $\frac{d\phi}{dn}$  is expressed in terms of the derivatives  $\left(\frac{\partial}{\partial z}\right)_{r,\zeta}$  and  $\left(\frac{\partial}{\partial \zeta}\right)_{z,r}$  then integration of the normal momentum equation, Eq. (52b), along the undisturbed streamlines yields

$$v_n = \left(\frac{\omega r}{U}\right) \frac{\phi}{\rho_\infty U_R} - \frac{1}{\rho_\infty U_R} \left[ \frac{1}{r} \left(1 + \frac{\omega^2 r^2}{U^2}\right) \right] \frac{\partial}{\partial \zeta} \int_{-\infty}^z \phi(r, \zeta, z') dz' + \frac{1}{\rho_\infty U_R} \sqrt{1 + \left(\frac{\omega r}{U}\right)^2} \int_{-\infty}^z F_B(r, \zeta, z') dz' \quad (137)$$

where  $z'$  is a dummy variable of integration. Note that  $r$  and  $\zeta$  are held constant in this integration. In keeping with the generalized function approach to the singularities, a body-force term representing the blade forces,  $F_B$ , has been included. Since this force acts normal to the undisturbed stream direction in the linearized theory, it appears only in the  $v_n$  expression. Before proceeding further, this contribution to  $v_n$  is evaluated. Each blade contributes a force per unit volume of

$$-\bar{n} \Delta \phi(r, s) \delta(n - n_j)$$

where  $\bar{n}$  is the unit vector normal to the undisturbed stream surface (see Figure 20),  $n$  is a coordinate in this direction, and  $n_j$  is the value of  $n$  at the  $j^{\text{th}}$  blade. The total force on the fluid due to the  $j^{\text{th}}$  blade,  $\vec{F}_j$ , is then

$$\vec{F}_j = - \int_{n_j^-}^{n_j^+} \int_{S_{B_j}} \vec{n} \Delta p(r, s) \delta(n - n_j) dS_B dn = - \int_{S_{B_j}} \vec{n} \Delta p(r, s) dS_B \quad (138)$$

Returning to the term in question, the coordinate  $n$  is expressed in terms of  $\xi$  and  $r$  by

$$n = \frac{r \xi}{\sqrt{1 + \left(\frac{\omega r}{U}\right)^2}} \quad (139)$$

and so we must have

$$\delta(n - n_j) = \frac{\sqrt{1 + \left(\frac{\omega r}{U}\right)^2}}{r} \delta(\xi - \xi_j) \quad (140)$$

Substituting these results, the term in  $v_n$  containing the body-force representation of the blade forces is

$$\frac{1}{\rho_\infty U} \int_{-\infty}^z F_\theta dz' = - \frac{\left[1 + \left(\frac{\omega r}{U}\right)^2\right]}{\rho_\infty U R r} \sum_{j=0}^{s-1} \delta\left(\xi - \frac{2j\pi}{B}\right) \int_0^{c_n} \Delta p(r, z') H(z - z') dz' \quad (141)$$

where we have accounted for the fact that the blades are located on the surfaces  $\xi = \frac{2j\pi}{B}$ , between the axial stations  $z=0$  and  $z=c_n$ . As we shall see, this term will be cancelled by other terms in  $v_n$ . For now the remaining terms in  $v_n$  will be designated  $v_n'$ . If the blade forces were treated as surface forces, then only  $v_n'$  would be present at this point; the delta function terms still present would be excluded from the value of  $v_n$  on the blade surface on the grounds that the singularities are within this surface.

The expression for  $v_r$  which results from integrating the radial momentum equation, Eq. (49a), is

$$v_r = - \frac{1}{\rho_\infty U} \frac{\partial}{\partial r} \int_{-\infty}^z p(r, \xi, z') dz' \quad (142)$$

Eqs. (137) and (142) show that the calculation of the velocity components requires the integration of  $p$  along the stream direction. The required integral is denoted by  $I(z)$  where

$$I(z) = \int_{-\infty}^z \rho(r, \xi, z') dz' \quad (143)$$

Substituting for  $\rho$  from Eq. (134) and doing the  $z'$  integration yields

$$\begin{aligned} I(z) = & \frac{\omega B}{2\pi\beta^2 U} \int_0^{c_n} \Delta p(z_0) (z-z_0) H(z-z_0) dz_0 \\ & + \frac{B}{4\pi\beta^2 r_r^2} \int_{r_H}^{r_r} \int_0^{c_n} \sum_{m=-\infty}^{\infty} \sum_{k=1}^{\infty} \frac{R_{mBk}(\sigma) R_{mBk}(\sigma_0)}{\omega \lambda_{mBk}} e^{imB\xi} \\ & \cdot \left\{ \frac{2imB \lambda_{mBk}}{\left[ \left( \frac{mB}{\beta^2} \right)^2 + \lambda_{mBk}^2 \right]} \left[ \frac{1 + \left( \frac{\omega r_0}{U} \right)^2}{\frac{\omega r_0}{U}} \right] H(z-z_0) + \frac{V_{mBk}(r_0, z, z_0)}{\Lambda_{mBk}(z, z_0)} e^{-\Lambda_{mBk}(z, z_0)(z-z_0)} \right\} \\ & \cdot \Delta p(r_0, z_0) dz_0 dr_0 \end{aligned} \quad (144)$$

Now the results for  $\rho$  and  $I(z)$  can be combined according to Eq. (137) in order to obtain  $v_n$ . Since the explicit representation of the blade force is omitted, the remaining terms are denoted  $v_n'$ .

$$\begin{aligned} v_n' = & \frac{\omega B}{2\pi\beta^2 U} \frac{\left( \frac{\omega r}{U} \right)}{\rho_n U_R} \int_0^{c_n} \Delta p(z_0) H(z-z_0) dz_0 \\ & + \frac{B}{2\pi\beta^2 r_r^2 \rho_n U_R} \left[ \frac{1 + \left( \frac{\omega r}{U} \right)^2}{\frac{\omega r}{U}} \right] \int_{r_H}^{r_r} \int_0^{c_n} \sum_{m=-\infty}^{\infty} \sum_{k=1}^{\infty} R_{mBk}(\sigma) R_{mBk}(\sigma_0) e^{imB\xi} \\ & \cdot \left[ \frac{(mB)^2}{\left( \frac{mB}{\beta^2} \right)^2 + \lambda_{mBk}^2} \right] \left[ \frac{1 + \left( \frac{\omega r}{U} \right)^2}{\frac{\omega r_0}{U}} \right] H(z-z_0) \Delta p(r_0, z_0) dz_0 dr_0 \quad (145) \\ & + \frac{B}{4\pi\beta^2 r_r^2 \rho_n U_R} \int_{r_H}^{r_r} \int_0^{c_n} \sum_{m=-\infty}^{\infty} \sum_{k=1}^{\infty} \frac{R_{mBk}(\sigma) R_{mBk}(\sigma_0)}{\omega \lambda_{mBk}} e^{imB\xi} V_{mBk}(r_0, z, z_0) \\ & \cdot \left\{ \frac{\omega r}{U} - \frac{imB}{\Lambda_{mBk}(z, z_0)} \left[ \frac{1}{r} \left( 1 + \frac{\omega^2 r^2}{U^2} \right) \right] \right\} e^{-\Lambda_{mBk}(z, z_0)(z-z_0)} \Delta p(r_0, z_0) dz_0 dr_0 \end{aligned}$$



The expression for  $v_r$ , obtained by combining Eqs. (142) and (144) is,

$$\begin{aligned}
 v_r = & - \frac{B}{4\pi\beta^2 r_r^2 \rho_\infty U} \int_{r_M}^{r_T} \int_0^{z_0} \sum_{m=-\infty}^{\infty} \sum_{k=1}^{\infty} \frac{R'_{mBk}(\sigma) R_{mBk}(\sigma_0)}{\omega \lambda_{mBk}} \left( \frac{K_{mBk}}{r_r} \right) e^{imBz} \\
 & \cdot \left\{ 2imB\lambda_{mBk} H(z-z_0) \left[ \frac{1 + \left(\frac{\omega r_0}{U}\right)^2}{\frac{\omega r_0}{U}} \right] \frac{1}{\left[ \left(\frac{mB}{\beta^2}\right)^2 + \lambda_{mBk}^2 \right]} + \frac{V_{mBk}(r_0, z, z_0)}{\Lambda_{mBk}(z, z_0)} \right. \\
 & \left. \cdot e^{\Lambda_{mBk}(z, z_0)(z-z_0)} \right\} \Delta p(r_0, z_0) \alpha z_0 \alpha r_0 \quad (146)
 \end{aligned}$$

Particular note should be paid to those terms in  $v_n$  and  $v_r$  which do not decay downstream of the rotor. These terms, which are present within the blade row and downstream of it, represent the contribution of the trailing vortex wakes to the velocity field. The flow field produced by these wakes has a helical pattern and, as a consequence of the linearization, the wakes coincide with the undisturbed stream surfaces on which the blades lie. There are no wake terms in  $p$  or  $v_s$ , which should be continuous across these surfaces.

The results given in this section for the lifting-rotor flow field satisfy the global mass and momentum balances presented in Appendix B. In the next section it is demonstrated that the velocity perturbations found for the lifting rotor also exhibit the proper behavior at the blade surfaces.

### 3. Behavior of Velocity Components at the Blade Surfaces and across the Trailing Vortex Wakes

The properties of the above solution for the velocity field of a lifting rotor can be examined in much the same way as was done in the previous section for a nonlifting rotor, although the loading case is somewhat more complicated because of the presence of the trailing vortex wakes. Again the

streamwise, normal, and radial components,  $v_s$ ,  $v_n$ , and  $v_r$ , are considered. First the behavior of  $v_s$  is treated, followed by  $v_r$ . The examination of  $v_n$  will be done last because it provides a natural transition to the discussion of the direct lifting surface theory in the next section.

#### a. Streamwise Velocity Component

Since  $v_s$  is proportional to  $\phi$ , it must contain a discontinuity across the blade surfaces which is in the same proportion to the blade loading,  $\Delta\phi$ . Therefore, it is equivalent to demonstrate the proper behavior of  $v_s$  at the blade surface by showing that the solution for the pressure field contains the correct discontinuity. Again this is done by ordering the series expansions in  $(mB)^{-1}$  and, in particular, isolating a series for which the  $k$  summation can be done and for which the  $m$  summation yields the generalized function  $\zeta_j$ .

As before, the first operation on the expression for  $\phi$  is to perform an integration by parts on the  $z_0$  integral. The result, after some rearrangement, is

$$\begin{aligned}
 \phi = & \frac{\omega B}{2\pi\beta^2 U} \int_0^z \Delta\phi(z_0) dz_0 + \frac{B}{4\pi\beta^2 r_1^2} \int_{r_H}^{r_1} \sum_{m=-\infty}^{\infty} \sum_{k=1}^{\infty} \frac{R_{mBk}(r) F_{mBk}(z_0)}{\lambda_{mBk}} e^{imBz} \\
 & \cdot \left\{ \Delta\phi(r_0, 0) \frac{V_{mBk}(r_0, z, 0)}{\lambda_{mBk}(z, 0)} e^{-\lambda_{mBk}(z, 0)z} - \Delta\phi(r_0, z_0) \frac{V_{mBk}(r_0, z, z_0)}{\lambda_{mBk}(z, z_0)} e^{-\lambda_{mBk}(z, z_0)(z-z_0)} \right. \\
 & + \int_0^{z_0} \frac{V_{mBk}(r_0, z, z_0)}{\lambda_{mBk}(z, z_0)} e^{-\lambda_{mBk}(z, z_0)(z-z_0)} \frac{\partial}{\partial z_0} [\Delta\phi(r_0, z_0)] dz_0 \quad (147) \\
 & \left. + 2imB\lambda_{mBk} \left[ \frac{1 + \left(\frac{\omega r_0}{U}\right)^2}{\left(\frac{\omega r_0}{U}\right)} \right] \frac{1}{\left[\left(\frac{mB}{\beta^2}\right)^2 + \lambda_{mBk}^2\right]} \Delta\phi(r_0, z) \right\} dr_0
 \end{aligned}$$

In order to discuss the behavior of the various terms in this form, it is convenient to write

$$\psi = \frac{\omega B}{2\pi\beta^2 U} \int_0^z \Delta p(z_0) dz_0 + p_1 + p_2 + p_3 + p_4 \quad (148)$$

where  $p_i$  refers to each of the series in braces in Eq. (147), numbered sequentially. Each of the  $m, k$  terms in  $p_1$  and  $p_2$  are  $O(mB)^{-1}$  and are multiplied by the loading at the leading and trailing edges, respectively. In addition, the terms in  $p_1$  contain the exponential factor  $e^{-\lambda_{mk} \frac{\omega z^2}{U}}$  while those in  $p_2$  contain  $e^{-\frac{\omega \lambda_{mk}}{U} (C_a - z)}$ . Away from the leading and trailing edges, the presence of these factors accelerates the convergence of the series. However, at the leading or trailing edge, one or the other of the exponentials approaches unity and the series can diverge. At the trailing edge  $\Delta p$  should vanish according to the Kutta condition, and the convergence properties of the series in  $p_2$  depends on the behavior of  $\Delta p$  as  $z \rightarrow C_a$ . At the leading edge, the linearized analysis contains a singularity in the loading, and so the series for  $p_1$  can be expected to diverge there. The behavior at the leading and trailing edges is more difficult to understand than it was in the thickness case where the slopes of the thickness profile are well defined. Because of their impact on lifting surface calculations, these terms are examined further in the next section.

The series represented by  $p_3$  contains the integral which remains after the integration by parts. Integration of the exponential factors over  $z_0$  introduces a factor which is  $O(mB)^{-1}$  and so each term in  $p_3$  is at most  $O(mB)^{-2}$ . It has been verified that successive integration by parts produces terms of higher order in  $(mB)^{-1}$  and so this series is convergent.

Next consider the series denoted by  $p_4$ . It is this contribution to  $\psi$  that will be shown to contain the discontinuity across the blade surfaces. First the expression for  $p_4$  is rewritten in the form

$$p_4 = -\frac{B}{\pi^2} \sum_{m=1}^{\infty} \sum_{k=1}^{\infty} R_{mk} (K_{mk} \sigma) \frac{\sin(mB\zeta)}{mB} \frac{1}{\beta^2 + \beta^2 \left(\frac{\lambda_{mk}}{mB}\right)^2} \int_{z_0}^z \Delta p(r_0, z) \left[ \frac{1 + \left(\frac{\omega r_0}{U}\right)^2}{\left(\frac{\omega r_0}{U}\right)^2} \right] R_{mk} (K_{mk} \sigma_0) \sigma_0 dz_0 \quad (149)$$

The expression for  $p_4$  is now seen to be  $-S(r, \zeta)$ , the double series function defined in Eq. (121), if we identify  $f(r_0)$  in Eq. (121) with the quantity

$$\frac{1 + \left(\frac{\omega r_0^2}{U}\right)}{r_0} \Delta p(r_0, z)$$

When the final expression obtained for  $S(r, \zeta)$  in Eq. (128) is used here, then

$$p_4 = \frac{B}{2\pi} \zeta_j \Delta p(r, z) + \frac{B}{\pi} \sum_{m=1}^{\infty} \sum_{k=1}^{\infty} R_{mBk}(\sigma) \frac{\sin(mB\zeta)}{(mB)^3} \frac{1}{\left[\left(\frac{K_{mBk}}{mB}\right)^2 + \left(\frac{\omega r_r}{U}\right)^2\right]} \cdot \int_{r_h}^{r_r} \frac{dR_{mBk}}{dr_0} \frac{\partial}{\partial r_0} [\Delta p(r_0, z)] r_0 dr_0 \quad (150)$$

Another integration by parts may be done in the second term in  $p_4$ . The integrated term vanishes as a consequence of the boundary condition that  $\frac{\partial p}{\partial r}$  vanishes at the hub and the tips. The final result for  $p_4$  is

$$p_4 = \frac{B}{2\pi} \zeta_j \Delta p(r, z) - \frac{B}{\pi} \sum_{m=1}^{\infty} \sum_{k=1}^{\infty} R_{mBk}(\sigma) \frac{\sin(mB\zeta)}{(mB)^3} \frac{1}{\left[\left(\frac{K_{mBk}}{mB}\right)^2 + \left(\frac{\omega r_r}{U}\right)^2\right]} \cdot \int_{r_h}^{r_r} R_{mBk}(\sigma) \frac{\partial}{\partial r_0} \left[ r_0 \frac{\partial}{\partial r_0} \Delta p(r_0, z) \right] dr_0 \quad (151)$$

The term containing the generalized function  $\zeta_j$  is the term which contains the discontinuity in  $p$ ; all of the remaining terms converge uniformly for all  $\zeta$  away from the leading or trailing edge and, hence, are continuous across the blade surfaces. If the difference in  $p$  across the blade surfaces is formed,  $p(r, z, \zeta = \frac{2\pi j}{B}) - p(r, z, \zeta = \frac{2\pi(j+1)}{B})$ , then because of the nature of the function  $\zeta_j$ , it can be seen that the definition of  $\Delta p$  given in Eq. (133) is recovered.

Collecting the evaluations of the various terms, the expression for the perturbation pressure at points within the blade row is

$$\begin{aligned}
 p = & \frac{B}{2\pi} \Delta p(r, z) \zeta_1 - \frac{B}{\pi} \sum_{m=1}^{\infty} \sum_{k=1}^{\infty} \frac{R_{mBk}(\sigma) \sin(mB\zeta)}{(mB)^3 \left[ \left( \frac{K_{mBk}}{mB} \right)^3 + \left( \frac{\omega r_T}{U} \right)^2 \right]} \\
 & \cdot \int_{r_{11}}^{r_T} R_{mBk}(\sigma_0) \frac{\partial}{\partial r_0} \left[ r_0 \frac{\partial}{\partial r_0} \Delta p(r_0, z) \right] dr_0 + \frac{\omega B}{2\pi \beta^2 U} \int_0^{c_a} \Delta p(z_0) H(z-z_0) dz_0 \\
 & + \frac{B}{4\pi \beta^2 r_T^2} \int_{r_{11}}^{r_T} \sum_{m=1}^{\infty} \sum_{k=1}^{\infty} \frac{R_{mBk}(\sigma) R_{mBk}(\sigma_0)}{\frac{\omega \lambda_{mBk}}{U}} e^{imB\zeta} \\
 & \cdot \left\{ \Delta p(r_0, 0) \frac{V_{mBk}(r_0, z, 0)}{\Lambda_{mBk}(z, 0)} e^{-\Lambda_{mBk}(z, 0) z} \right. \\
 & - \Delta p(r_0, c_a) \frac{V_{mBk}(r_0, z, c_a)}{\Lambda_{mBk}(z, c_a)} e^{-\Lambda_{mBk}(z, c_a)(z-c_a)} \\
 & \left. + \int_0^{c_a} \frac{V_{mBk}(r_0, z, z_0)}{\Lambda_{mBk}(z, z_0)} e^{-\Lambda_{mBk}(z, z_0)(z-z_0)} \frac{\partial}{\partial z_0} [\Delta p(r_0, z_0)] dz_0 \right\} dr_0
 \end{aligned} \tag{152}$$

When the first two terms are omitted, this expression for  $p$  is valid upstream ( $z < 0$ ) and downstream ( $z > c_a$ ) of the blade row. Thus, away from the leading and trailing edges,  $p$  (and hence  $v_s$ ) is continuous in these regions, and in particular, across the blade wakes.

#### b. Radial Velocity Component

Next, the properties of the expression for the radial velocity are examined, focussing on the terms due to the trailing vortex wakes. The radial velocity is tangential to the wake surfaces and should be discontinuous across them. This behavior can be demonstrated simply, if we consider points far downstream of the rotor where all other terms except the wake term have decayed and Eq. (146) becomes

$$\begin{aligned}
v_r(z \rightarrow +\infty) &= \frac{B}{\pi \rho_\infty U r^2} \int_{r_H}^{r_T} \int_0^{c_a} \sum_{m=1}^{\infty} \sum_{k=1}^{\infty} R_{mBk}'(\sigma) R_{mBk}(\sigma_0) \frac{\sin(mB\xi)}{mB} \\
&\quad \cdot \frac{K_{mBk}}{\frac{\omega r_T}{U}} \left[ \frac{1}{\frac{1}{\beta^2} + \beta^2 \left( \frac{\lambda_{mBk}}{mB} \right)^2} \right] \left[ \frac{1 + \left( \frac{\omega r_0}{U} \right)^2}{\left( \frac{\omega r_0}{U} \right)^2} \right] \Delta p(r_0, z_0) dz_0 dr_0
\end{aligned} \tag{153}$$

Comparing this equation with Eq. (149) shows that  $v_r$  is proportional to  $\frac{\partial p_s}{\partial r}$ . Taking the derivative of the expression for  $p_s$  in Eq. (151) and using the result in Eq. (153), then

$$\begin{aligned}
v_r(z \rightarrow +\infty) &= -\frac{B \xi_z}{2\pi \rho_\infty U} \frac{d}{dr} \int_0^{c_a} \Delta p(r, z_0) dz_0 \\
&\quad + \frac{B}{\pi \rho_\infty U} \int_0^{c_a} \sum_{m=1}^{\infty} \sum_{k=1}^{\infty} \frac{R_{mBk}'(\sigma) \left( \frac{K_{mBk}}{r} \right) \frac{\sin(mB\xi)}{(mB)^3}}{\left[ \left( \frac{K_{mBk}}{mB} \right)^2 + \left( \frac{\omega r_T}{U} \right)^2 \right]} \\
&\quad \cdot \int_{r_H}^{r_T} R_{mBk}(\sigma_0) \frac{\partial}{\partial r_0} \left[ r \frac{\partial \Delta p(r_0, z_0)}{\partial r_0} \right] dr_0 dz_0
\end{aligned} \tag{154}$$

At this point we introduce the blade circulation,  $\Gamma$ , which is defined by

$$\Gamma(r) = \int_0^{c_a} \gamma(r, s) ds \tag{155}$$

where  $\gamma(r, s)$  is the local vortex strength.

$$\gamma(r, s) = \Delta v_s = v_s \left( \xi = \frac{2\pi s^-}{B} \right) - v_s \left( \xi = \frac{2\pi s^+}{B} \right) \tag{156}$$

Substituting for  $\Delta v_s$  in terms of  $\Delta p$  using Eq. (53) and transforming the stream-wise integration to an integration over  $z$ , the circulation is expressed in terms of  $\Delta p(r, z)$  as

$$\Gamma = - \frac{1}{\rho_{\infty} U} \int_0^{c_a} \Delta p(r, z) dz \quad (157)$$

Thus

$$v_r(z \rightarrow +\infty) = \frac{B}{2\pi} \zeta_i \frac{d\Gamma}{dr} - \frac{B}{\pi \rho_{\infty} U} \int_0^{c_a} \sum_{m=1}^{\infty} \sum_{k=1}^{\infty} \frac{R_{mBk}(\sigma) \left( \frac{K_{mBk}}{r} \right)}{\left[ \left( \frac{K_{mBk}}{mB} \right)^2 + \left( \frac{\omega r}{U} \right)^2 \right]} \cdot \frac{\sin(mB\zeta)}{(mB)^3} \int_{r_n}^{r_0} \frac{\partial}{\partial r_0} \left[ r_0 \frac{\partial}{\partial r_0} \Delta p(r_0, z_0) \right] R_{mBk}(\sigma_0) dr_0 \quad (158)$$

The  $\zeta_i$  term produces the expected discontinuity in  $v_r$  across the wakes while the second term is continuous. Forming the difference in  $v_r$  across the blade wake locations according to the same convention adopted for  $\Delta p$ ,

$\Delta v_r = v_r(\zeta = \frac{2\pi l^-}{B}) - v_r(\zeta = \frac{2\pi l^+}{B})$ , we get

$$\Delta v_r = \frac{d\Gamma}{dr} \quad (159)$$

Notice that in this convention  $\Gamma$  is negative when  $\Delta p$  is positive and work is done on the fluid. This result for the jump in  $v_r$  across the wakes is the same as for an isolated wing. The difference here is that the trailing vortex wakes are helical rather than plane surfaces.

### c. Normal Velocity Component

The final task of this section is to develop further the expression for the normal component of the perturbation velocity. As with the expression for  $p$ , the terms in  $v_n'$  are numbered to facilitate the following discussion. From Eq. (145)

$$v_n' = \frac{\omega B}{2\pi \beta^2 U} \left( \frac{\omega r}{U} \right) \frac{1}{\rho_{\infty} U} \int_0^{c_a} \Delta p(z_0) H(z-z_0) dz_0 + (v_n)_1 + (v_n)_2 \quad (160)$$

The term labeled  $(v_n)_1$  contains the wake term, and can be rewritten as follows:

$$\begin{aligned}
(v_n)_1 &= \frac{B}{2\pi r_r^2 \rho_\infty U_n} \left[ \frac{1 + \left(\frac{\omega r}{U}\right)^2}{r} \right] \\
&\cdot \int_{r_H}^{r_r} \int_0^{c_a} \sum_{m=-\infty}^{\infty \prime} \sum_{k=1}^{\infty} R_{mBk}(\sigma) R_{mBk}(\sigma_0) e^{imBz} H(z-z_0) \\
&\cdot \left[ \frac{1}{\frac{1}{\beta^2} + \beta^2 \left(\frac{\lambda_{mBk}}{mB}\right)^2} \right] \left[ \frac{1 + \left(\frac{\omega r_0}{U}\right)^2}{\left(\frac{\omega r_0}{U}\right)^2} \right] \Delta p(r_0, z_0) r_0 dz_0 dr_0
\end{aligned} \tag{161}$$

where it is recalled that the prime on the  $m$  summation denotes that there is no  $m=0$  term. The  $k$ -summation can be rearranged using the same techniques employed to evaluate the series function  $S(r, z)$  in Section IV-C-3. The resulting expression for  $(v_n)_1$  is

$$\begin{aligned}
(v_n)_1 &= \frac{B}{2\pi} \frac{1 + \left(\frac{\omega r}{U}\right)^2}{\rho_\infty U_n r} \int_0^{c_a} \sum_{m=-\infty}^{\infty \prime} \sum_{k=1}^{\infty} R_{mBk}(\sigma) e^{imBz} H(z-z_0) \\
&\cdot \left\{ \int_k^{\prime} \Delta p(r_0, z_0) R_{mBk}(\sigma_0) \sigma_0 d\sigma_0 + \frac{1}{(mB)^2 \left[ \left(\frac{\lambda_{mBk}}{mB}\right)^2 + \left(\frac{\omega r_0}{U}\right)^2 \right]} \right. \\
&\cdot \left. \int_{r_H}^{r_r} \frac{\partial}{\partial r_0} \left[ r_0 \frac{\partial}{\partial r_0} \Delta p(r_0, z_0) \right] R_{mBk}(\sigma_0) dr_0 \right\} dz_0
\end{aligned} \tag{162}$$

The  $k$  summation which includes the first term in braces is just the Fourier-Bessel expansion for  $\Delta p(r, z_0)$ . The corresponding  $m$  summation also can be evaluated if the appropriate  $m=0$  term is added and subtracted so that the following relation can be used.

$$\frac{B}{2\pi} \sum_{m=-\infty}^{\infty} e^{imBz} = \sum_{j=0}^{\infty} \delta\left(z - \frac{2j\pi}{B}\right) \tag{163}$$

Then  $(v_n)_1$  becomes



$$\begin{aligned}
(v_n)_1 &= \frac{1 + \left(\frac{\omega r}{U}\right)^2}{\rho_\infty U_R r} \sum_{j=0}^{B-1} \delta\left(\xi - \frac{2j\pi}{B}\right) \int_0^{c_a} \Delta p(r, z_0) H(z - z_0) dz_0 - \frac{B}{2\pi} \frac{1 + \left(\frac{\omega r}{U}\right)^2}{\rho_\infty U_R r} \\
&\cdot \int_0^{c_a} \Delta p(r, z_0) H(z - z_0) dz_0 + \frac{B}{2\pi} \frac{1 + \left(\frac{\omega r}{U}\right)^2}{\rho_\infty U_R r} \int \sum_{m=-\infty}^{\infty} \sum_{k=1}^{\infty} \quad (164) \\
&\cdot \frac{R_{mBk}(\sigma) e^{imB\xi} H(z - z_0)}{(mB)^2 \left[ \left(\frac{K_{mBk}}{nB}\right)^2 + \left(\frac{\omega r}{U}\right)^2 \right]} \int_{r_H}^{r_0} \frac{\partial}{\partial r_0} \left[ r_0 \frac{\partial}{\partial r_0} \Delta p(r_0, z_0) \right] R_{mBk}(\sigma) dr_0 dz_0
\end{aligned}$$

The first term precisely cancels the blade force term in  $v_n$ , represented as a volume distribution of dipoles in Eq. (141). Thus, we can drop the prime on  $v_n$  and the expression is valid anywhere, including on the blade surfaces.

The next operation performed on  $v_n$  is an integration by parts over  $z_0$  in  $(v_n)_2$ .

$$\begin{aligned}
(v_n)_2 &= \frac{B}{4\pi \beta^2 r^2 \rho_\infty U_R} \int_{r_H}^{r_0} \sum_{m=-\infty}^{\infty} \sum_{k=1}^{\infty} \frac{R_{mBk}(\sigma) R_{mBk}(\sigma)}{\omega \lambda_{mBk}} e^{imB\xi} \\
&\cdot \left\{ L_{mBk}(r, r_0, z, 0) \Delta p(r_0, 0) e^{\lambda_{mBk}(z, 0) z} \right. \\
&- L_{mBk}(r, r_0, z, c_a) \Delta p(r_0, c_a) e^{\lambda_{mBk}(z, c_a)(z - c_a)} \\
&+ \int_0^{c_a} L_{mBk}(r, r_0, z, z_0) e^{\lambda_{mBk}(z, z_0)(z - z_0)} \frac{\partial}{\partial z_0} [\Delta p(r_0, z_0)] dz_0 \\
&+ \frac{2imB}{D_{mBk}} \frac{\omega \lambda_{mBk}}{U} \left[ \frac{\omega r}{U} \frac{1 + \left(\frac{\omega r_0}{U}\right)^2}{\left(\frac{\omega r_0}{U}\right)^2} + \frac{1 + \left(\frac{\omega r}{U}\right)^2}{\frac{\omega r}{U}} \right. \\
&- \left. 2 \frac{1 + \left(\frac{\omega r}{U}\right)^2}{\left(\frac{\omega r}{U}\right)^2} \frac{1 + \left(\frac{\omega r_0}{U}\right)^2}{\left(\frac{\omega r_0}{U}\right)^2} \frac{\left(\frac{mB}{\beta}\right)^2}{D_{mBk}} \right] \Delta p(r_0, z) r_0 \left. \right\} dr_0 \quad (165)
\end{aligned}$$

where

$$L_{m\theta k}(r, r_0, z, z_0) = \frac{V_{m\theta k}(r_0, z, z_0)}{\mathcal{L}_{m\theta k}(z, z_0)} \left\{ \frac{\omega r}{U} - \frac{im\beta}{\mathcal{L}_{m\theta k}(z, z_0)} \left[ \frac{1}{r} \left( 1 + \frac{\omega^2 r^2}{U^2} \right) \right] \right\} \quad (166)$$

and

$$D_{m\theta k} = \left( \frac{m\beta}{\beta^2} \right)^2 + \lambda_{m\theta k}^2 \quad (167)$$

Except near the leading and trailing edges, the first three terms in  $(v_n)_2$  are well-behaved. In the integrated terms evaluated at  $z_n = z$ , the last three terms in Eq. (165), the  $r$ -dependence has been factored in a special way in order to demonstrate that  $v_n$  is continuous across the blade surfaces. The first of these terms comes from the  $p$ -contribution to  $v_n$  in Eq. (137); the other two of these terms derive from the  $I(z)$  contribution to  $v_n$ . The first of the last three terms is just  $(\omega r/U) \frac{1}{\rho_m U_n}$  times the discontinuous part of  $p$ , (see  $p_2$  in Eq. (149)). Hence if  $v_n$  is to be continuous across the blade surfaces, then the last two terms must cancel this discontinuity. In order to simplify the demonstration that such is the case,  $(v_n)_2$  is further subdivided.

$$(v_n)_2 = (v_n)_3 + (v_n)_4 \quad (168)$$

where  $(v_n)_3$  includes the terms containing  $L_{m\theta k}$  and  $(v_n)_4$  can be written, using the definition of  $D_{m\theta k}$  in Eq. (167), as

$$\begin{aligned} (v_n)_4 = & - \frac{B}{\pi \beta^2 r_T^2 \rho_m U_n} \int_{r_H}^{r_T} \sum_{m=1}^{\infty} \sum_{k=1}^{\infty} R_{m\theta k}(\sigma) R_{m\theta k}(\sigma_0) \frac{\sin(m\beta r)}{m\beta} \frac{(m\beta)^2}{\left[ \left( \frac{m\beta}{\beta^2} \right)^2 + \lambda_{m\theta k}^2 \right]} \\ & \cdot \left\{ \frac{\omega r}{U} \left[ \frac{1 + \left( \frac{\omega r_0}{U} \right)^2}{\left( \frac{\omega r_0}{U} \right)^2} \right] + \left[ \frac{1 + \left( \frac{\omega r}{U} \right)^2}{\frac{\omega r}{U}} \right] \right. \\ & \left. - 2 \left[ \frac{1 + \left( \frac{\omega r}{U} \right)^2}{\left( \frac{\omega r}{U} \right)} \right] \left[ \frac{1 + \left( \frac{\omega r_0}{U} \right)^2}{\left( \frac{\omega r_0}{U} \right)} \right] \left[ \frac{i}{\beta^2 + \beta^2 \left( \frac{\lambda_{m\theta k}}{m\beta} \right)^2} \right] \right\} \Delta p(r_0, z) r_0 dr_0 \quad (169) \end{aligned}$$

Now the series containing the first two terms in braces are in the same form as the doubly infinite series evaluated already. The third term in braces can be manipulated in much the same way; the factor containing  $\lambda_{m\beta k}$  is re-written using Eq. (122) and the quantity  $(\frac{\omega r_0}{U})^2 / [1 + (\frac{\omega r_0}{U})^2]$  is added and subtracted to it. When these operations are completed, the form of  $(v_n)_4$  is

$$\begin{aligned}
 (v_n)_4 = & -\frac{B}{\pi \beta^2 r_r^2 \rho_\infty U_R} \int_{r_n}^{r_r} \sum_{m=1}^{\infty} \sum_{k=1}^{\infty} R_{m\beta k}(\sigma) R_{m\beta k}(\sigma_0) \frac{\sin(m\beta \xi)}{m\beta} \\
 & \cdot \frac{(m\beta)^2}{\left[\left(\frac{m\beta}{\beta^2}\right)^2 + \lambda_{m\beta k}^2\right]} \left\{ \left(\frac{\omega r}{U}\right) \left[\frac{1 + \left(\frac{\omega r_0}{U}\right)^2}{\left(\frac{\omega r_0}{U}\right)^2}\right] - \left[\frac{1 + \left(\frac{\omega r}{U}\right)^2}{\frac{\omega r}{U}}\right] \right. \\
 & \left. - 2 \left[\frac{1 + \left(\frac{\omega r}{U}\right)^2}{\frac{\omega r}{U}}\right] \left[\frac{1}{\left(\frac{K_{m\beta k}}{m\beta}\right)^2 + \left(\frac{\omega r_r}{U}\right)^2}\right] \left[\frac{r_r^2}{r_0^2} - \left(\frac{K_{m\beta k}}{m\beta}\right)^2\right] \right\} \Delta p(r_0, z) r_0 dr_0.
 \end{aligned} \tag{170}$$

If the results for  $S(r, \xi)$  in Eq. (121) and  $p_4$  in (149) are used to evaluate the series corresponding to the first two terms in braces, the respective contributions to  $(v_n)_4$  which contain the generalized function,  $\mathcal{E}_j$ , cancel. The differential equation satisfied by the radial eigenfunctions, Eq. (74), can be used to substitute in the third term and then an integration by parts carried out. The final expression for  $(v_n)_4$  is

$$\begin{aligned}
 (v_n)_4 = & \frac{B}{\pi} \frac{\left(\frac{\omega r}{U}\right)}{\rho_\infty U_R} \sum_{m=1}^{\infty} \sum_{k=1}^{\infty} \frac{R_{m\beta k}(\sigma) \sin m\beta \xi}{(m\beta)^3 \left[\left(\frac{K_{m\beta k}}{m\beta}\right)^2 + \left(\frac{\omega r_r}{U}\right)^2\right]} \\
 & \cdot \int_{r_n}^{r_r} \frac{d R_{m\beta k}(\sigma_0)}{d r_0} \frac{\partial}{\partial r_0} \left\{ \Delta p(r_0, z) \left[ 1 - \frac{1 + \left(\frac{\omega r}{U}\right)^2}{\left(\frac{\omega r}{U}\right)^2} \frac{\left(\frac{\omega r_r}{U}\right)^2}{1 + \left(\frac{\omega r_0}{U}\right)^2} \right. \right. \\
 & \left. \left. - 2 \frac{\left(\frac{\omega r_r}{U}\right)^2}{\left[\left(\frac{K_{m\beta k}}{m\beta}\right)^2 + \left(\frac{\omega r_r}{U}\right)^2\right]} \frac{1 + \left(\frac{\omega r}{U}\right)^2}{\left(\frac{\omega r}{U}\right)^2} \right] \right\} r_0 dr_0.
 \end{aligned} \tag{171}$$

The series in  $(v_n)_+$  are uniformly convergent, as are the remaining terms in  $v_n$ , and so we conclude that  $v_n$  is continuous across the blade surfaces. As a prelude to evaluating the full expression for  $v_n$  on the blade surfaces, in order to establish the integral equation for the blade loading, we collect the result for  $v_n$ .

$$\begin{aligned}
 v_n &= \frac{\omega B}{2\pi\beta^2 U} \left(\frac{\omega r}{U}\right) \frac{i}{\rho_\infty U_R} \int_0^{c_a} \overline{\Delta p}(z_0) H(z-z_0) dz_0 \\
 &- \frac{B}{2\pi\rho_\infty U_R r} \left[1 + \left(\frac{\omega r}{U}\right)^2\right] \int_0^{c_a} \Delta p(r, z_0) H(z-z_0) dz_0 \\
 &+ \frac{B}{2\pi\rho_\infty U_R r} \left[i + \left(\frac{\omega r}{U}\right)^2\right] \int_0^{c_a} \sum_{m=-\infty}^{\infty} \sum_{k=1}^{\infty} \frac{R_{mBk}(\sigma) e^{imBz} H(z-z_0)}{(mB)^2 \left[\left(\frac{K_{mBk}}{mB}\right)^2 + \left(\frac{\omega r_r}{U}\right)^2\right]} \\
 &\cdot \int_{r_H}^{r_r} R_{mBk}(\sigma_0) \frac{\partial}{\partial r_0} \left[r_0 \frac{\partial}{\partial r_0} \Delta p(r_0, z_0)\right] dr_0 dz_0 \\
 &+ \frac{B}{2\pi\beta^2 r_r^2 \rho_\infty U_R} \int_{r_H}^{r_r} \sum_{m=-\infty}^{\infty} \sum_{k=1}^{\infty} \frac{R_{mBk}(\sigma) R_{mBk}(\sigma_0)}{\frac{\omega \lambda_{mBk}}{U}} e^{imBz} \\
 &\cdot \left\{ L_{mBk}(r, r_0, z, 0) \Delta p(r_0, 0) e^{\Lambda_{mBk}(z, 0) z} \right. \\
 &- L_{mBk}(r, r_0, z, c_a) \Delta p(r_0, c_a) e^{\Lambda_{mBk}(z, c_a)(z-c_a)} \\
 &+ \left. \int_0^{c_a} L_{mBk}(r, r_0, z, z_0) \frac{\partial}{\partial z_0} [\Delta p(r_0, z_0)] e^{\Lambda_{mBk}(z, z_0)(z-z_0)} dz_0 \right\} dr_0 \\
 &+ (v_n)_+
 \end{aligned} \tag{172}$$

where  $(v_n)_d$ , given in Eq. (171), is not written out because it vanishes on the blade surfaces. The quantity  $L_{m\beta k}(r, r_0, z, z_0)$ , defined by Eq. (166), has been rationalized and written in the form

$$L_{m\beta k}(r, r_0, z, z_0) = \frac{1}{D_{m\beta k}^2} \left[ C_{m\beta k}^{(1)}(z, z_0) \left( \frac{\omega r_0}{U} \frac{\omega r}{U} \right) \right. \\ \left. + C_{m\beta k}^{(2)}(z, z_0) \left( \frac{r}{r_0} + \frac{r_0}{r} \right) + C_{m\beta k}^{(3)}(z, z_0) \left( \frac{\omega r}{U} \frac{\omega r_0}{U} \right)^{-1} \right] \quad (173)$$

where  $D_{m\beta k}$  is defined in Eq. (167). The coefficients of the different radial factors in Eq. (173),  $C_{m\beta k}^{(l)}(z, z_0)$ , are complex quantities, i.e.,

$$C_{m\beta k}^{(l)}(z, z_0) = A_{m\beta k}^{(l)} + i B_{m\beta k}^{(l)}(z, z_0)$$

The real and imaginary parts,  $A_{m\beta k}^{(l)}$  and  $B_{m\beta k}^{(l)}(z, z_0)$ , are written out in Table 5.

The formulation of the loading problem with the pressure dipole approach is now complete. Expressions given in Sections IV-D1 and IV-D2 for the pressure and velocity fields have been shown to satisfy global mass and momentum conservation, and to display the correct behavior at the blade and wake locations. The result given in Eq. (172) for the normal or upwash velocity is used next to develop a direct lifting surface analysis.

TABLE 3

Coefficients in the Expression for the Normal Velocity  
Component of a Lifting Rotor, Eq. (172)

<u><math>l</math></u>	<u><math>A_{mBk}^{(l)}</math></u>
1	$-\frac{(mB)^4 M^4}{\beta^2} + \frac{(mB)^2 \lambda_{mBk}^2}{\beta^4} (1 - 4M^2 + M^4) - \lambda_{mBk}^4$
2	$\frac{(mB)^2}{\beta^2} \left[ \left( \frac{mB}{\beta^2} \right)^2 M^2 + (2 - M^2) \lambda_{mBk}^2 \right]$
3	$-(mB)^2 \left[ \left( \frac{mB}{\beta^2} \right)^2 - \lambda_{mBk}^2 \right]$
<u><math>l</math></u>	<u><math>B_{mBk}^{(l)}(z, z_0)</math></u>
1	$-2 mB \lambda_{mBk} \operatorname{sgn}(z - z_0) \left[ \left( \frac{mB}{\beta^2} \right)^2 M^2 + \lambda_{mBk}^2 \right]$
2	$mB \lambda_{mBk} \operatorname{sgn}(z - z_0) \left[ (1 - 2M^2) \left( \frac{mB}{\beta^2} \right)^2 - \lambda_{mBk}^2 \right]$
3	$2 mB \lambda_{mBk} \operatorname{sgn}(z - z_0) \frac{(mB)^2}{\beta^2}$

## E. DIRECT LIFTING SURFACE THEORY

The formal solution for the loading contribution to the flow field of a rotor can now be applied to the direct lifting surface problem. An integral equation is derived which relates the unknown blade loading to a specified blade geometry. This derivation is accomplished by evaluating the normal component of the perturbation velocity, Eq. (172), at the blade surface, and using the flow tangency condition to relate it to the blade camber line. The resulting linear integral equation for  $\Delta\phi$  is then nondimensionalized, and what appears to be a promising solution procedure is discussed.

### 1. Formulation of the Integral Equation

Due to the periodic nature of Eq. (172), and the fact that all blades are assumed identical, it makes no difference on which of the blade surface streamlines,  $\zeta = \frac{2\pi j}{B}$   $j = 0, 1, 2, \dots$ , we choose to specify conditions. Two simplifications are immediately apparent when  $v_n$  is evaluated at a blade surface:  $(v_n)_s$ , as given by Eq. (171), vanishes, and in the other terms of Eq. (172), the complex exponentials involving  $\zeta$  become unity.

At this point some discussion of the integrated terms proportional to  $\Delta\phi(r_o, 0)$  and  $\Delta\phi(r_o, c_a)$  is in order. Analogous to subsonic isolated airfoil theory, the Kutta condition is assumed to be satisfied at the trailing edge; i.e., the loading  $\Delta\phi(r_o, c_a)$  vanishes so that this term need no longer be carried. The leading edge term, on the other hand, poses a problem of interpretation. The loading on a subsonic, isolated airfoil is known to approach infinity as the minus one-half power of the distance from the leading edge.<sup>53</sup> Again, we can expect analogous behavior in the present situation, implying that the quantity  $\Delta\phi(r_o, 0)$  is singular. This also implies that the integrand containing  $\partial\Delta\phi/\partial z_o$  now contains a minus three-halves power singularity, which is not integrable in the usual sense. However, note that the original expression for  $v_n$  before performing the integration by parts with respect to  $z_o$ , Eq. (145), involved only integrations over  $\Delta\phi(r_o, z_o)$ .

Hence it contained only an integrable singularity, and would thus give a finite result. This strongly suggests that the infinities in Eq. (172) are self-cancelling, and that only the finite part of the expression remains.

Following Mangler,<sup>54</sup> the singularity in the integrand can be displayed explicitly, with the other factors being expanded in Taylor series in the vicinity of the leading edge. Such a procedure shows that the infinities do indeed cancel, and that the appropriate way to write the terms in question is with the leading edge term proportional to  $\Delta p(r_0, \epsilon)$ , and the last integral taken with  $\epsilon$  as the lower limit of integration, where  $\epsilon$  is some small but finite number. This will always yield a finite result, and amounts to neglecting the contribution from a strip of width  $\epsilon$  near the leading edge. However this contribution is easily shown to be of order  $\epsilon^{1/2}$  and hence can be made negligible by choosing  $\epsilon$  sufficiently small.

It is also useful to eliminate any complex quantities from the expression for  $v_n$ , since on physical grounds it must be a real quantity. This can be verified from Eq. (172) by first recognizing that the  $R_{mB\pm}$  are real and are odd functions of the index  $m$ ; thus, the product  $R_{mB\pm}(\sigma)R_{mB\pm}(\sigma_0)$  is even with respect to  $m$ . From here it is easy to show that the  $(-m)$  terms are the conjugates of the corresponding  $(+m)$  terms, and so the doubly infinite sum over  $m$  will always yield a real result for  $v_n$ . This suggests the calculation can be shortened considerably by considering only  $m \geq 0$ , i.e.,

$$\sum_{m=-\infty}^{\infty} ( ) = 2 \sum_{m=1}^{\infty} R_e ( ) \quad \sum_{m=-\infty}^{\infty} ( ) = 2 \sum_{m=0}^{\infty} [1 - \frac{1}{2} \delta_{n,0}] R_e ( ) \quad (173)$$

where  $\delta_{m,n}$ , the Kronecker delta,

$$\delta_{mn} = 1 \quad m = n \\ = 0 \quad m \neq n$$

is used to avoid counting the zeroth term twice.



The next step is to relate  $v_n$  on the left-hand side of Eq. (172) to the prescribed blade geometry, which in the loading case means the blade camber line. (As used here, the camber line includes any mean angle of attack). As pointed out in Section IV-C i, this is not as straightforward as it is in isolated airfoil theory because of the so-called "camber due to thickness". A row of blades with this camber distribution is by definition unloaded, and so represents the zero reference in any loading calculation. Thus,  $v_n$  in the loading case must be continuous across the blades and satisfy the flow tangency condition with respect to the following camber line,

$$\eta_{cl}(s, r) = \eta_c(s, r) - \eta_{ct}(s, r) \quad (174)$$

where  $\eta_c$  is the geometric camber of Figure 21 and  $\eta_{ct}$  is the thickness-induced camber given by

$$\begin{aligned} \eta_{ct} &= \frac{1}{U_R} \int_0^s (v_n)_{cont} ds' \\ &= \frac{1}{U} \int_0^z (v_n)_{cont} dz' \end{aligned} \quad (175)$$

Here  $(v_n)_{cont}$  is the portion of  $v_n$  in Eq. (130) which is continuous across the blades, and the integral is understood to be along  $\zeta=0$  at constant radius.

For a blade with thickness, it is assumed now that  $\eta_{ct}$  has been determined so that  $\eta_{cl}$  is known; alternatively, one can consider the results below as applying to a blade with zero thickness, in which case  $\eta_{ct}$  is obviously zero. In either case, the left hand side of Eq. (172) is replaced by

$$\begin{aligned} (v_n)_{\zeta=0} &= U_R \left. \frac{\partial \eta_{cl}(s, r)}{\partial s} \right)_{n, r} \\ &= U \left. \frac{\partial \eta_{cl}(z, r)}{\partial z} \right)_{\theta, r} \end{aligned} \quad (176)$$

to insure that the flow remains parallel to the loading camber line. Here  $\eta_{cl}(z, r)$  is understood to be  $\eta_{cl}(s = \sqrt{1 + (\frac{\omega r}{U})^2} z, r)$  when both  $s$  and  $z$  are assumed to originate at the leading edge of the reference blade, and use has been made of Eq. (51a).

When all the above steps are taken, Eq. (172) yields the following integral equation for  $\Delta p$ :

$$\begin{aligned}
 U \frac{\partial \eta_{cl}(z, r)}{\partial z} \Big|_{\theta, r} &= \frac{B \left(\frac{\omega r}{U}\right)^2}{\pi \rho_\infty U_R r \beta^2 (1-h^2)} \int_0^{c_a} d z_0 \int_h^1 d \sigma_0 \Delta p(r_0, z_0) \sigma_0 \\
 &- \frac{B \left[1 + \left(\frac{\omega r}{U}\right)^2\right]}{2 \pi \rho_\infty U_R r} \left\{ \int_0^{c_a} \Delta p(r, z_0) H(z-z_0) d z_0 - \frac{2}{\beta^2 \left(\frac{\omega r}{U}\right)^2} \int_0^{c_a} d z_0 \sum_{m=1}^{\infty} \sum_{k=1}^{\infty} \right. \\
 &\cdot \left. \frac{R_{mBk}(\sigma) H(z-z_0)}{D_{mBk}} \int_{r_h}^{r_0} d r_0 \left( r_0 \frac{\partial^2 \Delta p}{\partial r_0^2} + \frac{\partial \Delta p}{\partial r_0} \right) R_{mBk}(\sigma_0) \right\} \\
 &+ \frac{B}{2 \pi \rho_\infty U_R \beta^2 r^2} \int_{r_h}^{r_0} \sum_{m=0}^{\infty} \sum_{k=1}^{\infty} \frac{(1 - \frac{1}{2} \delta_{m0}) R_{mBk}(\sigma) R_{mBk}(\sigma_0)}{\frac{\omega}{U} \lambda_{mBk} D_{mBk}^2} \left\{ \Delta p(r_0, \epsilon) e^{-\lambda_{mBk} \frac{\omega}{U} z} \right. \\
 &\cdot \left[ G_{mBk}^{(1)}(z, 0) \left(\frac{\omega r_0}{U} \frac{\omega r}{U}\right) + G_{mBk}^{(2)}(z, 0) \left(\frac{r}{r_0} + \frac{r_0}{r}\right) + G_{mBk}^{(3)}(z, 0) \left(\frac{\omega r}{U} \frac{\omega r_0}{U}\right)^{-1} \right] \\
 &+ \int_\epsilon^{c_a} \frac{\partial \Delta p(r_0, z_0)}{\partial z_0} e^{-\lambda_{mBk} \frac{\omega}{U} |z-z_0|} \left[ G_{mBk}^{(1)}(z, z_0) \left(\frac{\omega r}{U} \frac{\omega r_0}{U}\right) \right. \\
 &\left. + G_{mBk}^{(2)}(z, z_0) \left(\frac{r}{r_0} + \frac{r_0}{r}\right) + G_{mBk}^{(3)}(z, z_0) \left(\frac{\omega r}{U} \frac{\omega r_0}{U}\right)^{-1} \right] d z_0 \Big\} d r_0
 \end{aligned} \tag{177}$$

where for convenience we have defined

$$G_{mBk}^{(l)}(z, z_0) = A_{mBk}^{(l)} \cos \frac{mB}{\beta^2} \frac{\omega}{U} (z-z_0) - B_{mBk}^{(l)}(z, z_0) \sin \frac{mB}{\beta^2} \frac{\omega}{U} (z-z_0) \tag{178}$$

for  $l = 1, 2, 3$ ; the  $A_{mBk}^{(l)}$ 's and  $B_{mBk}^{(l)}$ 's are as given in Table 3.

Before considering the nature of this equation, it is convenient to nondimensionalize the variables. In the radial direction, we retain the use of  $\sigma = \frac{r}{r_T}$  as the dimensionless variable. For the axial direction, in keeping with the usual convention in isolated airfoil theory, we nondimensionalize by  $c_a/2$  and shift the origin to midchord. Thus, we define

$$\lambda = \frac{z - \frac{c_a}{2}}{\frac{c_a}{2}} \quad (179)$$

so that now the blades lie between  $h \leq \sigma \leq 1$  and  $-1 \leq \lambda \leq 1$ . For convenience in specifying the blade row geometry, we also define the parameters

$$\phi_T = \frac{\omega r_T}{U} \quad \eta_T = \frac{c_a}{2r_T} \quad (180)$$

$\phi_T$  is the inverse of the usual flow coefficient at the tip;<sup>32</sup>  $\eta_T$  can be related to either the aspect ratio or the solidity at the tip (based on  $c_a$  rather than  $c$ ):

$$\text{Aspect ratio} = \frac{r_T - r_h}{c_a} = \frac{r_T}{c_a} (1 - h) = \frac{1 - h}{2\eta_T} \quad (181)$$

$$\text{Solidity at tip} = \frac{B c_a}{2\pi r_T} = \frac{B \eta_T}{\pi} \quad (182)$$

We next note that since quantities like  $\lambda_{m\theta k}$ ,  $G_{m\theta k}$ ,  $A_{m\theta k}^{(2)}$ ,  $B_{m\theta k}^{(1)}$  and  $D_{m\theta k}$  are already dimensionless, we need only rewrite them in terms of the above. Hence, we get

$$\lambda_{m\theta k} = \begin{cases} \frac{mB}{\beta\phi_T} \left[ \left( \frac{K_{m\theta k}}{mB} \right)^2 - \left( \frac{\phi_T M}{\beta} \right)^2 \right]^{1/2} & m \neq 0 \\ \frac{K_{0k}}{\beta\phi_T} & m = 0 \end{cases} \quad (183)$$

Also

$$D_{m\theta k} = \begin{cases} \left( \frac{mB}{\beta\phi_T} \right)^2 \left[ \left( \frac{K_{m\theta k}}{mB} \right)^2 + \phi_T^2 \right] & m \neq 0 \\ \left( \frac{K_{0k}}{\beta\phi_T} \right)^2 = \lambda_{0k}^2 & m = 0 \end{cases} \quad (184)$$

and

$$G_{m\theta k}^{(2)}(X, X_0) = A_{m\theta k}^{(1)} \cos \frac{mB}{\beta^2} \phi_r \eta_r (X - X_0) - B_{m\theta k}^{(1)}(X, X_0) \sin \frac{mB}{\beta^2} \phi_r \eta_r (X - X_0) \quad (185)$$

The expressions defining  $A_{m\theta k}^{(1)}$  and  $B_{m\theta k}^{(1)}$  can be used as they stand in Table 3.

As for the dependent variables, such as velocity and pressure, it is natural to normalize them by the axial velocity,  $U$ , and dynamic pressure,  $\frac{1}{2} \rho_\infty U^2$ , respectively. Thus we define

$$\hat{v}_n = \frac{v_n}{U} \quad \hat{M}_{cL} = \frac{2 \eta_{cL}}{C_a} \quad \hat{p} = \frac{p}{\frac{1}{2} \rho_\infty U^2} \quad (186)$$

With these definitions, Eq. (177) becomes:

$$\begin{aligned} \left. \frac{\partial \hat{M}_{cL}}{\partial X} \right)_{\theta, \sigma} &= \frac{B \phi_r^2 \eta_r \sigma}{2\pi \beta^2 (1 - k^2) (1 + \phi_r^2 \sigma^2)^{1/2}} \int_{-1}^{+1} dX_0 \int_k^1 d\sigma_0 \Delta \hat{p}(\sigma_0, X_0) \sigma_0 \\ &- \frac{B \eta_r (1 + \phi_r^2 \sigma^2)^{1/2}}{4\pi \sigma} \left\{ \int_{-1}^{+1} \Delta \hat{p}(\sigma_0, X_0) H(X - X_0) dX_0 - \frac{2}{(\beta \phi_r)^2} \int_{-1}^{+1} dX_0 \sum_{m=1}^{\infty} \sum_{k=1}^{\infty} \right. \\ &\cdot \left. \frac{R_{m\theta k}(\sigma) H(X - X_0)}{D_{m\theta k}} \int_k^1 d\sigma_0 \left( \sigma_0 \frac{\partial^2 \Delta \hat{p}}{\partial \sigma_0^2} + \frac{\partial \Delta \hat{p}}{\partial \sigma_0} \right) R_{m\theta k}(\sigma_0) \right\} \\ &+ \frac{B}{4\pi \phi_r \beta^2 (1 + \phi_r^2 \sigma^2)^{1/2}} \int_k^1 \sum_{m=0}^{\infty} \sum_{k=1}^{\infty} \frac{(1 - \frac{1}{2} \delta_{m0}) R_{m\theta k}(\sigma) R_{m\theta k}(\sigma_0)}{\lambda_{m\theta k} D_{m\theta k}^2} \\ &\cdot \left\{ \Delta \hat{p}(\sigma_0, -1 + \epsilon) e^{-\lambda_{m\theta k} \phi_r \eta_r (X + \epsilon)} \left[ \phi_r^2 G_{m\theta k}^{(1)}(X, -1) (\sigma \sigma_0) \right. \right. \\ &+ G_{m\theta k}^{(2)}(X, -1) \left( \frac{\sigma}{\sigma_0} + \frac{\sigma_0}{\sigma} \right) + \phi_r^{-2} G_{m\theta k}^{(3)}(X, -1) (\sigma \sigma_0)^{-1} \left. \right] \\ &+ \int_{-1 + \epsilon}^{+1} \frac{\partial \Delta \hat{p}}{\partial X_0} e^{-\lambda_{m\theta k} \phi_r \eta_r |X - X_0|} \left[ \phi_r^2 G_{m\theta k}^{(1)}(X, X_0) (\sigma \sigma_0) \right. \\ &+ G_{m\theta k}^{(2)}(X, X_0) \left( \frac{\sigma}{\sigma_0} + \frac{\sigma_0}{\sigma} \right) + \phi_r^{-2} G_{m\theta k}^{(3)}(X, X_0) (\sigma \sigma_0)^{-1} \left. \right] dX_0 \left. \right\} d\sigma_0 \end{aligned} \quad (187)$$

The next step is to consider the behavior of the integrand. In isolated airfoil theory, singularities generally appear as the source  $(\sigma_0, x_0)$  and field  $(\sigma, x)$  point approach one another, and we must expect such behavior here. In our case however, they would appear as divergent series, so that the nature of the singularity is not immediately obvious. Preliminary consideration of the series in Eq. (187) when the source and field points coincide suggests that for fixed  $k$ , the terms in the integrand decay only as  $(m\beta)^{-1}$ , and for fixed  $m\beta$  as  $(k)^{-1}$ , thus indicating potential convergence problems. (It should be noted here that this in no way contradicts the earlier statement that the  $m$  series occurring in Eq. (172) for  $v_n$  is uniformly convergent. There we were considering the integrated expression for  $v_n$ , and hence could make the use of the fact that the integration over  $z_0$  of the exponential arguments would yield an extra factor of  $(m\beta)^{-1}$ . Here we are considering the behavior of the integrand near  $x = x_0$ , at which point the exponentials all reduce to unity, and hence cannot aid in the convergence).

The nature of these singularities has not yet been determined, and so a detailed discussion of the convergence of these series is deferred until then. Once the form of the singularity is determined, it is anticipated that its influence can be subtracted out and isolated, much as the discontinuous portions of  $\phi$  and  $v_r$  were isolated in Section IV-D-3. In addition to facilitating the evaluation of the improper integrals which occur, the isolation of the singularity will serve another very useful purpose. In any numerical scheme, the infinite series over the azimuthal and radial mode numbers must be truncated after a finite number of terms; since all series would be convergent after the above separation, a much better estimate of the truncation error should result.

## 2. Progress Toward the Solution

Despite the fact that this singularity has not yet been isolated, some progress has been made toward the inversion of Eq. (187). This equation is obviously too complex to hold any hope for an analytical solution,

and so various numerical schemes employed successfully in past lifting-surface studies<sup>55,56</sup> have been reviewed. The schemes all appear to fall into one of two basic categories. The first involves the idealization of the distributed loading as a lattice of discrete loading elements (i.e., vortices, dipoles, etc.) whose strengths are constant, but initially unknown. The second approach is to represent the continuous loading as a double series of suitable functions in the chordwise and spanwise variables, the coefficients in which are initially unknown. This is also sometimes referred to as a kernel function approach.

In either case, one then requires that the velocity be parallel to the blade surface at each of a set of suitably chosen collocation points. This reduces the integral equation to a set of simultaneous linear algebraic equations which can be expressed as a matrix equation. The rank of the matrix equals the number of unknowns, which in turn equals the number of collocation points for the system to be determinant. One can also choose the number of collocation points to exceed the number of unknowns, in which case the boundary condition at the surface can only be satisfied in a least-squares sense.<sup>56,57</sup>

The solution of a matrix equation, whether for the unknown strengths of the source lattice or for the unknown coefficients in the series expansion, is thus common to both approaches. This portion of the solution is relatively straightforward and rapid. It is in determining the elements of the coefficient matrix that the most time is usually consumed,<sup>56</sup> and it is here that the two techniques differ significantly, with each having advantages in certain problems.

The greatest advantage of the lattice methods is that no numerical quadratures are needed to determine the coefficient matrix. Moreover, provided the source and collocation points are never coincident, the problems mentioned above in treating the singularity are evidently avoided.<sup>58</sup> However, since one only solves for the loading at a set of discrete locations, there is some ambiguity involved in how best to interpolate for the loadings at other positions. (A general discussion of this point is given in Chapter 3 of Reference 57.)

We feel that the series expansion approach has several overriding advantages in the present problem, the principal one being that it enables one to express the loading, as well as its derivatives, uniquely at every point on the surface. Through judicious choice of the loading functions in the series expansion, one can also include the appropriate behavior at the leading and trailing edges automatically.<sup>53,55</sup> The principal disadvantage is that numerical quadratures usually are required for the elements of the coefficient matrix, which for our kernel function would likely be rather time-consuming.

Fortunately, there appears to be a strong possibility that, once the singularity has been treated separately, the remaining spanwise integrations can all be done analytically. To see this, note that the  $\sigma_0$  integrals in Eq. (187) involve only products of  $\sigma_0^{n-1} R_{mBk}(K_{nBk}\sigma_0)$  with  $\Delta\phi$  or its derivatives. Further, if we expand the radial dependence of  $\Delta\phi$  in a simple power series, then the integrals will still involve only products of  $R_{mBk}$  with integral powers of  $\sigma_0$ . Then, since the  $R_{mBk}$  are linear combinations of  $J_{mB}$  and  $Y_{mB}$  (see Appendix A), use can be made of the indefinite integral:<sup>59</sup>

$$\int \xi^\mu \begin{Bmatrix} J_n(\xi) \\ Y_n(\xi) \end{Bmatrix} \alpha \xi = (\mu + n + 1) \xi \begin{Bmatrix} J_n(\xi) \\ Y_n(\xi) \end{Bmatrix} S_{\mu-1, n-1}(\xi) - \xi \begin{Bmatrix} J_{n-1}(\xi) \\ Y_{n-1}(\xi) \end{Bmatrix} S_{\mu, n}(\xi) \quad (188)$$

where  $\mu$  and  $n$  are each integers, the  $S_{\mu, n}$  are Lommel's functions and  $\xi$  is a dummy variable for  $K_{nB}\sigma_0$ . Reference 59 gives an easily used asymptotic expansion for the evaluation of the  $S_{\mu, n}$  valid for large argument. Since  $K_{nB}\sigma_0$ , where  $n \in O(1)$ , can be shown to be of the same order as the number of blades, this should be applicable in the majority of cases encountered in the present problem.

One further point needs to be made regarding the radial variation of  $\Delta p$ , and that concerns its behavior as the hard walls at  $\sigma = k$  and 1 are approached. In isolated airfoil theory the loading at the tips must vanish since no pressure differential can exist off the airfoil. However, in the present problem, since we have not allowed for the effects of any clearance between the blades and the walls, the hard-wall boundary conditions require instead that there be no radial pressure gradient there, so

$$\frac{\partial \Delta p}{\partial \sigma} = 0 \quad \sigma = k, 1 \quad (189)$$

This requirement can be satisfied easily by a power series, and is another advantage of using such an expansion in the radial coordinate. In fact, if one assumes an expansion with N unknown coefficients, two of these can be expressed as linear combinations of the remaining (N-2) using the two conditions embodied in Eq. (189). This allows one to represent the radial variations with a power series two orders higher than the number of unknown coefficients one is willing to include.

As for the chordwise variation, it is very doubtful that a simple power series expansion in  $x_0$  would be adequate. This is because of the need to represent the behavior near the blade leading and trailing edges, where  $\Delta p$  and/or  $\frac{\partial \Delta p}{\partial x_0}$  have singularities. Accordingly, an expansion which represents such behavior explicitly will likely prove necessary, i.e.

$$\Delta p(\sigma_0, x_0) = A_0(\sigma_0) \sqrt{\frac{1-x_0}{1+x_0}} + \sqrt{1-x_0^2} \sum_i A_i(\sigma_0) P_i(x_0) \quad (190)$$

where each of the  $A_i$  is a power series in  $\sigma_0$  as discussed above, and the  $P_i$  is a suitably chosen set of finite polynomials, each of order  $i$ . Such a representation automatically exhibits the appropriate  $(1 \pm x_0)^{\pm 1/2}$  behavior near the leading and trailing edges, respectively.<sup>53</sup> Unfortunately, it also requires the use of numerical integrations with respect to  $x_0$ . The efficiency and accuracy of these integrations can be affected by the form assumed for the set of polynomials  $P_i$ , and various alternatives discussed in Refs. 55 and 60 are being considered. Once the terms containing the singularity that



occurs at the coincidence of the source and field points has been isolated and the mathematical character of the nonsingular portion of the integrand has been established, a choice for the form of the  $P_i$  will be made and efforts to obtain numerical results will begin.

#### F. CONCLUDING REMARKS

A linearized direct lifting surface theory has been formulated for the compressible, three-dimensional flow through a rotor of specified geometry in an annular duct. In arriving at this formulation, the overall subject of the linearized analysis of three-dimensional compressor flows was reviewed in detail. This review was made necessary by difficulties encountered in early phases of the work. Initial attempts to derive the loading contribution to the flow field of a rotor by the superposition of pressure dipole solutions met with two problems. The solution for the rotor pressure field did not yield a net pressure rise between points far upstream and downstream of the rotor. Furthermore, it did not agree with the result obtained by Namba<sup>49</sup> in a similar investigation.

The error in the pressure rise was traced to the omission of a term in previous versions of the fundamental solution for a point source. The missing term in the source solution also led to an error in the dipole solution. When these singularity solutions were corrected and the result for the pressure field revised accordingly, then a nonvanishing pressure rise across the rotor was found which agreed with the vortex theory result obtained by Okurounmu and McCune.<sup>42</sup>

Both the thickness and loading contributions to the flow field of a rotor were rederived using the corrected singularity solutions. The implications of the additional term in the source solution to published reports on the thickness problem have been described. The solution for the loading problem has been applied to formulate a direct lifting surface theory. There are two remaining differences between our formulation and that given by Namba.<sup>49</sup> First of all, there is the difference which results because the additional

term we found to be required in the dipole solution is not present in his. Secondly, our formulation does not contain his scale factor, a function of radius which modifies the dipole strength. We have concluded that this factor should not be included on the basis of several checks made on our analysis. Both the thickness and loading contributions to the rotor flow field have been shown to satisfy the global conservation of mass and of the axial components of linear and angular momentum. In addition, the velocity components have been shown to display the correct behavior at the blade surfaces and, in the loading case, across the trailing vortex wakes.

Progress has been made toward obtaining numerical solutions of the integral equation for the unknown blade loading. A kernel function method has been chosen as the best approach; the loading is expanded in a double series of suitable functions in the chordwise and spanwise variables, the coefficients in which are unknown. The expected loading behavior near the blade leading and trailing edges is ensured by the inclusion of appropriate factors outside the double sum. The choice of the form of the expansion functions used to represent the axial and radial variations is deferred until the singularities in the integral equation have been isolated. These singularities occur in the kernel function when the source and field points coincide. It is felt that the same techniques used to isolate the discontinuities in the pressure and velocity fields can be used to determine the nature of these singularities, and work along these lines has begun. The isolation of these singularities should accelerate the rate of convergence of the series in the remaining portions of the integrand, and therefore, facilitate numerical evaluation of the solution.

SECTION V  
SUMMARY AND CONCLUSIONS

A theoretical and experimental investigation of discrete-tone rotor-stator interaction noise, and the development of a three-dimensional lifting surface theory for a rotor have been presented. In the experimental part of the program, the sound pressure levels produced on the outer duct wall of the annular cascade facility were measured for a rotor-stator pair. The microphone probe was located in the far field upstream of the blade rows and data were taken for two stator stagger angle settings. In both sets of data the rotor speed was varied continuously up to about 1450 rpm. A pure tone signal was observed above 1100 rpm which was identified as the fourth-harmonic of blade passage frequency. For one of the stator settings, some additional data were obtained on the fifth harmonic at about 600 rpm. Lower harmonics could not be excited at the rotor speeds attainable in the facility at the time of these experiments.

A limited amount of experimental data were taken on the time varying pressure signal at several chordwise locations adjacent to the blade tips of an isolated rotor. These data were taken in an attempt to obtain information on the loading at the blade tips with which to compare lifting surface calculations. However, the data appear to contain tip clearance effects which are not included in the theory and would complicate such an eventual comparison.

An approximate model has been developed to predict the discrete-tone noise produced by the interaction of a rotor and a stator. In this analysis the aerodynamic and acoustic aspects of the problem are treated separately. The sound pressure levels in the duct and total radiated power at the harmonics of blade passage frequency are computed in terms of the propagating duct acoustic modes. The amplitudes of these modes are related to the blade row parameters through an approximate two-dimensional representation of the unsteady blade forces. The main advance over previous approximate treatments of rotor-stator noise is the incorporation of an aerodynamic model that accounts for compressibility effects.

Sample calculations have been presented for sound pressure levels and total radiated power over a wide range of subsonic Mach numbers and comparisons of the mode amplitudes were made with those predicted by an incompressible model. In addition, theoretical predictions were made of the discrete-tone noise to be expected in the acoustic experiments. The calculated sound pressure levels were significantly lower than the measured values. Evidence has been presented showing that the sound pressure levels at the higher harmonics of blade passage frequency are sensitive to the uncertainties in the data for wake mean velocity profiles. This should not be true for the fundamental and the lower harmonics and so, if the inaccuracies in predicting the sound pressure levels of the fourth harmonic are due to an inadequate wake model, then better agreement with experiment should result for lower harmonics. The annular cascade facility has been repowered so that higher rotor speeds are now available. Further acoustic experiments are planned in order to obtain data on the lower harmonics.

Finally, a direct lifting surface theory has been formulated for the compressible, three-dimensional flow through an isolated rotor. A pressure dipole representation of the blade row was used to derive the integral equation relating the blade loading to a specified blade shape. During this development, the omission of a term in previously published versions of the fundamental source and pressure dipole solutions was found and corrected. As a result, a general review of the linearized analysis of three-dimensional compressor flows was presented. Both the thickness and loading contributions to the flow field of a rotor were considered.

Work was begun on solving the governing integral equation using numerical techniques analogous to those employed successfully for isolated wings and cascades. A kernel function approach has been chosen which incorporates the expected behavior of the loading at the blade leading and trailing edges and at the duct walls. At present, the singularity in the kernel function is being isolated and, once this is completed, programming and numerical evaluations of the solution will begin.

APPENDIX A

DEFINITION OF RADIAL EIGENFUNCTIONS

This appendix summarizes the definition and properties of the orthogonal normal radial eigenfunctions,  $R_{nm}$ . As used in Section III

$$R_{nm}(v_{nm}\sigma) \equiv \left[ J_n(v_{nm}\sigma) - \frac{J_n'(v_{nm})}{Y_n'(v_{nm})} Y_n(v_{nm}\sigma) \right] / N_{nm}$$

$$\equiv Z_{nm}(v_{nm}\sigma) / N_{nm}$$

where  $J_n$  and  $Y_n$  are the Bessel functions of the first and second kind, of order  $n$ . The normalization factor  $N_{nm}$  is chosen such that

$$\int_{\hbar}^1 \sigma R_{nk}(v_{nk}\sigma) R_{nm}(v_{nm}\sigma) d\sigma = \delta_{km}$$

where  $\delta_{km}$  is the Kronecker delta. This requires

$$N_{nm} = \frac{1}{\sqrt{2}} \left\{ Z_{nm}^2(v_{nm}) \left[ 1 - \left( \frac{n}{v_{nm}} \right)^2 \right] - Z_{nm}^2(v_{nm}\hbar) \left[ \hbar^2 - \left( \frac{n}{v_{nm}\hbar} \right)^2 \right] \right\}^{1/2}$$

The set of eigenvalues  $v_{nm}$  corresponding to each function are solutions of

$$\frac{J_n'(v_{nm})}{Y_n'(v_{nm})} = \frac{J_n'(v_{nm}\hbar)}{Y_n'(v_{nm}\hbar)}$$

which insures that Equation (8) will be satisfied. The zeroth eigenvalue,  $v_{n0}$  is zero so that all the  $R_{n0}$  are trivially zero, save for the case  $n=0$ . Then

$$v_{00} = 0 \quad R_{00} = \frac{1}{N_{00}} = \left( \frac{2}{1-\hbar^2} \right)^{1/2}$$

The set of functions  $R_{nm}$  is complete for any  $n$ , so that a function can be represented on the interval  $\hbar$  to 1 by the series

$$f(\sigma) = \sum_{m=0}^{\infty} C_{nm} R_{nm}(v_{nm}\sigma)$$

where

$$C_{nm} = \int_{\hbar}^1 \sigma f(\sigma) R_{nm}(v_{nm}\sigma) d\sigma$$

and  $n$  can be chosen for convenience. These functions are discussed at more length in the papers by McCune<sup>28</sup> and Tyler and Sofrin.<sup>4</sup> (Note that in the lifting surface theory of Section IV, a somewhat different notation is used. There,  $k$  rather than  $m$ , is used as the radial mode index, and the eigenvalues are referred to as  $K_{nk}$  rather than  $\nu_{nm}$ .)

APPENDIX B  
EXPRESSIONS FOR ROTOR-STATOR INTERACTION FORCES

This appendix quotes the results of Osborne's analysis of the unsteady compressible interactions within a stator-rotor pair,<sup>24</sup> as shown in Figure 12a. Some typographical errors appearing in Reference 24, and checked with its author, are also corrected. The notation used here is that of Osborne, except where otherwise noted. Note in particular that "l" was used for the load harmonic index, in place of his "m", to keep consistent with the main text.

a) Rotor Unsteady Lift Resulting from Passage of Steady Stator Loads

$$X_l = L_R \frac{\Gamma_s}{\Gamma_R \beta_R} \left[ 1 - (1 - \beta_s) e^{-i\chi} \cos \chi \right] G_l K_L (l \Omega_R, l \beta_R, M_R)$$

$$G_l = -\pi \sigma_R \left( \frac{d_R}{d_s} \right) e^{i\alpha_R} D_s H_l \\ \cdot e \left\{ -\pi l \sigma_R \left( \frac{d_R}{d_s} \right) \left[ \frac{b}{c_R} (1 + i \tan \alpha_R - i \frac{U}{V_s \cos \alpha_s}) A - i \frac{U}{V_R} \right] \right\}$$

$${}_s H_l = J_0(\psi) + \sum_{n=1}^{\infty} (-1)^n \frac{{}_s A_{n-1} - {}_s A_{n+1}}{{}_s A_0 + {}_s A_1} J_n(\psi)$$

$$\psi = i\pi l \sigma_s e^{-i\alpha_s} A \quad \chi = \alpha_s + \alpha_R$$

$$A = \left[ 1 - (1 - \beta_s) e^{i\alpha_s} \cos \alpha_s \right] / (1 - M_s^2 \cos^2 \alpha_s)$$

$$B = 1 - i(1 - \beta_s) e^{-i\chi} \sin \chi, \quad C = AB, \quad D = A/\beta_s$$

$$\Gamma_s = 2\pi c_s V_s ({}_s A_0 + {}_s A_1) \quad L_s = \rho V_s \Gamma_s$$

$$\Gamma_R = 2\pi c_R V_R ({}_R A_0 + {}_R A_1) \quad L_R = \rho V_R \Gamma_R$$

$$\Omega_R = \frac{\omega_R}{\beta_R^2} \quad \tau_R = M_R^2 \Omega_R \quad \omega_R = \frac{V_R C_R}{V_R}$$

$$\mu_R = \frac{-2\pi l V_R e^{i\alpha_R} C}{d_s} \quad \delta_R = \tau_R + \frac{\mu_R C_R}{V_R}$$

$$\sigma_R = \frac{2C_R}{d_R} \quad \sigma_s = \frac{2C_s}{d_s}$$

$$M_R = \frac{V_R}{a_0} \quad M_s = \frac{V_s}{a_0} \quad \beta_R = (1 - M_R^2)^{1/2} \quad \beta_s = (1 - M_s^2)^{1/2}$$

The  ${}_s A_n$  are the coefficients in the Glauert expansion of the stator blade shape. That is, if  ${}_s Y(x_s)$  describes the stator blade shape, then

$${}_s Y'(x_s) = -{}_s A_0 - 2 \sum_{n=1}^{\infty} A_n \cos n\theta$$

where

$$x_s = c_s \cos \theta \quad c_s \leq x_s \leq c_s$$

An analogous expression defines the  ${}_R A_n$ . The quantities  $K_L$  and  $\tau_R$  will be discussed further below.

b) Stator Unsteady Lift Resulting from Passage of Steady Rotor Loads

$$Z_L = L_s \frac{\Gamma_R}{\Gamma_s \beta_s} [1 - (1 - \beta_R) e^{i\chi} \cos \chi] G_L K_L(l\Omega_s, l\delta_s, M_s)$$

$$G_L = \pi \sigma_s \left(\frac{d_s}{d_R}\right) e^{-i\alpha_s} J_R H_L e^{\left\{-\pi l \sigma_R \left[\frac{b}{C_R} (1 + i \tan \alpha_R - i \frac{U}{V_s \cos \alpha_s}) K - i \frac{U}{V_R}\right]\right\}}$$

$${}_R H_L = J_0(\psi) + \sum_{n=1}^{\infty} (-i)^n \frac{{}_R A_{n+1} - {}_R A_{n-1}}{{}_R A_0 + {}_R A_1} J_n(\psi)$$

$$\psi = -i \pi l \sigma_R e^{i\alpha_R} E$$



$$E = [1 - (1 - \beta_R) e^{-i\alpha_R} \cos \alpha_R] / (1 - M_R^2 \cos^2 \alpha_R)$$

$$F = 1 + i(1 - \beta_R) e^{i\chi} \sin \chi$$

$$G = 1 + i(1 - \beta_R) e^{i\alpha_s} \sin \chi$$

$$K = EG \quad I = EF \quad J = E/\beta_R$$

$$\Omega_s = \frac{\omega_s}{\beta_s^2} \quad \tau_s = M_s^2 \Omega_s \quad \omega_s = \frac{V_s C_s}{V_s}$$

$$\mu_s = \frac{2\pi i V_s e^{-i\alpha_s} I}{\alpha_R} \quad \delta_s = \tau_s + \frac{\mu_s C_s}{V_s}$$

The function  $K_L(\Omega, \delta, M)$  represents the airfoil response to a generalized Kemp-type upwash gust. In Equation (6) of Reference 24, it was given as the sum of an infinite series of products of Bessel functions. Kemp<sup>38</sup> later showed that the series could be summed analytically, and gave the closed form expression:

$$K_L(\Omega, \delta, M) = J(\delta) [C(\Omega) J(\tau) + i J_1(\tau)] + i \left[ \frac{\omega}{\delta - \tau} \right] [J_0(\tau) J_1(\delta) - J_1(\tau) J_0(\delta)]$$

with either  $R$  or  $s$  subscripts, as appropriate above. Here

$$J(x) \equiv J_0(x) - i J_1(x)$$

and  $C(x)$  is Theodorsen's function,

$$C(x) = \frac{K_1(ix)}{K_0(ix) + K_1(ix)}$$

where  $K_0$  and  $K_1$  are modified Bessel functions of the second kind with imaginary arguments. This is the form for  $K_L$  used in the present study; using it, Osborne's original numerical results were reproduced to within the reading accuracy of his curves.

Furthermore, it has recently been noted<sup>59</sup> that Osborne's original asymptotic aerodynamic analysis does not appear to be consistent to first order in his small parameter  $M\omega/2\pi\beta^2$ , as claimed.<sup>27</sup> After re-doing the analysis starting from the integral equation for blade loading in unsteady flow, it was found that all of Osborne's expressions remained valid provided that  $\tau$  was replaced by  $\tau'$ ,<sup>29</sup> where

$$\tau' = [M^2 - f(M)] \Omega$$

$$f(M) = \beta \ln(1 + \beta) + (1 - \beta) \ln M - \ln 2; \quad f(0) = 0$$

again with either  $R$  or  $S$  subscripts. Accordingly, this revised definition of  $\tau$  was used in both potential interactions above for the present study. Note that this in no way alters the fact that the equations still reduce to those of Kemp and Sears<sup>2</sup> at incompressible speeds.

c) Rotor Unsteady Lift Resulting from Passage of Stator Viscous Wakes

$$Y_L = \frac{\rho V_R^2 C_R}{\beta_R} G_L T(l\tau_R, l\Omega_R)$$

$$G_L = 4\pi \frac{V_S}{V_R} \frac{2.42 C_D^{1/2} \sin \chi}{\left(\frac{Z}{C_S} + 0.3\right)} \frac{0.63 \sigma_S}{\cos \alpha_S} \left(\frac{C_D}{2}\right)^{1/2} \left(\frac{Z}{C_S}\right)^{1/2} e^{i l \omega_R} e^{-\left(\frac{0.68 \sigma_S l}{\cos \alpha_S}\right)^2 \frac{\pi C_D Z}{2 C_S}}$$

where

$$\frac{Z}{C_S} = \left(\frac{b}{C_S} \sec \alpha_S + \frac{Z_R}{C_S} \frac{V_S}{V_R}\right) - 0.7$$

and  $Z_R$  is some chosen value of  $x_R$  between  $-C_R$  and  $+C_R$ , usually the quarter-chord point. The other quantities are given in a) above. As originally derived by Osborne,  $T$ , which represents the airfoil response to a sinusoidal gust, was given as

$$T(l\tau_R, l\Omega_R) = J(l\tau_R) S(l\Omega_R)$$

where  $J(x)$  is defined above and  $S(x)$  is Sears' original incompressible response function:

$$S(x) = \frac{1}{i x [K_0(i x) + K_1(i x)]}$$

However, Amiet<sup>40</sup> has shown that if this expression is multiplied by the phase factor  $e^{if(M)\Omega_R}$ , the result more closely approximates numerical solutions for the loading. Thus, in the present study

$$T(l\tau_R, l\Omega_R) = J(l\tau_R) S(l\Omega_R) e^{if(M)\Omega_R}$$

where  $f(M)$  is defined in b) above. Note, however, that use of Osborne's original  $\tau$ , and not  $\tau'$ , is retained in this expression; also, the magnitude remains unaffected. Again, the above results reduce to those of Kemp and Sears in the limit  $M = 0$ . (The factor  $e^{i l \omega_R}$  in  $G_l$  is a phase shift reflecting Osborne's alternate choice of the blade row positions at the instant  $t = 0$ ).

Having quoted the aerodynamic expressions appropriate to a stator-rotor pair shown in Figure 12a, we now consider how these can be applied to the rotor-stator geometry of Figure 12b. As noted by Osborne,<sup>24</sup> the only thing in his two-dimensional model which distinguishes the rotor from the stator is that by definition the rotor is the blade row which moves with respect to the duct. Since the row stagger angles, blade profiles, etc. all appear as input parameters in Osborne's analysis, these are readily switched. But the fact that it is now the upstream blade row which is moving is not consistent with his model. This is easily remedied by a Galilean transformation to coordinates moving with the rotor, as in Figure 12c, so that the stator now appears in motion. Noting the sense in which  $\alpha_R$  and  $\alpha_S$  are defined positive in Figure 12a, a comparison of Figure 12c with Figure 12a suggests that the interaction forces in the reverse geometry of Figure 12b are directly related to those of Figure 12a if one simply substitutes

$$\alpha_R = -\alpha_S \quad \alpha_S = -\alpha_R \quad U = -U$$

in the above equations and reverses the subscripts  $R$  and  $S$  wherever appropriate. At first glance, the reader might be bothered that we appear to be computing

the forces in the wrong coordinate frame, so to speak, i.e., with the stator moving and the rotor stationary. But we are only concerned with the force magnitudes and their relative phasing between blades, which, of course, remain the same provided we always measure in a Galilean frame. In using these forces in the subsequent acoustic calculations, we revert back to duct-fixed coordinates [see Equations (13a-c) in the main text] .

APPENDIX C  
 MASS AND MOMENTUM BALANCES FOR SINGULARITY AND  
 ROTOR FLOW FIELDS

Tests performed on the source, dipole, and rotor flow field solutions derived in Section IV to determine if they satisfy global mass and momentum conservation are described here. The control volume employed is bounded by the duct walls and the annular areas perpendicular to the duct axis at upstream and downstream infinity (see Figure 19). Since this control volume rotates with angular velocity  $\omega$  (in the negative  $\theta$ -direction), the conservation laws for a noninertial reference frame must be used. The appropriate integral forms of the equations for conservation of mass, momentum, and angular momentum for such a control volume have been taken from Ref. 61. Then, these equations have been linearized so that they are expressed in terms of the undisturbed flow properties  $\rho_\infty$ ,  $U$ , and  $\omega r$ , and the perturbation quantities  $p$ ,  $\rho$ ,  $v_r$ ,  $v_\theta$ , and  $v_z$ . These equations were specialized further to account for the fact that all the flow field solutions decay at upstream infinity and satisfy the boundary condition of no flow through the duct walls. Attention has been confined to the expressions for mass conservation and to the axial components of the momentum and angular momentum balances. Under the present set of assumptions, these expressions become

$$\dot{m} = \int_{r_H}^{r_T} \int_0^{2\pi} (\rho_\infty v_z + \rho u) \Big|_{z \rightarrow \infty} r dr d\theta \quad (C-1)$$

$$\dot{F}_z = \int_{r_H}^{r_T} \int_0^{2\pi} (2\rho_\infty U v_z + \rho U^2 + p) \Big|_{z \rightarrow \infty} r dr d\theta \quad (C-2)$$

$$\begin{aligned} \dot{J}_z = & -2 \int_{-\infty}^{\infty} \int_{r_H}^{r_T} \int_0^{2\pi} \rho_\infty (\omega r v_r) r dr d\theta dz \quad (C-3) \\ & + \int_{r_H}^{r_T} \int_0^{2\pi} [\rho_\infty U r v_\theta + \omega r^2 (\rho_\infty v_z + \rho U)] \Big|_{z \rightarrow \infty} r dr d\theta \end{aligned}$$

where  $\dot{m}$  denotes the rate of introduction of mass into the control volume while  $F_z$  and  $J_z$  are the axial components of the net force and torque on the fluid. In the discussion which follows, the flow field solutions obtained for a mass source, pressure dipole, rotor blade thickness distribution, and rotor loading distribution are shown in each case to give the values of  $\dot{m}$ ,  $F_z$ , and  $J_z$  required to satisfy these conservation laws.

### 1. Mass Source

The flow field due to a point source which is located at the point  $(r_0, \theta_0, z_0)$  was given in Section IV-B. The mass addition rate into the control volume,  $\dot{m}$ , due to this source is just the following volume integral:

$$\dot{m} = \int_{-\infty}^{\infty} \int_0^{2\pi} \int_{r_H}^{r_T} \rho_{\infty} Q \frac{\delta(r-r_0) \delta(\theta-\theta_0) \delta(z-z_0)}{r_0} r dr d\theta dz = \rho_{\infty} Q \quad (C-4)$$

This rate of introduction of mass must be balanced by the mass flow out of the control volume, as expressed by Eq. (C-1). Using Eq. (54) to eliminate  $\rho$  in favor of  $p$ , that expression for  $\dot{m}$  becomes

$$\dot{m} = \int_{r_H}^{r_T} \int_0^{2\pi} \left( \rho_{\infty} v_z + \frac{p}{a_{\infty}^2} U \right) \Big|_{z=-\infty} r d\theta dr \quad (C-5)$$

From Eqs. (83b) and (83c), the limiting values of  $v_z$  and  $p$  for  $z \rightarrow \infty$  are found to be

$$\lim_{z \rightarrow \infty} (v_z)_S = \frac{Q}{2\pi \beta^2 r_T^2} \left( \frac{z}{1-k^2} \right) \quad (C-6a)$$

$$\lim_{z \rightarrow \infty} p_S = -\rho_{\infty} U \frac{Q}{2\pi \beta^2 r_T^2} \left( \frac{z}{1-k^2} \right) \quad (C-6b)$$

Substituting these results into Eq. (C-5), it is easy to show that the integration yields  $\dot{m} = \rho_\infty Q$  and so the source solution satisfies global conservation of mass.

The presence of a source in a mean flow results in a force on the fluid. To first order, the force due to a point source of strength  $Q$  in an undisturbed stream with velocity  $\bar{U}_R$  is

$$\vec{F} = \rho_\infty \int_{-\infty}^{\infty} \int_0^{2\pi} \int_{r_H}^{r_T} \bar{U}_R Q \frac{\delta(r-r_0)\delta(\theta-\theta_0)\delta(z-z_0)}{r_0} r dr d\theta dz \quad (C-7)$$

The axial component of this force,  $F_z$ , is  $\rho_\infty U Q$ . This force on the fluid must be balanced by the momentum flux and the pressure forces at the surfaces of the control volume. For the control volume being considered here, this balance is expressed by Eq. (C-2). Again eliminating  $\rho$  in terms of  $\phi$ , that equation becomes

$$F_z = \int_{r_H}^{r_T} \int_0^{2\pi} \left[ 2\rho_\infty U v_z + (1+M^2)\phi \right] \Big|_{z=-\infty}^{z=\infty} r d\theta dr \quad (C-8)$$

If the results for  $(v_z)_s$  and  $\phi_s$  given in Eq. (C-6) are substituted in Eq. (C-8), it is straightforward to show that this expression reduces to  $F_z = \rho_\infty U Q$ , and hence the source solution also satisfies the axial component of global momentum conservation.

In the present application, the presence of a source also results in a torque on the fluid because the undisturbed stream has a rotational component. Since the  $\theta$ -component of the undisturbed velocity is  $\omega r$  the axial component of the torque on the fluid is

$$J_z = \rho_\infty \int_{-\infty}^{\infty} \int_0^{2\pi} \int_{r_H}^{r_T} (\omega r) r Q \frac{\delta(r-r_0)\delta(\theta-\theta_0)\delta(z-z_0)}{r_0} r dr d\theta dz = \rho_\infty \omega r_0^2 Q \quad (C-9)$$

Conservation of angular momentum requires that this also be the result of the integrations over the source solution indicated in Eq. (C-3). First we write Eq. (C-3) in the form

$$\mathcal{J}_z = -2\mathcal{J}_1 + \mathcal{J}_2 \quad (\text{C-10})$$

where  $\mathcal{J}_1$  is the volume integral and  $\mathcal{J}_2$  is the surface integral. From Eq. (83a) it can be seen that  $(v_\theta)_s$  decays for  $z \rightarrow \infty$ . When Eq. (C-6) is used for the limiting values of  $(v_z)_s$  and  $p_s$ , the surface integral becomes similar to those already evaluated in the  $\mathcal{M}$  and  $\mathcal{F}_z$  expressions. The result for  $\mathcal{J}_2$  is

$$\mathcal{J}_2 = \rho_\infty \omega Q \frac{r_T^2 + r_H^2}{2} \quad (\text{C-11})$$

Obtaining  $(v_r)_s$  by taking the derivative with respect to  $r$  of  $\Phi_s$  in Eq. (81), the following intermediate result needed in  $\mathcal{J}_1$  can be obtained.

$$\int_{-\infty}^{\infty} \int_0^{2\pi} (v_r)_s \alpha \theta \alpha z = - \frac{Q}{\beta^2 r_T^2} \sum_{k=1}^{\infty} \frac{R_{0k}(\sigma_0)}{\left(\frac{\omega \lambda_{0k}}{U}\right)^2} \frac{dR_{0k}(\sigma)}{dr} \quad (\text{C-12})$$

Also using the definition of  $\lambda_{0k}$  from Eq. (71), the expression for  $\mathcal{J}_1$  at this stage is

$$\mathcal{J}_1 = - \rho_\infty \omega Q \sum_{k=1}^{\infty} \frac{R_{0k}(\sigma_0)}{K_{0k}^2} \int_{r_H}^{r_T} \frac{dR_{0k}(\sigma)}{dr} r^2 dr \quad (\text{C-13})$$

Next an integration by parts is carried out and Eqs. (70) and (74) are used in the result so that  $\mathcal{J}_1$  becomes

$$\mathcal{J}_1 = - \rho_\infty \omega Q \sum_{k=1}^{\infty} R_{0k}(\sigma_0) \int_k^{r_T} \frac{r^2}{2} R_{0k}(\sigma) \sigma d\sigma \quad (\text{C-14})$$

The summation in (C-14), but for the  $k=0$  term, is the Fourier-Bessel expansion for  $r_0^2/2$  in terms of the zeroth-order eigenfunctions,  $R_{0k}(\sigma_0)$ . The



final result for  $\mathcal{J}$ , is

$$\mathcal{J} = -\frac{\rho_\infty \omega r_o^2 Q}{2} + \frac{\rho_\infty \omega Q}{4} (r_r^2 + r_n^2) \quad (C-15)$$

Using Eqs. (C-11) and (C-15) in Eq. (C-10) yields

$$\mathcal{J}_z = \rho_\infty \omega r_o^2 Q \quad (C-16)$$

which is the result required for the source solution to satisfy conservation of angular momentum (see Eq. (C-9)).

## 2. Pressure Dipole

The pressure dipole singularity should result in a net force on the fluid, but it should not introduce any mass. Hence, in this case the rate of mass addition to the control volume,  $\dot{m}$ , must be zero. Before substituting the results for the dipole flow field into Eq. (C-1) to check for conservation of mass, these results are rewritten in a somewhat different form. The integral of the dipole pressure field,  $p_D$ , along the stream direction as given in Eq. (100a) is labeled  $I_D(z)$ . Then, from Eqs. (99) and (100), the normal velocity component is

$$(v_n)_D = -\frac{1}{\rho_\infty U} \frac{\partial I_D(z)}{\partial n} - \frac{D}{\rho_\infty U} \frac{\delta(r-r_o) \delta(\xi-\xi_o)}{r_o} H(z-z_o) \quad (C-17)$$

Now if  $\frac{\partial}{\partial n}$  is written in terms of  $\frac{\partial}{\partial \xi} \xi_{,r}$  and  $\frac{\partial}{\partial \xi} z_{,r}$ , as in Eq. (115), and it is recalled that  $\xi$  is held constant in the integration along streamlines,

$(v_n)_D$  becomes

$$(v_n)_D = \frac{p_D}{\rho_\infty U} \sin \psi - \frac{1}{\rho_\infty U r} \sqrt{1 + \left(\frac{\omega r}{U}\right)^2} \frac{\partial I_D}{\partial \xi} - \frac{D}{\rho_\infty U} \frac{\delta(r-r_o) \delta(\xi-\xi_o)}{r_o} H(z-z_o) \quad (C-18)$$

Using Eq. (53) to relate  $(v_\xi)_D$  to  $p_D$  and then using Eq. (10ib) to obtain

$(v_z)_D$  from  $(v_n)_D$  and  $(v_\xi)_D$ ,

$$(v_z)_D = -\frac{p_D}{\rho_\infty U} + \frac{\omega}{\rho_\infty U^2} \frac{\partial I_D}{\partial \xi} + \frac{D \sin \psi}{\rho_\infty U} \frac{\delta(r-r_o) \delta(\xi-\xi_o)}{r_o} H(z-z_o) \quad (C-19)$$

In order to evaluate the integral in Eq. (C-1) we need the limiting forms of  $p_0$  and  $\frac{\partial I_0}{\partial \xi}$  for  $z \rightarrow \infty$ . These quantities are found to be

$$\lim_{z \rightarrow \infty} p_0 = \frac{D}{2\pi \beta^2 r_T^2} \sin \psi_0 \left( \frac{z}{1-k^2} \right) \quad (C-20a)$$

$$\lim_{z \rightarrow \infty} \frac{\omega}{U} \frac{\partial I_0}{\partial \xi} = - \frac{D}{2\pi \beta^2 r_T^2 \sin \psi_0} \sum_{n=-\infty}^{\infty} \sum_{k=1}^{\infty} R_{n*}(\sigma_0) R_{n*}(\sigma) e^{in(\xi-\xi_0)} \left[ \frac{n^2}{\beta^2 + \lambda_{n*}^2} \right] \quad (C-20b)$$

Upon substituting for  $(v_z)_0$  and  $p_0$  in Eq. (C-1), the integral expression for  $\mathcal{M}$  is written

$$\mathcal{M} = \mathcal{I}_3 + \mathcal{I}_4 + \mathcal{I}_5 \quad (C-21)$$

where

$$\mathcal{I}_3 = - \frac{\beta^2}{U} \int_{r_H}^{r_r} \int_0^{2\pi} p_0 \Big|_{z \rightarrow \infty} r d\theta dr \quad (C-22)$$

$$\mathcal{I}_4 = \frac{1}{U} \int_{r_H}^{r_r} \int_0^{2\pi} \left[ \frac{\omega}{U} \frac{\partial I_0(z)}{\partial \xi} \right]_{z \rightarrow \infty} r d\theta dr \quad (C-23)$$

$$\mathcal{I}_5 = \frac{D}{U} \int_{r_H}^{r_r} \int_0^{2\pi} \sin \psi \frac{\delta(r-r_0) \delta(\xi-\xi_0)}{r_0} r d\theta dr \quad (C-24)$$

Now, using Eq. (C-20a) in Eq. (C-22),  $\mathcal{I}_3$  is found to be

$$\mathcal{I}_3 = - \frac{D \sin \psi_0}{U} \quad (C-25)$$

As a result of the  $\theta$ -integration,  $\mathcal{I}_4$  vanishes because the  $n=0$  term is absent. Also, since for fixed  $z$ ,  $d\theta = d\xi$ , we have

$$\mathcal{I}_5 = \frac{D \sin \psi_0}{U} \quad (C-26)$$

When the results for  $\mathcal{J}_3$ ,  $\mathcal{J}_4$ , and  $\mathcal{J}_5$  are added together,  $\mathcal{M}$  vanishes as it should.

As discussed in Section IV-B, the pressure dipole exerts a force of magnitude  $D$  in the negative  $\vec{n}$  direction (see Figure 20). The  $z$ -component of this force,  $F_z$ , is  $D \sin \psi_0$ . The global momentum balance as stated in Eq. (C-2) provides a check on whether the dipole flow field is consistent with this force on the fluid. Eq. (C-2) can be expressed in terms of the integrals  $\mathcal{J}_3$ ,  $\mathcal{J}_4$ , and  $\mathcal{J}_5$  defined above.

$$F_z = U \mathcal{J}_3 + 2U \mathcal{J}_4 + 2U \mathcal{J}_5 \quad (\text{C-27})$$

Using the results in Eqs. (C-25) and (C-26), and the fact that  $\mathcal{J}_4$  vanishes, the dipole flow field is seen to satisfy momentum conservation.

The force which the dipole exerts also results in a torque acting on the fluid. The axial component of this torque,  $J_z$ , is  $-Dr_0 \cos \psi_0$ . In order for the dipole flow field to conserve angular momentum, this also must be the value of the integrals on the right-hand side of Eq. (C-3). In order to simplify the description of these integrations, Eq. (C-3) is written

$$J_z = -2\mathcal{J}_6 + \mathcal{J}_7 + \mathcal{J}_8 \quad (\text{C-28})$$

where

$$\mathcal{J}_6 = \rho_\infty \omega \int_{-\infty}^{\infty} \int_0^{2\pi} \int_{r_H}^{r_T} (v_r)_0 r^2 dr d\theta dz \quad (\text{C-29})$$

$$\mathcal{J}_7 = \rho_\infty U \int_{r_H}^{r_T} \int_0^{2\pi} (v_\theta)_0 \Big|_{z \rightarrow \infty} r^2 d\theta dr \quad (\text{C-30})$$

$$\mathcal{J}_8 = \omega \int_{r_H}^{r_T} \int_0^{2\pi} r^2 [\rho_\infty (v_z)_0 + \rho_0 U] \Big|_{z \rightarrow \infty} r d\theta dr \quad (\text{C-31})$$

The radial velocity component for the dipole field is given by Eqs. (98) and (100a). If the  $\theta$  and  $z$  integrations in  $\mathcal{J}_6$  are carried out, the following result is obtained.

$$\int_{-\infty}^{\infty} \int_0^{2\pi} (v_r)_0 d\theta dz = \frac{D \sin \psi_0}{\rho_m U \beta^2 r^2} \sum_{k=1}^{\infty} \frac{R_{0k}(\sigma_0)}{\left(\frac{\omega \lambda_0}{U}\right)^2} \frac{dR_{0k}(\sigma)}{dr} \quad (\text{C-32})$$

Using Eq. (C-52) in Eq. (C-29) and substituting for  $\lambda_{0k}$  from Eq. (71), the following intermediate expression for  $\mathcal{J}_6$  results.

$$\mathcal{J}_6 = \frac{\omega}{U} D \sin \psi_0 \int_{r_H}^{r_0} \sum_{k=1}^{\infty} \frac{R_{0k}(\sigma_0)}{K_{0k}^2} \frac{dR_{0k}(\sigma)}{dr} r^2 dr \quad (\text{C-33})$$

This same integral was evaluated in the angular momentum balance for the mass source, see Eqs. (C-13) through (C-15). Using that result

$$\mathcal{J}_6 = \frac{\omega}{U} D \sin \psi_0 \left(\frac{r_0^2}{2}\right) - \frac{\omega}{U} D \sin \psi_0 \frac{r_r^2 + r_H^2}{4} \quad (\text{C-34})$$

The evaluation of  $\mathcal{J}_7$  requires the result for  $(v_\theta)_0$ , which can be obtained from  $(v_s)_0$  and  $(v_n)_0$  by Eq. (101a). Using Eqs. (91), (53), and (C-18) in Eq. (101a),

$$(v_\theta)_0 = - \frac{1}{\rho_m U r} \frac{\partial I_D(z)}{\partial \xi} - \frac{D \cos \psi}{\rho_m U} \frac{\delta(r-r_0) \delta(\xi-\xi_0)}{r_0} H(z-z_0) \quad (\text{C-35})$$

The limit of  $\frac{\partial I_D}{\partial \xi}$  for  $z \rightarrow \infty$  is given by Eq. (C-20b) and, since the  $\theta$ -integration of this quantity vanishes,  $\mathcal{J}_7$  reduces to

$$\mathcal{J}_7 = -D r_0 \cos \psi_0 \quad (\text{C-36})$$

The integral  $J_8$  is similar to the integrals  $J_3$ ,  $J_4$ , and  $J_5$  done in connection with the mass balance. Substituting into Eq. (C-31) using Eqs. (54), (C-19), and (C-20)

$$J_8 = -\frac{\omega}{U} D \sin \psi_0 \left( \frac{r_T^2 + r_H^2}{2} \right) + \frac{\omega}{U} D \sin \psi_0 (r_0^2) \quad (C-37)$$

Collecting the results for  $J_6$ ,  $J_7$ , and  $J_8$  from Eqs. (C-34), (C-36), and (C-37) according to Eq. (C-28) leads to the result  $J_z = -D r_0 \cos \psi_0$ , and so the solution for the flow field of a pressure dipole also conserves angular momentum.

### 3. Rotor Blade Thickness

The flow field produced by the thickness of a rotor has been obtained by the superposition of source solutions. For closed blade surfaces, the net source strength must vanish. Hence, conservation of mass requires that there be no net introduction of mass into the control volume. It should be mentioned that blade shapes having flat-faced trailing edges are excluded from consideration. Blades having nonzero thickness at the trailing edge would require infinite source strength because of the discontinuity in surface slope.

In order to separate the rotor flow field into thickness and loading contributions, it has been assumed that the rotor is unloaded in the thickness problem. In Section IV-C-3, it was shown that the flow field solution displays the correct behavior of zero pressure difference across the blade surfaces. Consequently, there should be no net force or torque exerted on the fluid by the rotor, provided there is no blunt trailing edge which results in a base drag. However, as discussed in the previous paragraph such a blade shape is excluded from consideration because of the singularity in the source strength which results.

When the quantities  $\dot{m}$ ,  $\dot{T}_z$ , and  $J_z$  are computed from the mass and momentum balances expressed in Eqs. (C-1) through (C-3), all of these

quantities must vanish if the flow field produced by rotor thickness is to satisfy the global conservation laws. The evaluation of the expressions for  $\mathcal{M}$ ,  $\mathcal{F}_z$  and  $\mathcal{J}_z$  parallels that for the field of a mass source. The flow field results given in Section IV-C-2 are used to find the limiting values of  $v_\theta$ ,  $v_z$ , and  $p$ , which are then substituted in Eqs. (C-5), (C-8), and (C-10). The results obtained, in this case, are

$$m = \rho_\infty q_1 \quad (C-38a)$$

$$\mathcal{F}_z = \rho_\infty U q_1 \quad (C-38b)$$

$$\mathcal{J}_z = \rho_\infty \omega q_2 \quad (C-38c)$$

where

$$q_1 = B \int_{r_H}^{r_T} \int_0^{c_a} f(r_o) g(z_o) dz_o dr_o \quad (C-39a)$$

$$q_2 = B \int_{r_H}^{r_T} \int_0^{c_a} r_o^2 f(r_o) g(z_o) dz_o dr_o \quad (C-39b)$$

These integrals are rewritten by substituting the definition of  $f(r_o) g(z_o)$  in terms of the blade thickness distribution from Eq. (110).

$$q_1 = B \int_{r_H}^{r_T} \int_0^{c_a} \sqrt{1 + \left(\frac{\omega r_o}{U}\right)^2} U_R \frac{\partial t}{\partial S_o} dz_o dr_o \quad (C-40a)$$

$$q_2 = B \int_{r_H}^{r_T} \int_0^{c_a} r_o^2 \sqrt{1 + \left(\frac{\omega r_o}{U}\right)^2} U_R \frac{\partial t}{\partial S_o} dz_o dr_o \quad (C-40b)$$

But along the blade surfaces,  $U_R \frac{\partial}{\partial S_o} t(r_o, S_o)$  can be written as  $U \frac{\partial}{\partial z_o} t(r_o, z_o)$  and so the  $z_o$  integration which occurs in both  $q_1$  and  $q_2$  becomes

$$\int_0^{c_a} \frac{\partial}{\partial z_o} t(r_o, z_o) dz_o = t(r_o, c_a) - t(r_o, 0) \quad (C-41)$$

Now, for closed blade surfaces,  $\tau(r_o, 0) = \tau(r_o, C_a) = 0$  and so  $q_1 = q_2 = 0$ . Hence, from Eq. (C-38),  $\mathcal{M}$ ,  $\mathcal{F}_z$ , and  $J_z$  all vanish as required.

#### 4. Rotor Blade Loading

The results obtained for the flow field of a lifting rotor can be shown to satisfy the global conservation laws by following much the same steps as for the dipole field. Again there should be no net introduction of mass into the control volume, i.e.,  $\mathcal{M} = 0$ . The force which each rotor blade exerts on the fluid is given by Eq. (138). The axial component of the force of the whole rotor on the fluid is

$$\mathcal{F}_z = \frac{\omega B}{U} \int_0^{C_a} \int_{r_H}^{r_T} \Delta p(r, z) r dr dz \quad (C-42)$$

where Eq. (50b) has been used for the unit vector  $\vec{n}$  and Eq. (108) has been used to project an element of the blade surface area on the  $r, z$  plane. Similarly, if the  $\theta$ -component of the blade force at each radius is determined, the axial component of the torque exerted by the rotor is found to be

$$J_z = -B \int_0^{C_a} \int_{r_H}^{r_T} \Delta p(r, z) r dr dz \quad (C-43)$$

In order to evaluate the expressions for  $\mathcal{M}$ ,  $\mathcal{F}_z$ , and  $J_z$  derived from conservation of mass and momentum, Eqs. (C-1) to C-3), the rotor flow field variables appearing in these integrals are written in the same way as they were for the dipole field. First of all, the axial component of the mass flux is written in the form

$$\rho_\infty v_z + \rho U = -\beta^2 \frac{p}{U} + \frac{\omega}{U^2} \frac{\partial I}{\partial \xi} + \frac{\omega}{U^2} \sum_{j=0}^{B-1} \delta\left(\xi - \frac{2j\pi}{B}\right) \int_0^{C_a} \Delta p(r, z') H(z-z') dz' \quad (C-44)$$

where the expressions for  $p$  and  $I$  are given by Eqs. (134) and (144) respectively. The integrand in the relation for  $\mathcal{M}$  given in Eq. (C-1) contains the limit of this quantity for  $z \rightarrow \infty$ , and so the limiting values of  $p$  and  $\partial I / \partial z$  are needed.

$$\lim_{z \rightarrow \infty} p = \frac{\omega B}{2\pi\beta^2 U} \int_0^{c_a} \bar{\Delta p}(z_0) dz_0 \quad (C-45a)$$

$$\lim_{z \rightarrow \infty} \frac{\partial I}{\partial z} = -\frac{B}{2\pi\beta^2 r_T^2} \int_{r_H}^{r_T} \int_0^{c_a} \sum_{m=-\infty}^{\infty} \sum_{k=1}^{\infty} R_{m\theta k}(\sigma) R_{m\theta k}(\sigma_0) e^{im\theta} \cdot \left[ \frac{(mB)^2}{\left(\frac{mB}{\beta^2}\right)^2 + \lambda_{m\theta k}^2} \left[ \frac{1 + \left(\frac{\omega r_c}{U}\right)^2}{\left(\frac{\omega r_0}{U}\right)^2} \right] \right] \Delta p(r_0, z_0) r_0 dz_0 dr_0 \quad (C-45b)$$

where  $\bar{\Delta p}(r_0)$  is defined by Eq. (135).

By direct analogy with the dipole results, the expression for  $\mathcal{M}$  is rewritten as the sum of three integrals corresponding to integration over each of the three terms on the right-hand side of Eq. (C-44). These integrals are labeled  $\mathcal{I}_1$ ,  $\mathcal{I}_2$ , and  $\mathcal{I}_3$ , respectively. The first of these is

$$\mathcal{I}_3 = \int_{r_H}^{r_T} \int_0^{c_a} \left( -\beta^2 \frac{p}{U} \right) \Big|_{z \rightarrow \infty} r d\theta dr = -\frac{\omega B}{U^2} \int_0^{c_a} \int_{r_H}^{r_T} \Delta p(r_0, z_0) r_0 dr_0 dz_0 \quad (C-46)$$

where Eqs. (135) and (C-45a) have been used. The second integral vanishes as a consequence of the integration over  $\theta$ , i.e.,

$$\mathcal{I}_4 = \int_{r_H}^{r_T} \int_0^{2\pi} \left( \frac{\omega}{U^2} \frac{\partial I}{\partial z} \right) \Big|_{z \rightarrow \infty} r d\theta dr = 0 \quad (C-47)$$

The third integral is



$$\begin{aligned} \mathcal{L}_5 &= \int_{r_H}^{r_T} \int_0^{2\pi} \left[ \frac{\omega}{U^2} \sum_{j=0}^{B-1} \delta\left(\zeta - \frac{2j\pi}{B}\right) \int_0^{c_a} \Delta p(r, z') dz' \right] r d\theta dr \quad (C-48) \\ &= \frac{\omega B}{U^2} \int_0^{c_a} \int_{r_H}^{r_T} \Delta p(r, z') r dr dz' \end{aligned}$$

where again we have used the fact that at fixed  $z$ ,  $d\theta = d\zeta$ . If these three integrals are added together then the result  $\mathcal{M} = 0$  is obtained, confirming that the rotor flow field solution conserves mass.

As with the dipole field, the expression for the axial component of the blade force computed from the momentum balance, Eq. (C-2), can be expressed in terms of these same three integrals. If Eqs. (C-46) to (C-48) are combined according to Eq. (C-27), then the expression obtained for the axial component of the rotor force agrees with the result of direct integration of the blade forces given in Eq. (C-42). Hence, our results for the flow field produced by rotor loading also obey global momentum conservation.

The expression for the axial component of the torque on the fluid obtained from conservation of angular momentum, Eq. (C-3), can be written as in Eq. (C-28) except that now the integrals defined by Eqs. (C-29) to (C-31) contain the rotor rather than the dipole flow-field perturbations. When the expression for  $v_r$  given in Eq. (146) is used in Eq. (C-29), the integral  $\mathcal{L}_6$  becomes

$$\mathcal{L}_6 = - \frac{\omega^2 B}{U^2} \left( \frac{r_T^2 + r_H^2}{4} \right) d_1 + \frac{\omega^4 B}{2U^2} d_2 \quad (C-49)$$

where

$$d_1 \equiv \int_0^{c_a} \int_{r_H}^{r_T} \Delta p(r_o, z_o) r_o dr_o dz_o \quad (C-50a)$$

$$d_2 \equiv \int_0^{c_a} \int_{r_H}^{r_T} \Delta p(r_o, z_o) r_o^3 dr_o dz_o \quad (C-50b)$$

This result is obtained by carrying out the integrations over  $\theta$ ,  $z$ , and  $r$  in that order. The first two are straightforward; the integration over  $r$  uses the same technique required to evaluate the corresponding integral in the source and dipole cases.

The evaluation of  $J_7$  in Eq. (C-30) requires the  $\theta$  component of the perturbation velocity. This component of the rotor velocity field can be obtained from the normal and streamline components using Eq. (101a).

$$v_\theta = - \frac{1}{\rho_\infty U r} \frac{\partial I}{\partial \zeta} - \frac{1}{\rho_\infty U r} \sum_{j=0}^{B-1} \delta\left(z - \frac{2j\pi}{B}\right) \int_0^{c_a} \Delta\phi(r, z') H(z-z') dz' \quad (C-51)$$

Using the limiting form of  $\partial I / \partial \zeta$  from Eq. (C-45b), and noting that the integration of this quantity over  $\theta$  vanishes, we obtain

$$J_7 = -B d_1 \quad (C-52)$$

Finally, the integrand in  $J_8$  is just  $\omega r^2$  times the mass flux given in Eq. (C-44). The integrations over  $r$  and  $\theta$  are essentially the same as those done above for  $m$ , and the result is

$$J_8 = - \frac{\omega^2 B}{U^2} \frac{r_T^2 + r_H^2}{2} d_1 + \frac{\omega^2 B}{U^2} d_2 \quad (C-53)$$

Combining  $J_6$ ,  $J_7$ , and  $J_8$  according to Eq. (C-28) gives the same result for  $J_z$  as Eq. (C-43). Therefore, the solution for the flow field of a lifting rotor satisfies the torque and angular momentum balance. This completes the demonstration that the flow field results of Section IV obey the global conservation laws.

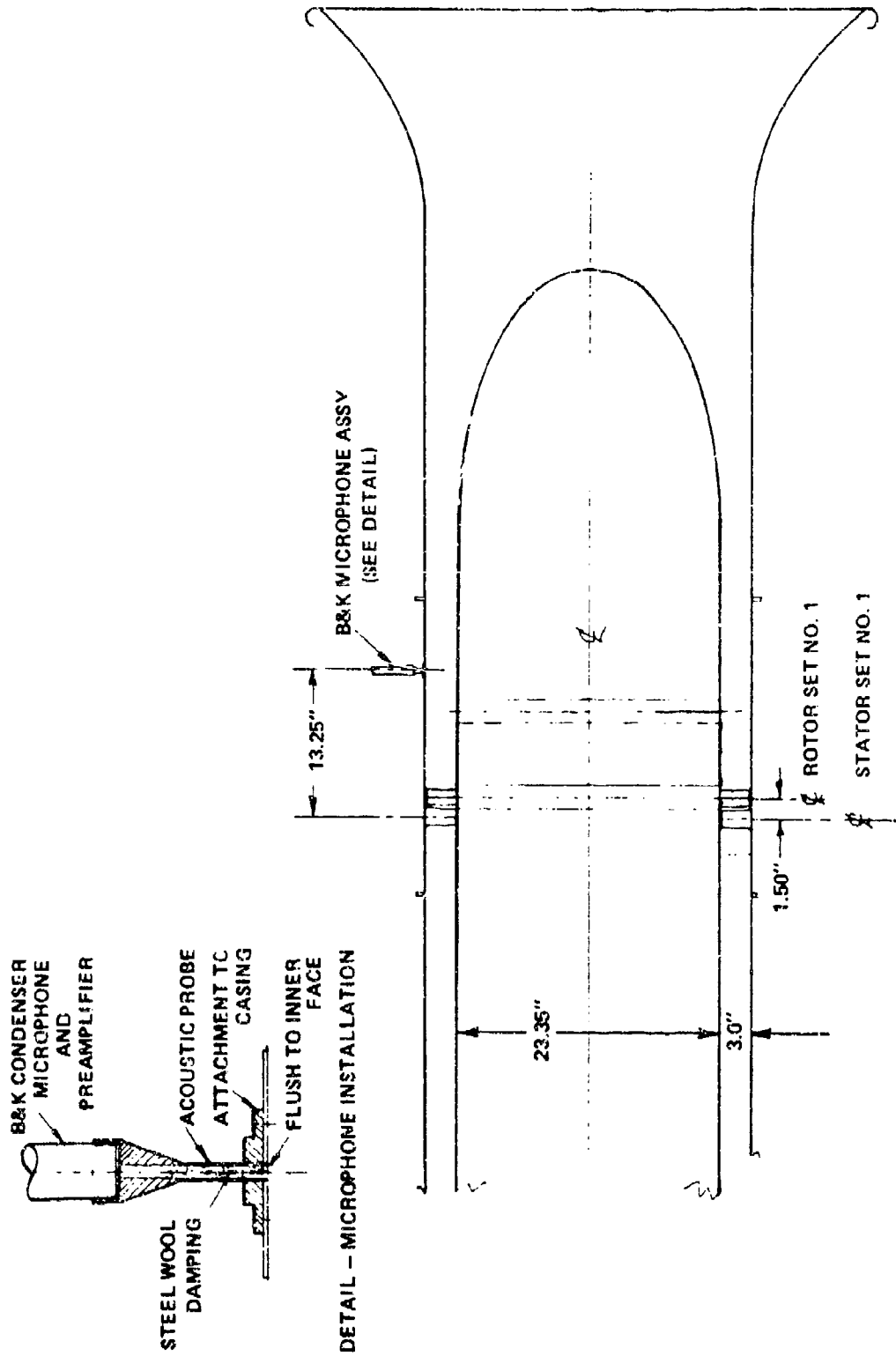
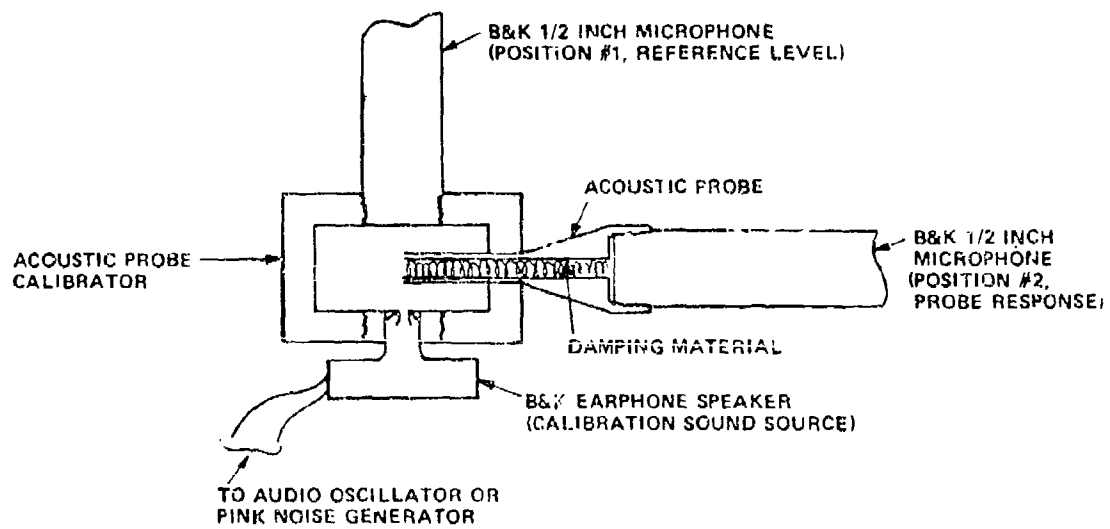


Figure 1 TEST CONFIGURATION FOR ACOUSTIC STUDIES OF ROTOR-STATOR INTERACTION



NOTE: WHEN MICROPHONE IS IN POSITION #1, A DUMMY MICROPHONE IS USED IN POSITION #2 AND VICE VERSA

Figure 2 SKETCH OF ACOUSTIC PROBE CALIBRATION APPARATUS

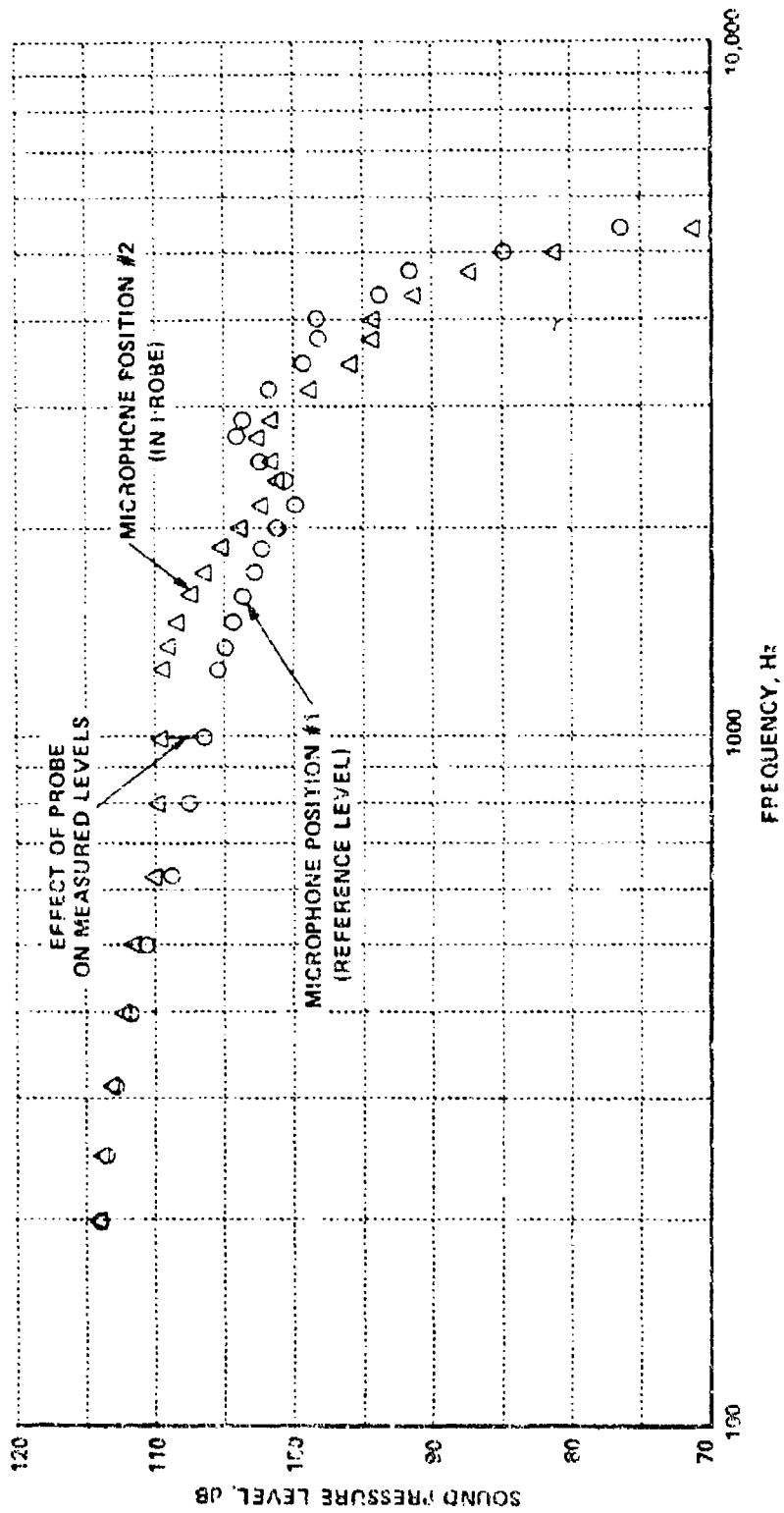


Figure 3 ACOUSTIC PROBE CALIBRATION RESULTS, PURE TONE EXCITATION

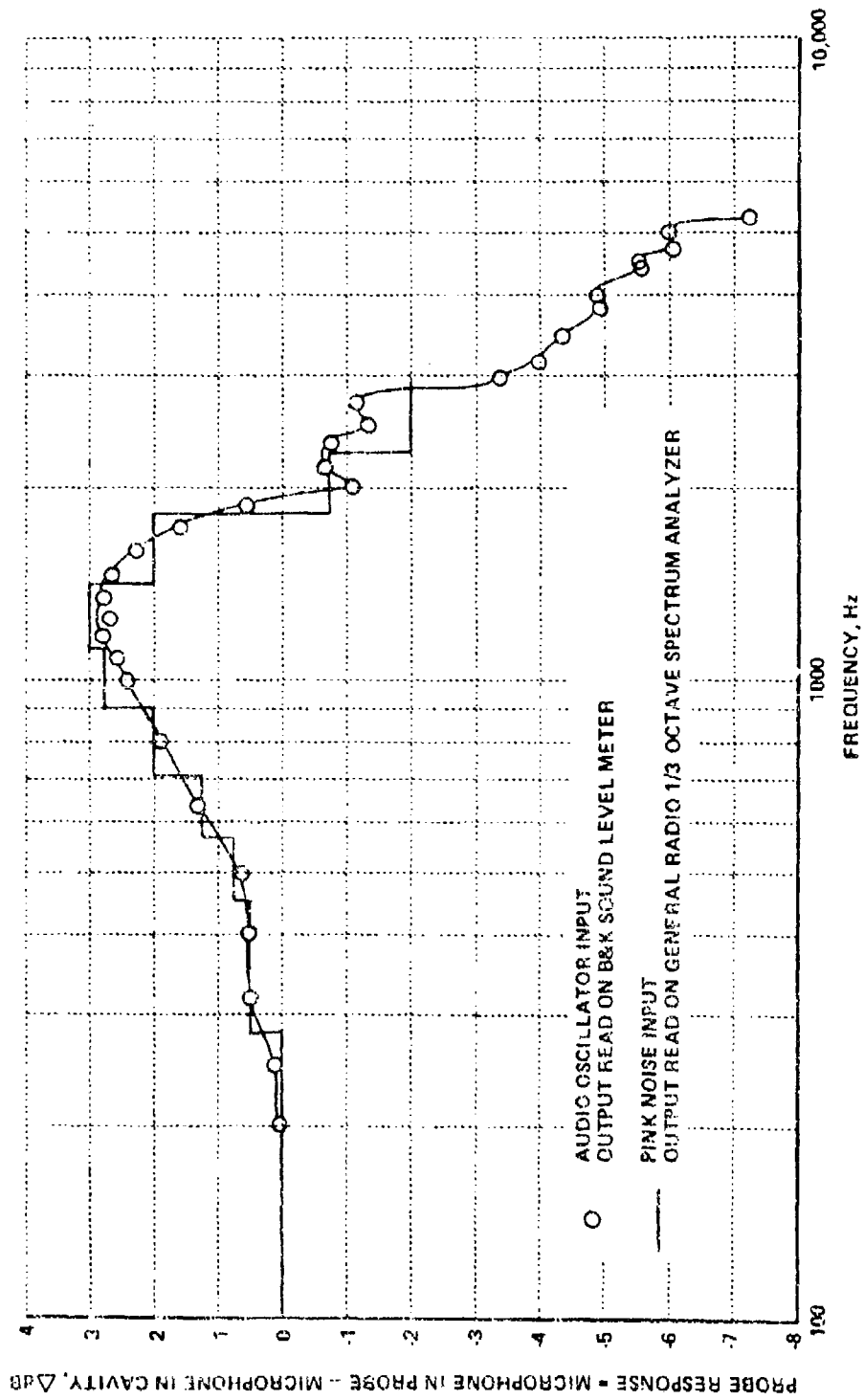
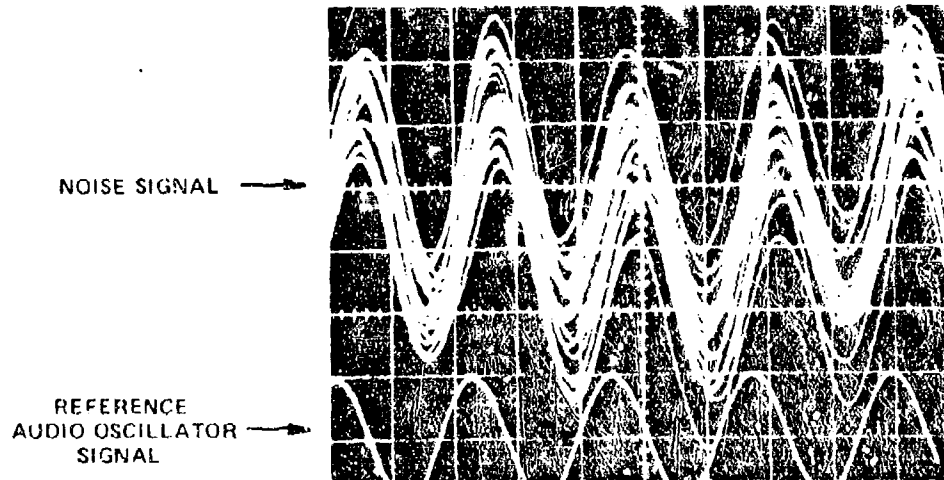


Figure 4 CALIBRATION OF MICROPHONE IN ACOUSTIC PROBE

ROTOR SET NO.1, ROTOR STAGGER ANGLE = 40.0 deg  
STATOR SET NO. 1, STATOR STAGGER ANGLE = 28.2 deg  
ROTOR RPM = 1435, AUDIO OSCILLATOR FREQUENCY = 4380 Hz



LISSAJOUS  
FIGURE FROM  
COMBINATION OF  
NOISE AND REFERENCE  
SIGNALS

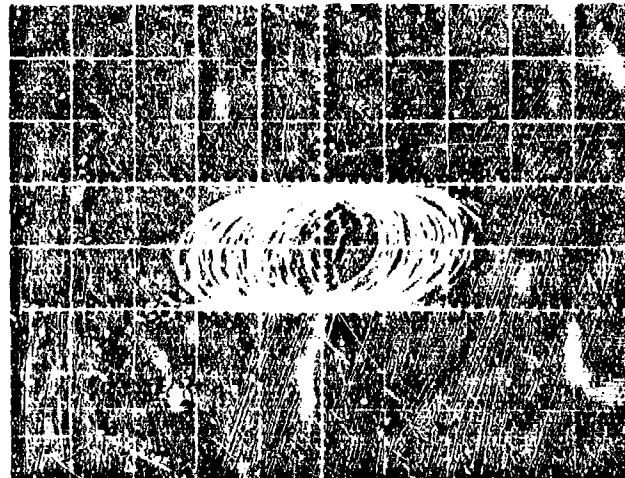


Figure 5 OSCILLOSCOPE RECORDS OF NOISE SIGNAL  
FROM ROTOR-STATOR INTERACTION

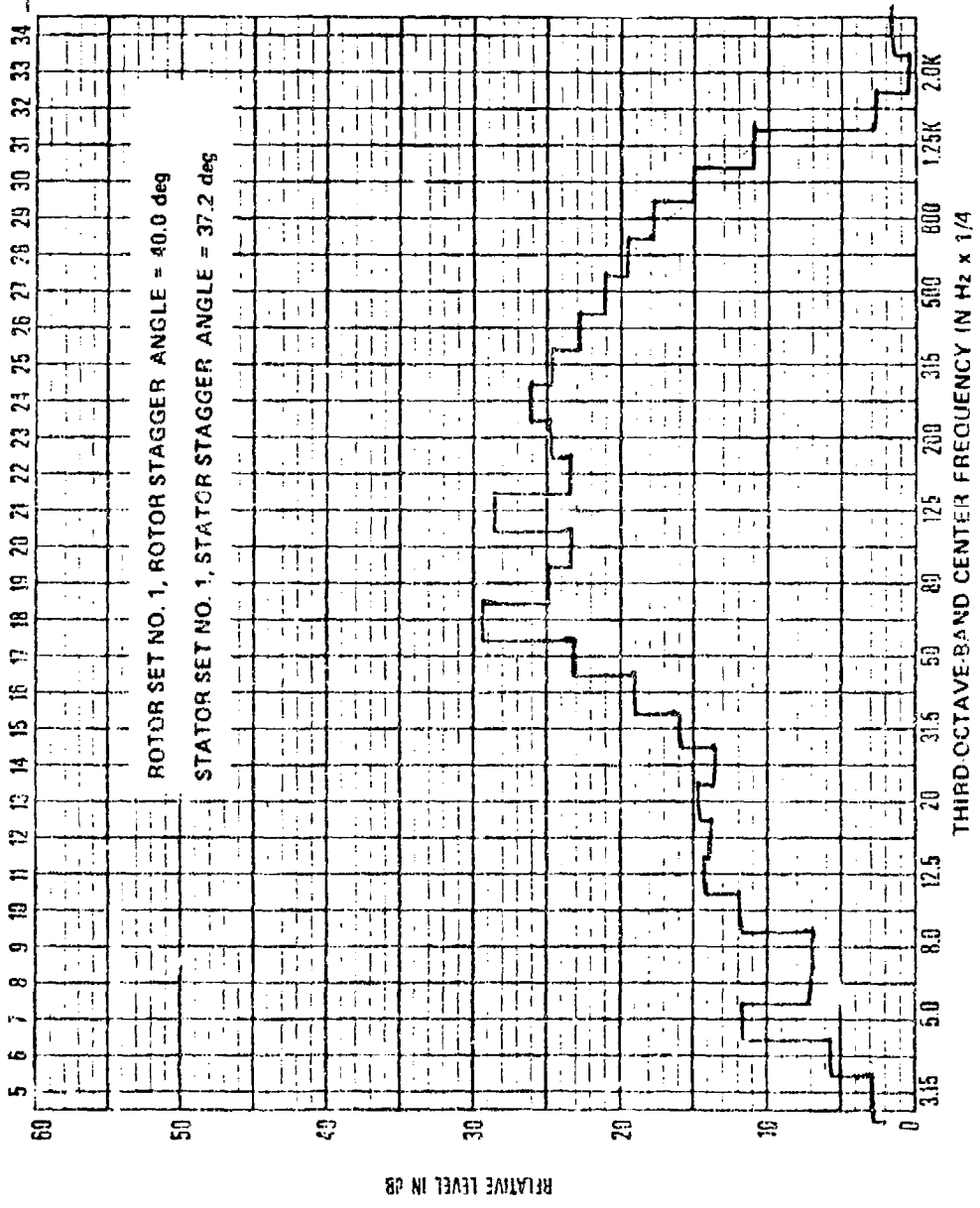
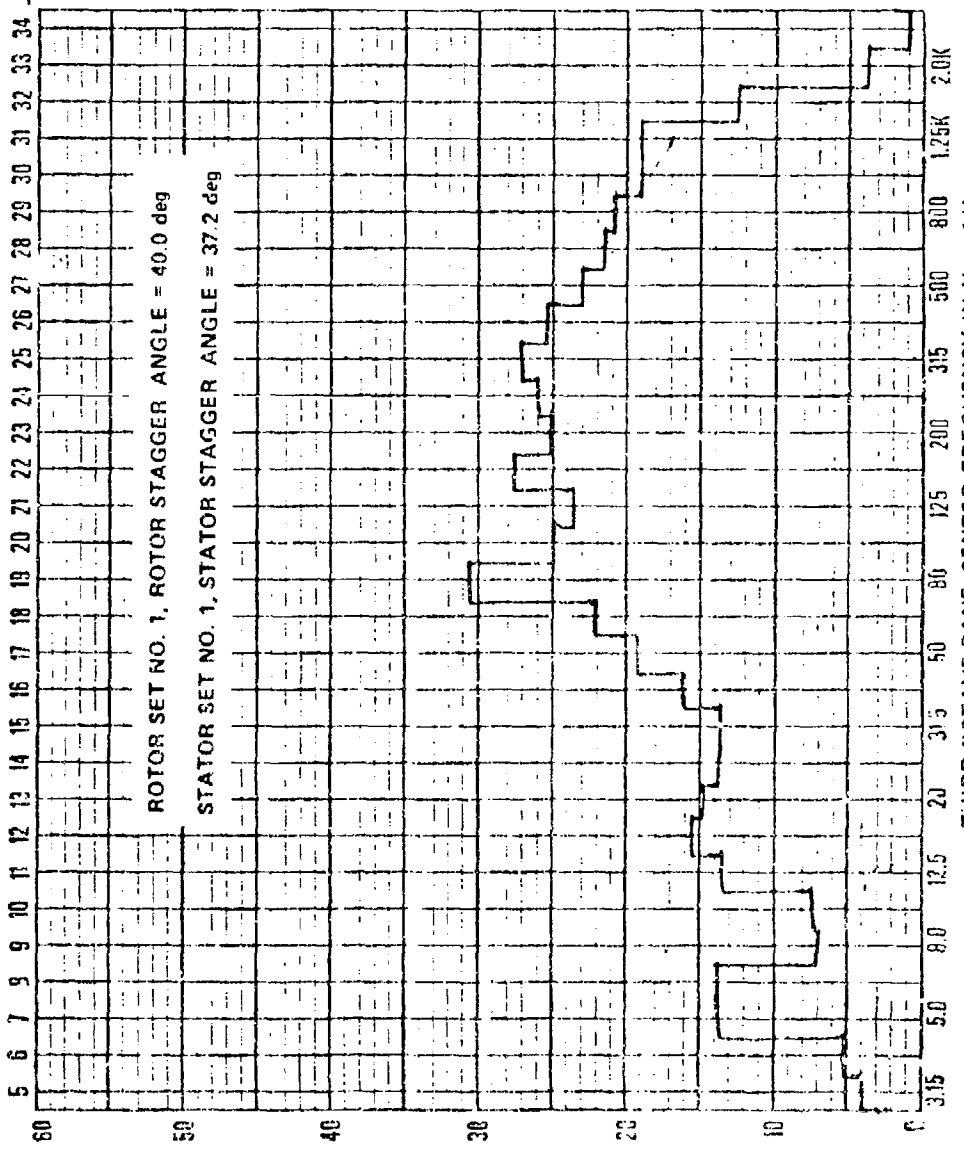


Figure 6 UNCORRECTED 1/3 OCTAVE SPECTRUM OF OUTER WALL SOUND PRESSURE LEVEL FROM ROTOR-STATOR INTERACTION



THIRD-OCTAVE  
-BAND NUMBER



INTEGRATION  
TIME

<input type="checkbox"/>	1/8	<input type="checkbox"/>	1	<input type="checkbox"/>	8
<input type="checkbox"/>	1/4	<input type="checkbox"/>	2	<input type="checkbox"/>	16
<input type="checkbox"/>	1/2	<input type="checkbox"/>	4	<input checked="" type="checkbox"/>	64
<input type="checkbox"/>		<input type="checkbox"/>		<input type="checkbox"/>	SEC

I.D. NO.  
2-18

ROTOR RPM = 1155

FOR  
ABSOLUTE  
LEVEL  
ADJ  
80 dB

Figure 6 (Cont.) UNCORRECTED 1/3 OCTAVE SPECTRUM OF OUTER WALL SOUND PRESSURE  
LEVEL FROM ROTOR-STATOR INTERACTION  
b) ROTOR RPM = 1155

RELATIVE LEVEL IN dB

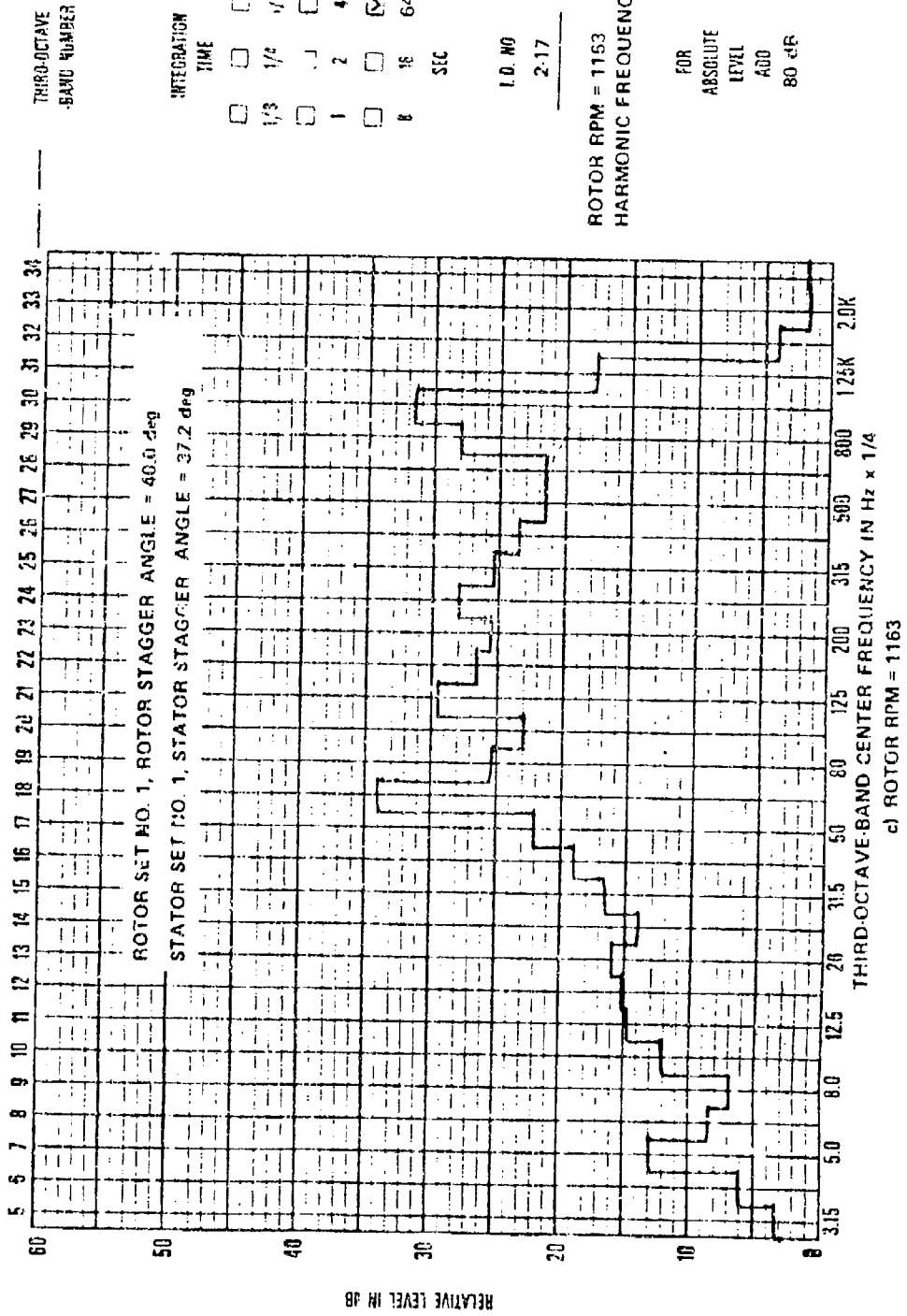


Figure 6 (Cont.) UNCORRECTED 1/3 OCTAVE SPECTRUM OF OUTER WALL SOUND PRESSURE LEVEL FROM ROTOR-STATOR INTERACTION

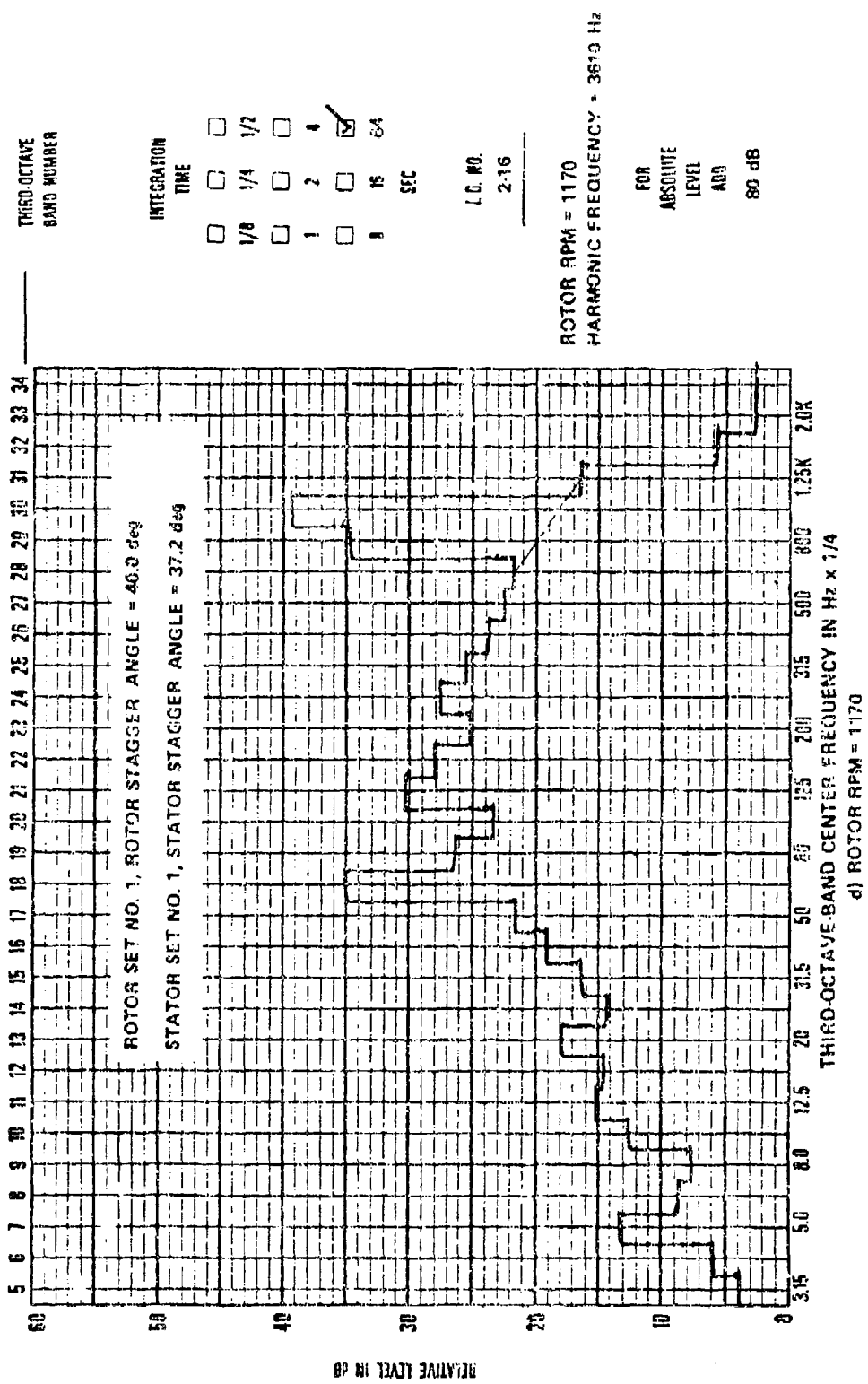


Figure 6 (Cont.): UNCORRECTED 1/3 OCTAVE SPECTRUM OF OUTER WALL SOUND PRESSURE LEVEL FROM ROTOR-STATOR INTERACTION

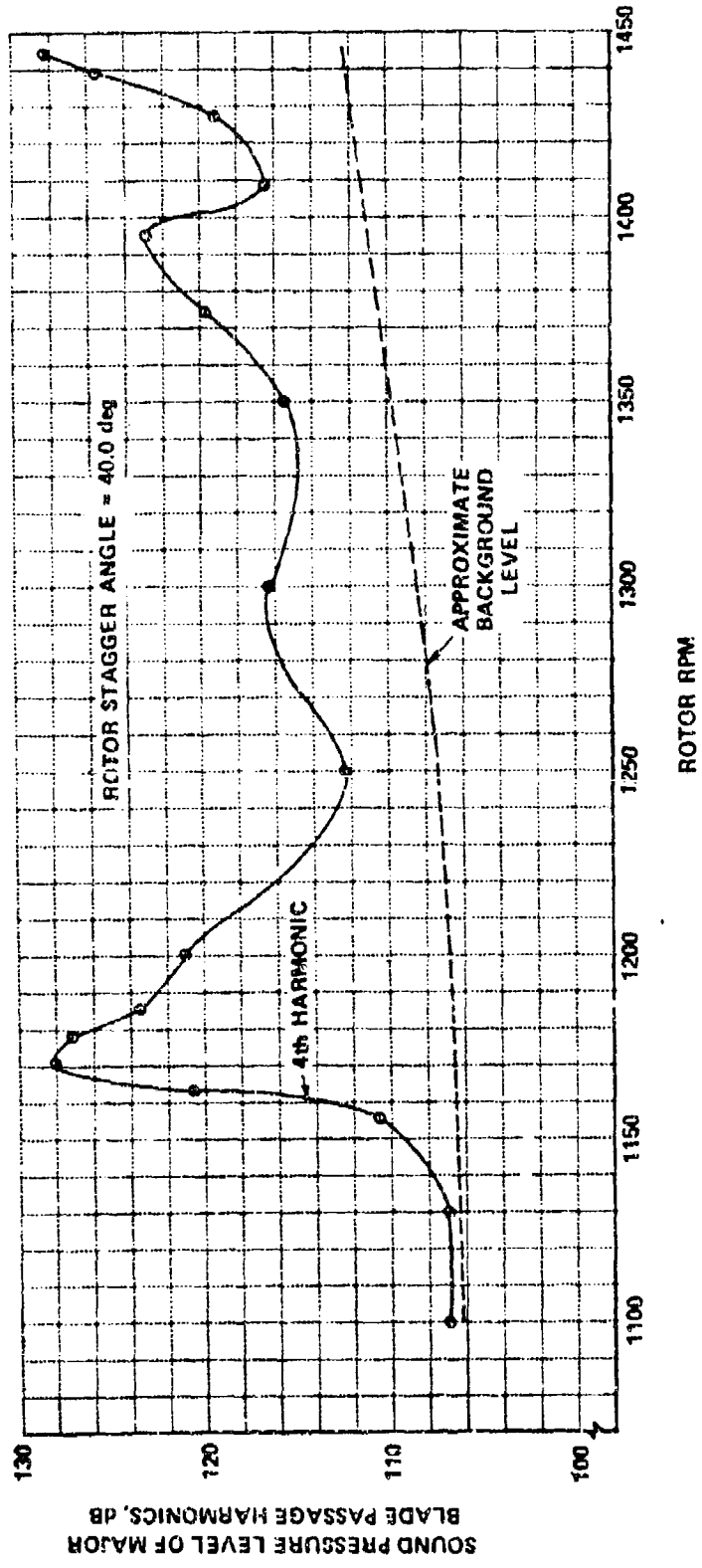


Figure 7 EXPERIMENTAL OUTER WALL SOUND PRESSURE LEVELS FROM ROTOR-STATOR INTERACTION, STATOR STAGGER ANGLE = 37.2 deg

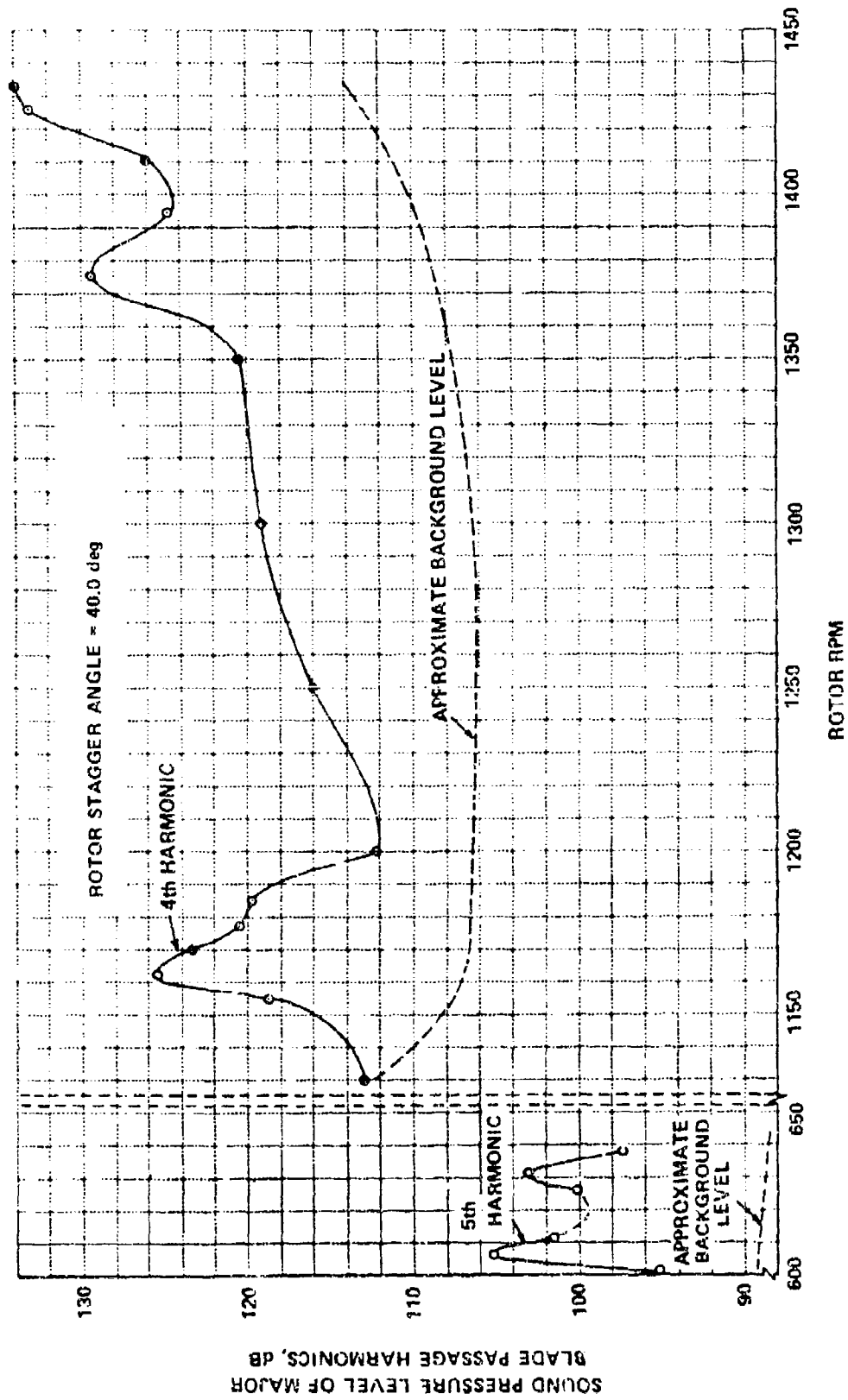
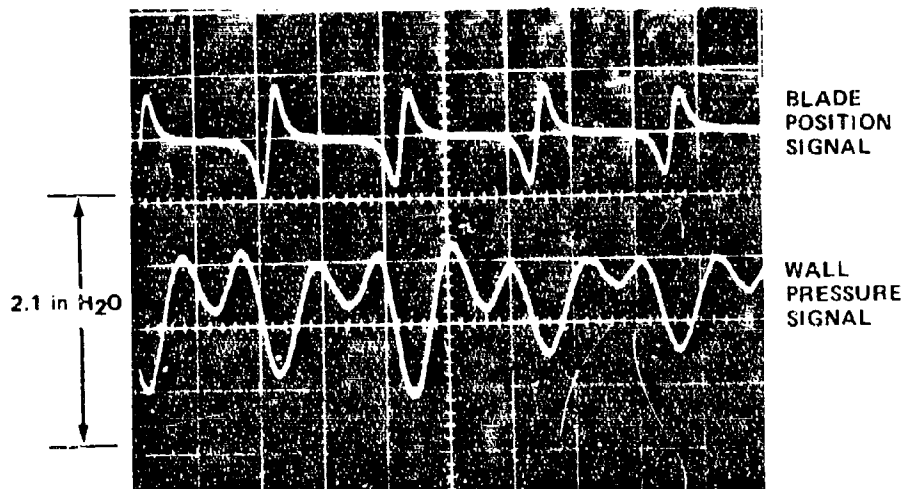
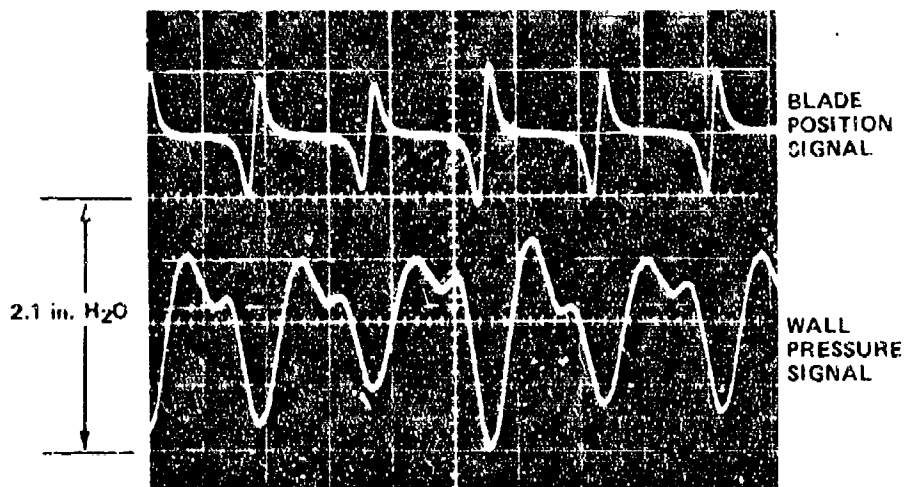
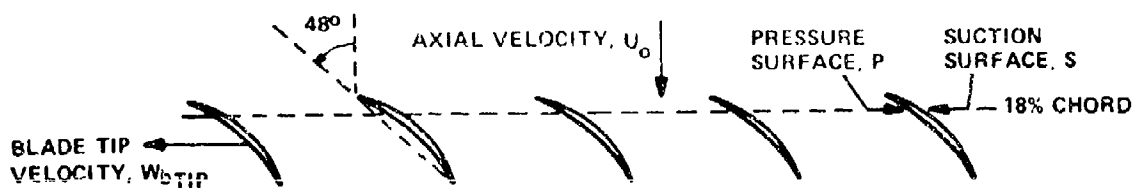


Figure 8 EXPERIMENTAL OUTER WALL SOUND PRESSURE LEVELS FROM ROTOR-STATOR INTERACTION, STATOR STAGGER ANGLE = 28.2 deg

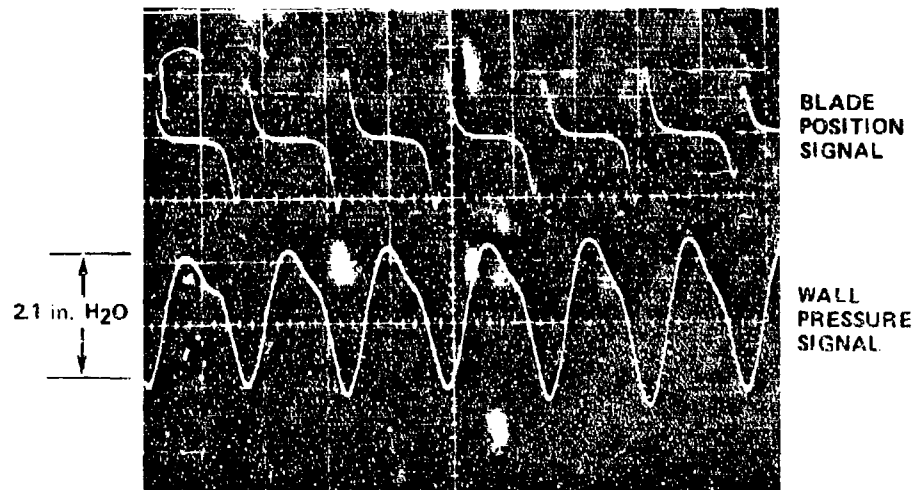


a) ROTOR RPM = 600, INLET SWIRL ANGLE,  $\beta_{1TIP} = 52.0$  deg

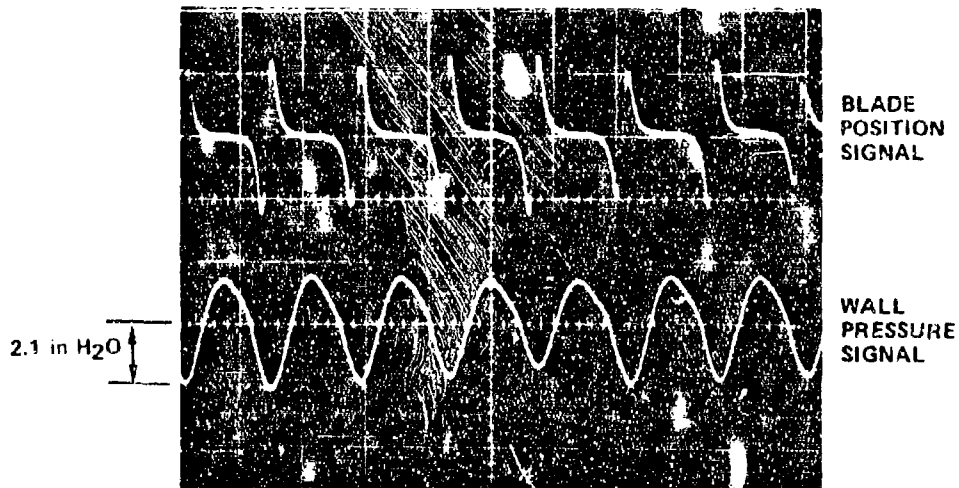
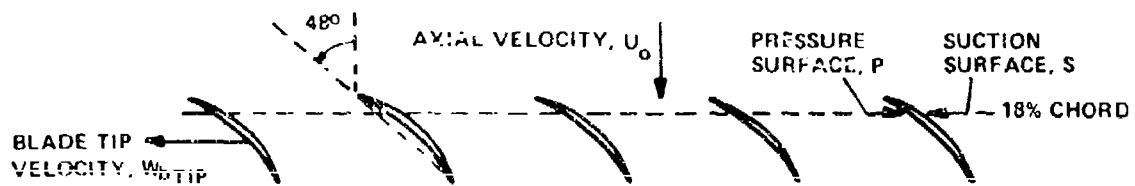


b) ROTOR RPM = 700, INLET SWIRL ANGLE,  $\beta_{1TIP} = 56.2$  deg

Figure 9 BLADE TIP PASSAGE PRESSURE SIGNALS ON ISOLATED ROTOR AT VARIOUS ROTOR SPEEDS, CHORDWISE LOCATION = 18%, AXIAL VELOCITY,  $U_0 = 60$  ft/sec



c) ROTOR RPM = 800, INLET SWIRL ANGLE,  $\beta_{1TIP} = 59.7 \text{ deg}$



d) ROTOR RPM = 900, INLET SWIRL ANGLE,  $\beta_{1TIP} = 62.5 \text{ deg}$

Figure 9 (Cont.) BLADE TIP PASSAGE PRESSURE SIGNALS ON ISOLATED ROTOR AT VARIOUS ROTOR SPEEDS, CHORDWISE LOCATION = 18%, AXIAL VELOCITY,  $U_0 = 60 \text{ ft/sec}$



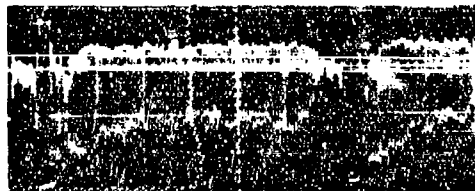
CHORDWISE LOCATION = 13%



CHORDWISE LOCATION = 18%



CHORDWISE LOCATION = 32%



CHORDWISE LOCATION = 49%



CHORDWISE LOCATION = 64%



CHORDWISE LOCATION = 79%

ROTOR RPM = 1000  
AXIAL VELOCITY,  $U_0 = 60$  ft/sec

2.1 in.  $H_2O$

20 milliseconds

Figure 10 BLADE TIP PASSAGE PRESSURE SIGNALS AT VARIOUS CHORDWISE LOCATIONS ON ISOLATED ROTOR DURING ROTATING STALL



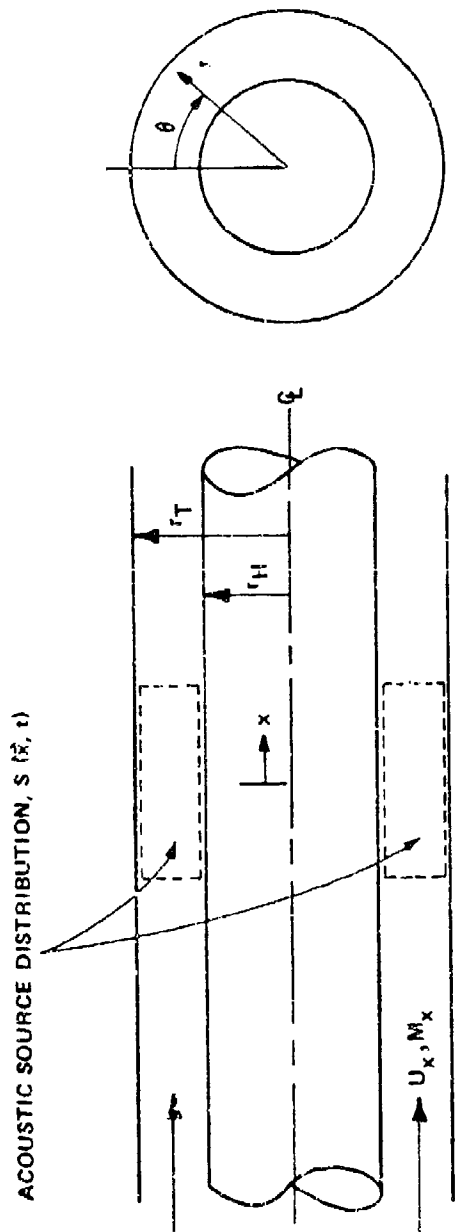


Figure 11 ACOUSTIC MODEL

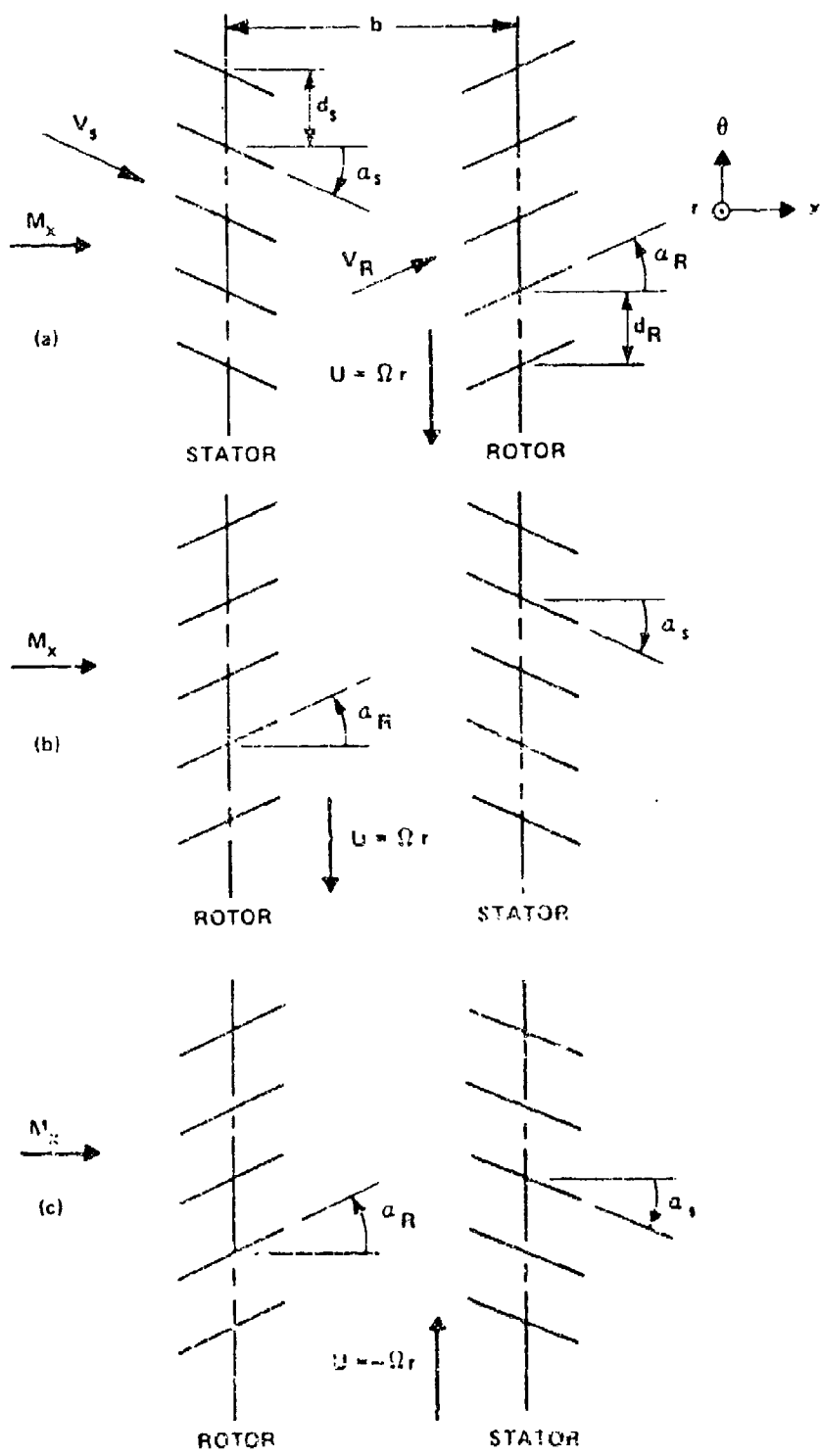
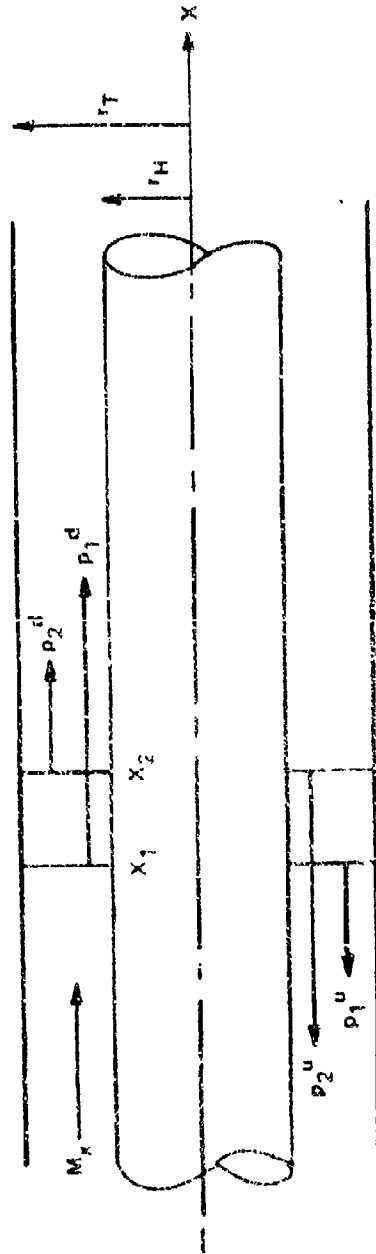


Figure 12 AERODYNAMIC MODEL



( )<sup>u,d</sup> DENOTES UPSTREAM, DOWNSTREAM PROPAGATING WAVE

( )<sub>1,2</sub> DENOTES WAVE GENERATED BY ROW AT  $X_1, X_2$

Figure 13 CLASSIFICATION OF PRESSURE WAVES

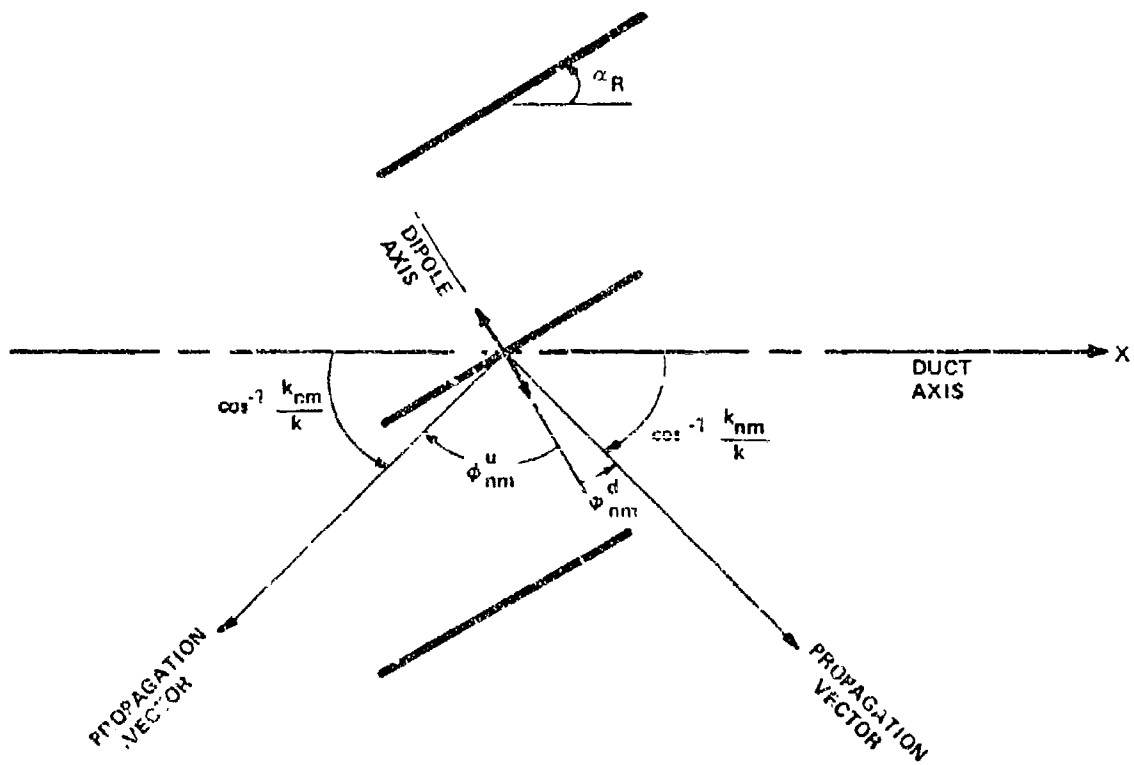


Figure 14 ASYMMETRY IN ANGULAR DEVIATION BETWEEN DIPOLE AXIS AND PROPAGATION VECTORS

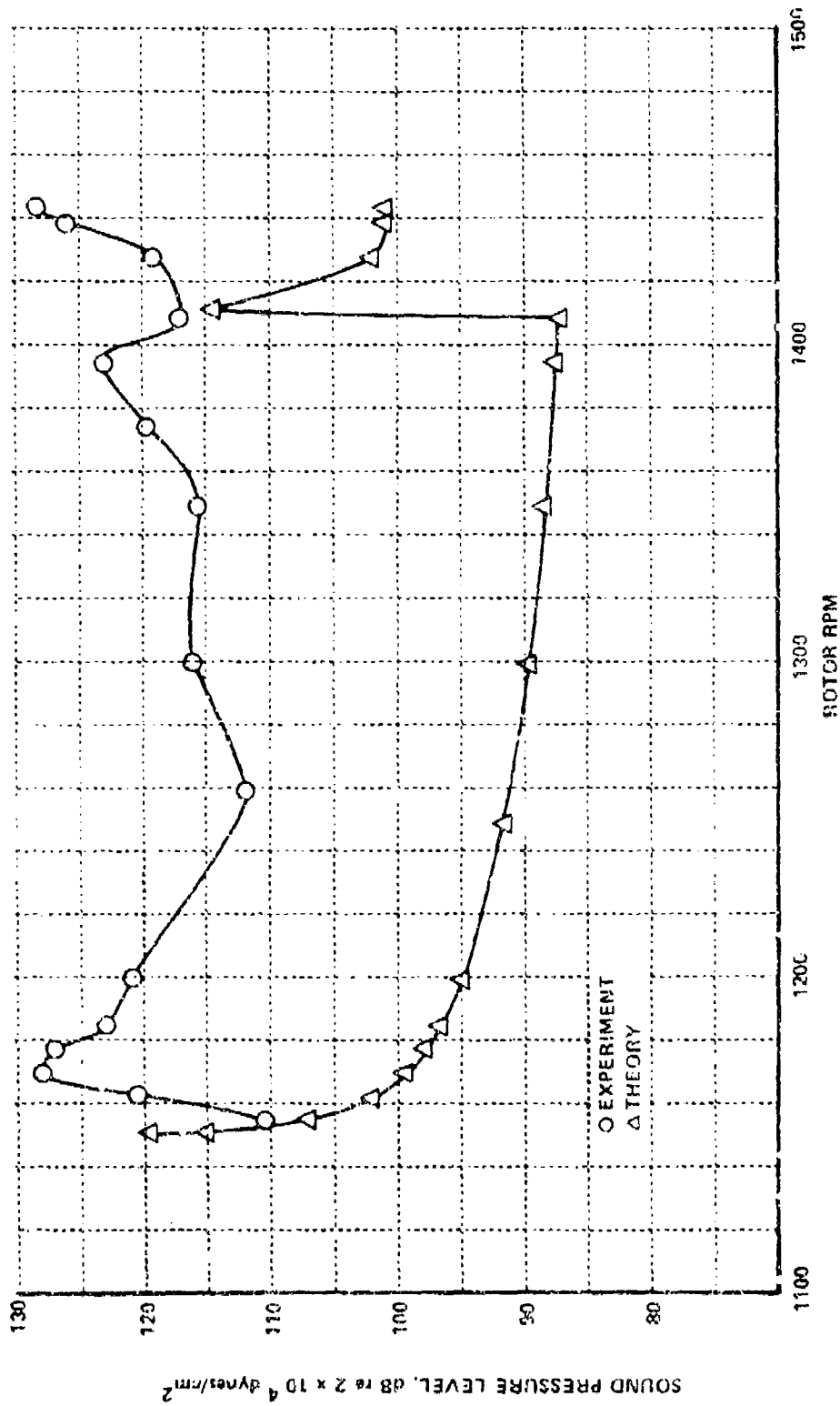


Figure 15 RMS WALL PRESSURE AT FOURTH HARMONIC OF BLADE PASSAGE FREQUENCY  
VS ROTOR RPM: MEAN STATOR STAGGER ANGLE = 37.2 DEG

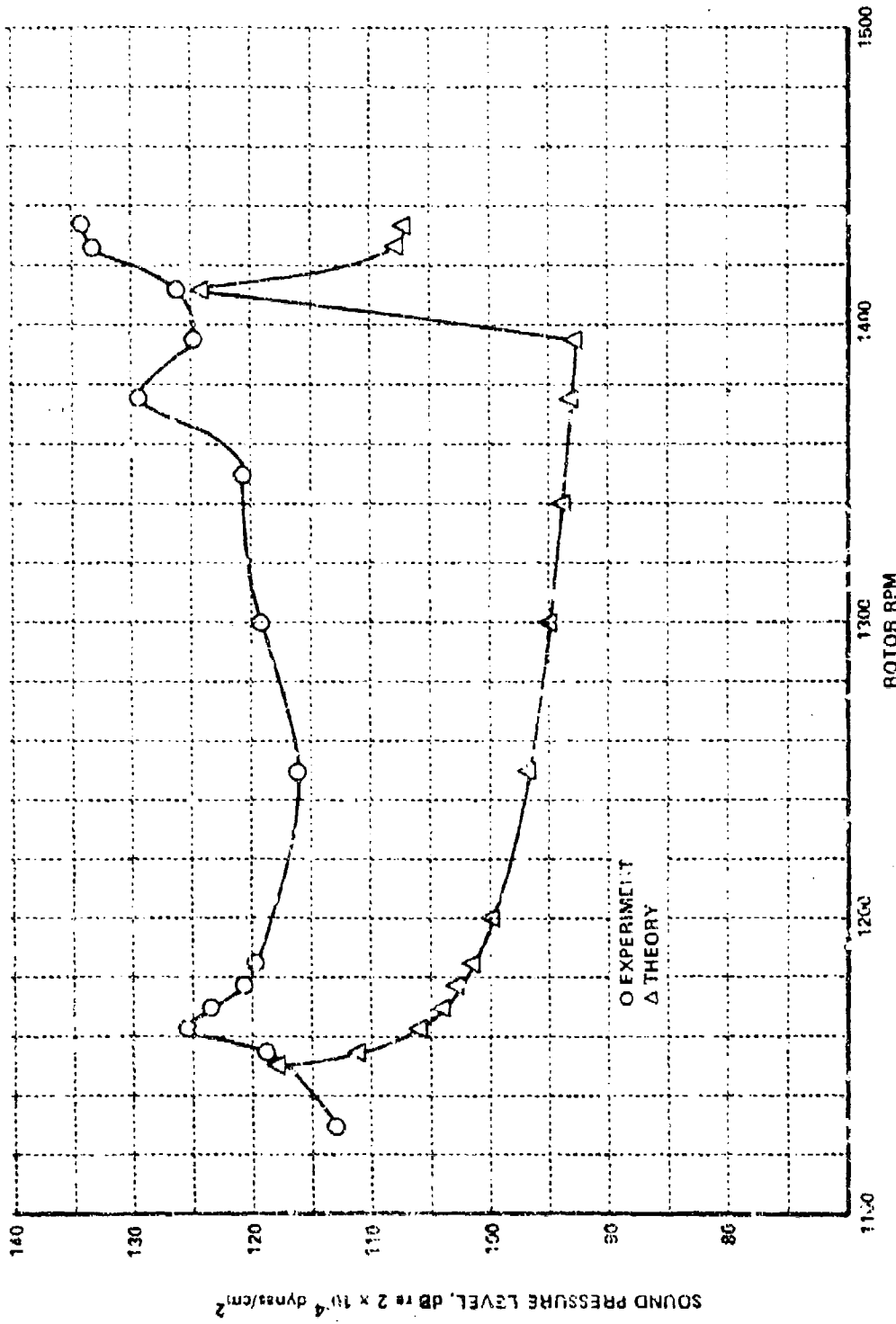


Figure 16 RMS WALL PRESSURE AT FOURTH HARMONIC OF BLADE PASSAGE FREQUENCY VS ROTOR RPM; MEAN STATOR STAGGER ANGLE = 28.2 DEG

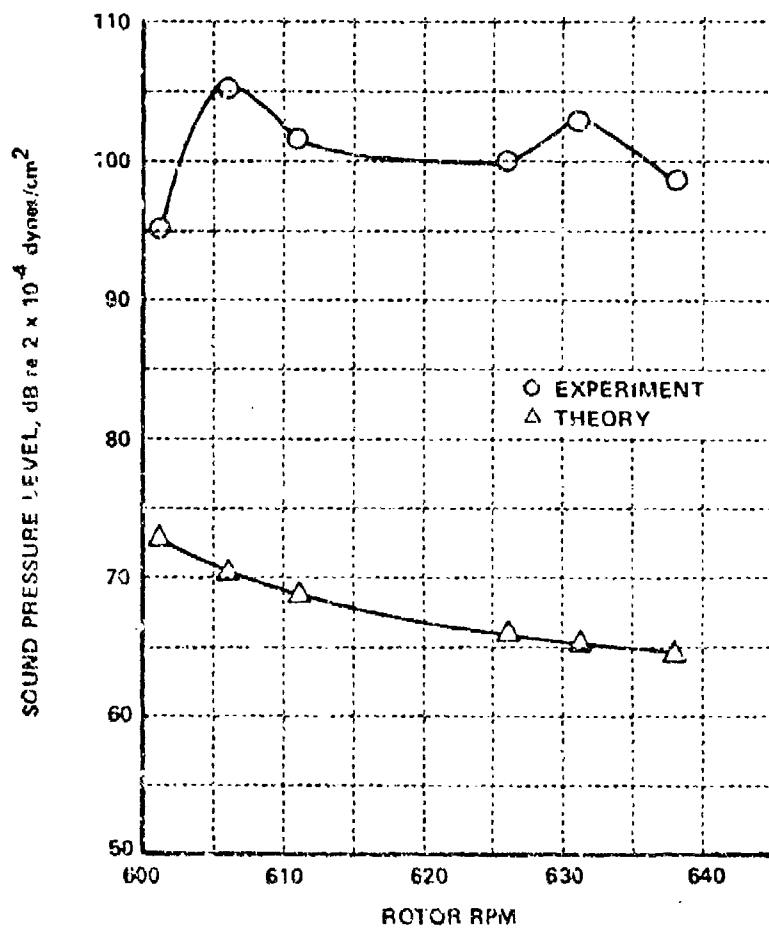


Figure 17 RMS WALL PRESSURE AT FIFTH HARMONIC OF BLADE PASSAGE FREQUENCY;  
MEAN STATOR STAGGER ANGLE = 28.2 DEG

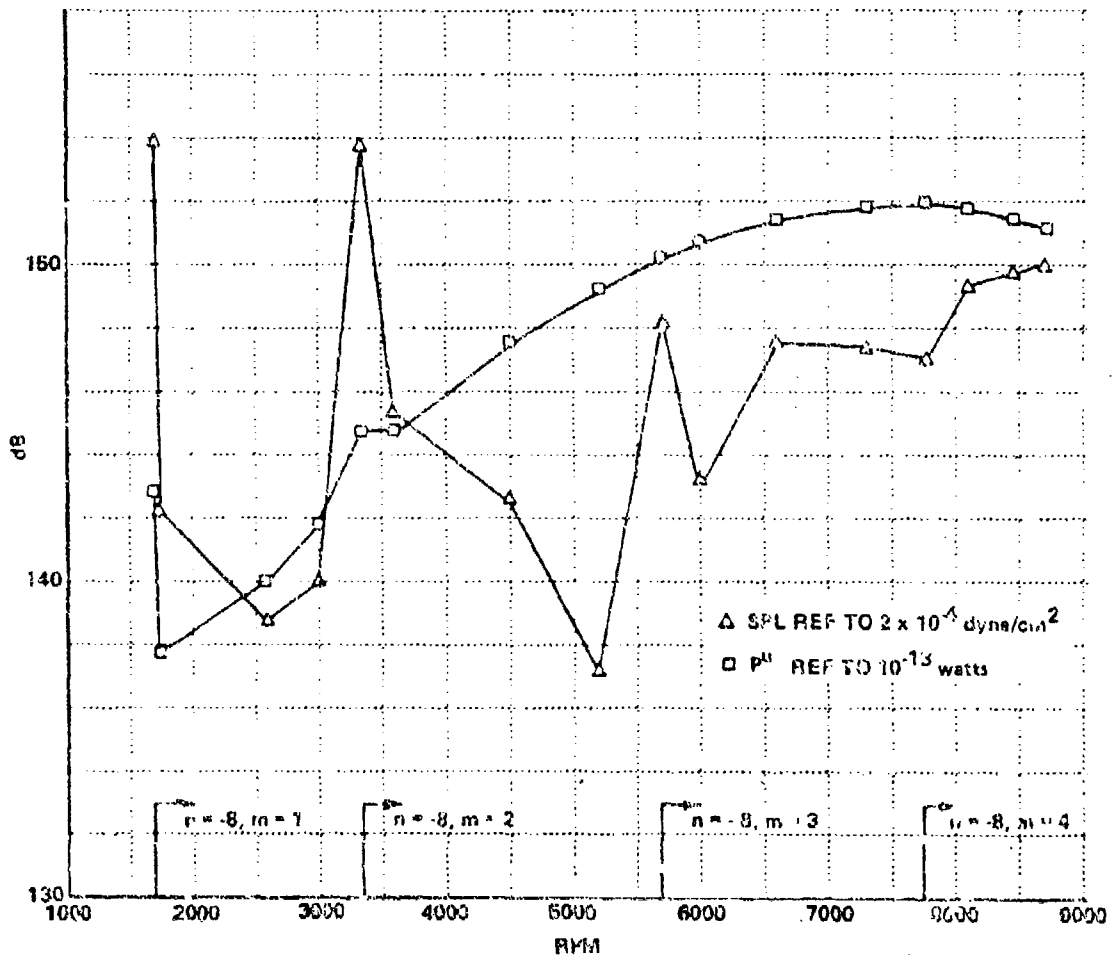


Figure 18 THEORETICAL SPL AND TOTAL RADIATED POWER AT BLADE PASSAGE FREQUENCY VERSUS ROTOR RPM; MEAN STATOR STAGGER ANGLE = 37.2 DEG



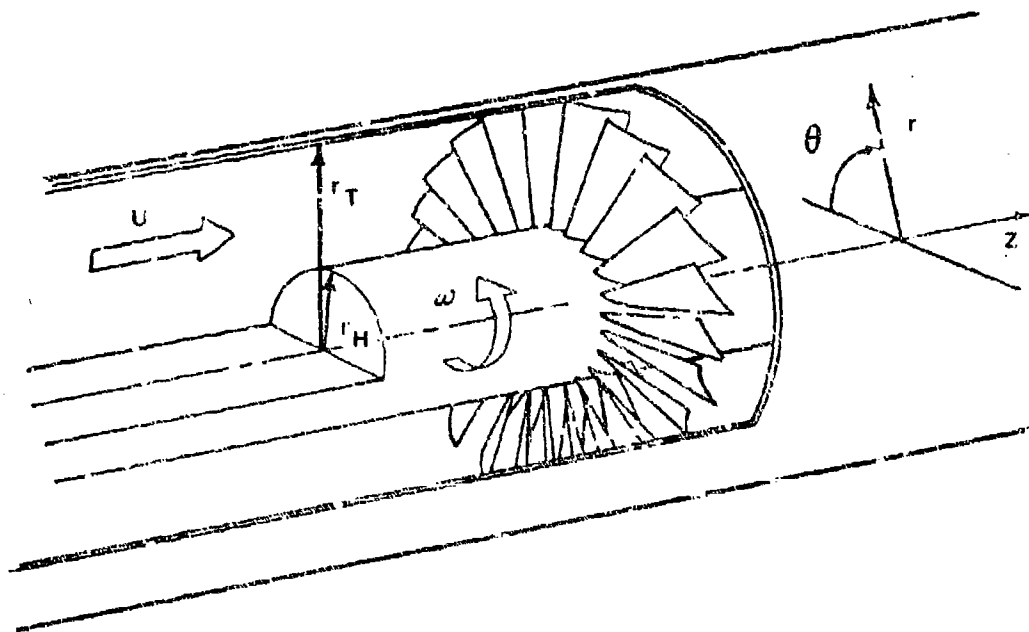


Figure 19 BLADE GEOMETRY AND BLADE-FIXED COORDINATE SYSTEM

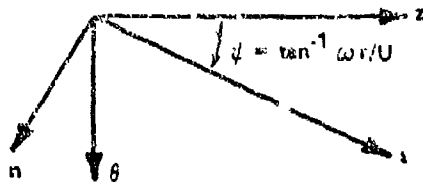
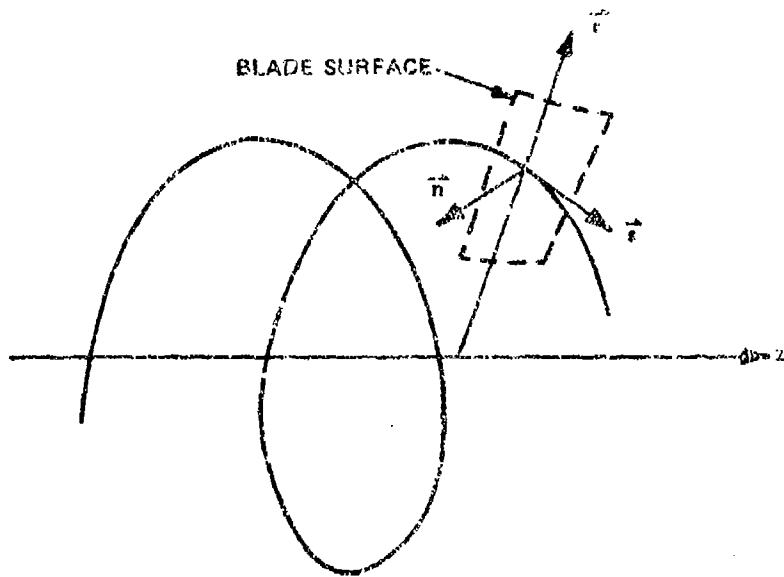


Figure 20 COORDINATE SYSTEM ALIGNED WITH UNDISTURBED FLOW DIRECTION

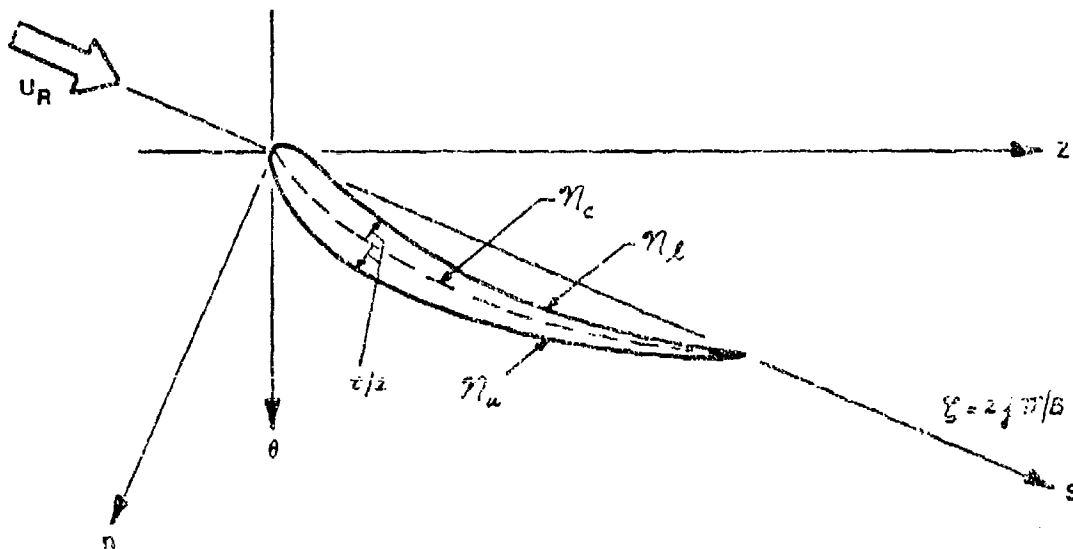


Figure 21 BLADE SURFACE GEOMETRY

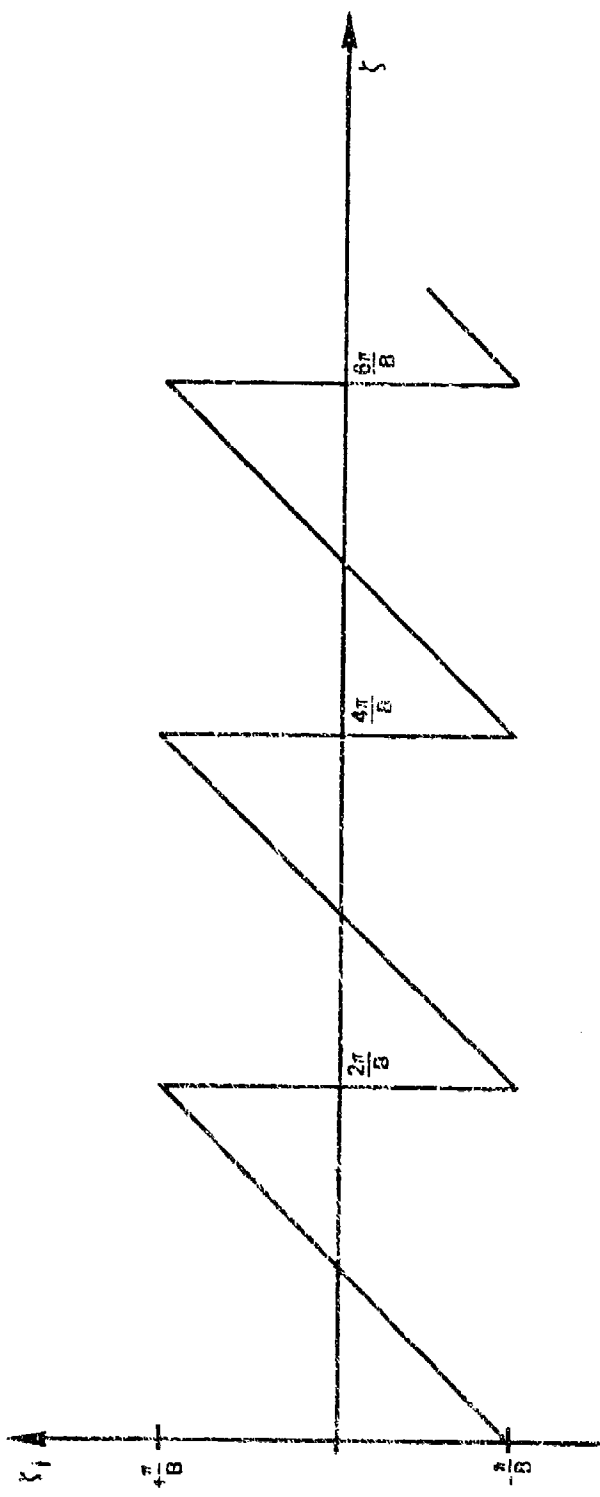


Figure 22 GENERALIZED FUNCTION,  $f_j$ , DEFINED BY EQ. (126)

## REFERENCES

1. Ludwig, G.R., Nenni, J.P. and Arendt, R.H., "Investigation of Rotating Stall in Axial Flow Compressors and the Development of a Prototype Rotating Stall Control System", AFAPL-TR-73-45, May 1973.
2. Kemp, N.H. and Sears, W.R., "Aerodynamic Interference Between Moving Blade Rows", J. of Aeronautical Sciences, Vol. 20, No. 9, 585-598, September 1953.
3. Kemp, N.H. and Sears, W.R., "The Unsteady Forces Due to Viscous Wakes in Turbomachines", J. of Aeronautical Sciences, Vol. 22, No. 7, 478-483, July 1955.
4. Tyler, J.M. and Sofrin, T.G., "Axial Flow Compressor Noise Studies", SAE Trans., Vol. 70, 309-332, 1962.
5. Morfey, C.L., "Rotating Pressure Patterns in Ducts: Their Generation and Transmission", J. Sound and Vibration, Vol. 1, 60-87, 1964.
6. Morfey, C.L., "Sound Transmission and Generation in Ducts with Flow", J. Sound and Vibration, Vol. 14, No. 1, 37-55, January 1971.
7. Hetherington, R., "Compressor Noise Generated by Fluctuating Lift Resulting from Rotor-Stator Interaction", AIAA Journal, Vol. 1, No. 2, 473-474, February 1963.
8. Crigler, J.L. and Copeland, W.L., "Noise Studies of Inlet Guide Vane-Rotor Interaction of a Single-Stage Axial-Flow Compressor", NASA TN D-2902, September 1965.
9. Hulse, B.T. and Large, J.B., "The Mechanisms of Noise Generation in a Compressor Model", ASME Transactions, J. Eng. for Power, Vol. 89A, No. 2, 191-198, April 1967.
10. Morfey, C.L., "Sound Generation in Subsonic Turbomachinery", ASME Trans., J. of Basic Eng., Vol. 92D, No. 3D, 450-458, September 1970.
11. Mani, R., "Discrete Frequency Noise Generation from an Axial Flow Fan Blade Row", ASME Trans., J. of Basic Eng., Vol. 92D, No. 1D, 37-43, March 1970.
12. Lipstein, M.J. and Mani, R., "Experimental Investigation of Discrete Frequency Noise Generated by Unsteady Blade Forces", ASME Transactions, J. of Basic Eng., Vol. 92D, No. 1, 155-164, March 1970.

13. Lowson, M.V., "Theoretical Studies of Compressor Noise", NASA CR-1287, March 1969.
14. Morfey, C.L., "Sound Generation in Subsonic Turbomachinery", ASME Paper 69-WA/FE-4, Presented at Winter Annual Meeting, Los Angeles, California, November 16-20, 1969.
15. Krishnappa, G., "Blade Interaction Noise from Lift Fans", J. Acoustical Society of America, Vol. 51, No. 5, 1464-1470, May 1972.
16. Abdelhamid, A.N., "Discrete Frequency Noise from Lifting Fans", ASME Transactions, J. Eng. for Power, Vol. 93A, No. 4A, 431-440, October 1971.
17. Dittmar, J.H., "Methods for Reducing Blade Passing Frequency Noise Generated by Rotor Wake-Stator Interaction", NASA TM X-2669, November 1972.
18. Cumpsty, N.A., "Tone Noise from Rotor/Stator Interactions in High Speed Fans", J. Sound and Vibration, Vol. 24, No. 3, 393-409, October 1972.
19. Clark, T.L., Ganz, U.W., Graf, G.A. and Westall, J.S., "Analytic Models of Ducted Turbomachinery Tone Noise Sources, Volume I: Analysis", NASA CR-132443, "Volume II: Subprogram Documentation", NASA CR-132444, "Volume III: Program Test Case Results", NASA CR-132445, May 1974.
20. Burdshall, E.A. and Urban, R.H., "Fan Compressor Noise: Prediction, Research and Reduction Studies", FAA-RD-71-73, February 1971.
21. Benzakein, M.J., Hochheiser, R.M., Claes, H.P., Kazin, S.B., Coward, W.E. and Knott, P.R., "Fan/Compressor Noise Research, Volume 1", FAA-RD-71-85, March 1972.
22. Kaji, S. and Okazaki, T., "Generation of Sound by Rotor-Stator Interaction", J. Sound and Vibration, Vol. 13, No. 5, 281-307, November 1970.
23. Mani, R., "Compressibility Effects in the Kemp-Sears Problem", presented at International Symposium on the Fluid Mechanics and Design of Turbomachinery, Penn. State Univ., September 1970.
24. Osborne, C., "Compressible Unsteady Interactions Between Blade Rows", AIAA J., Vol. 11, No. 3, 340-346, March 1973.
25. Whitehead, D.S., "Vibration and Sound Generation in a Cascade of Flat Plates in Subsonic Flow", Aeronautical Research Council, Great Britain, R & M 3685, February 1970.
26. Fleeter, S., "Fluctuating Lift and Moment Coefficients for Cascaded Airfoils in a Nonuniform Compressible Flow", Journal of Aircraft, Vol. 10, No. 2, 93-98, February 1973.

27. Osborne, C., "Unsteady Thin Airfoil Theory for Subsonic Flow", AIAA Journal, Vol. 11, No. 2, 205-209, February 1973.
28. McCune, J.E., "The Transonic Flow Field of an Axial Compressor Blade Row", Journal of the Aerospace Sciences, Vol. 25, No. 16, 616-626, October 1958.
29. Lighthill, M.J., "On Sound Generated Aerodynamically-I", Proceedings of the Royal Society (London), Vol. 211A, 564-587, March 1952.
30. Curle, N., "The Influence of Solid Boundaries Upon Aerodynamic Sound", Proceedings of the Royal Society (London), Vol. 231A, 503-514, September 1955.
31. Horlock, J.H., "Fluctuating Lift Forces on Aerofoils Moving Through Transverse and Chordwise Gusts", ASME Transactions, Journal of Basic Engineering, Vol. 90D, No. 11, 494-500, December 1968.
32. Horlock, J.H., Axial Flow Compressors: Fluid Mechanics and Thermodynamics, Butterworths, London, 1958.
33. Silverstein, A., Katzoff, S. and Bullivant, W.K., "Downwash and Wake Behind Plain and Flapped Airfoils", NACA TR 651, 1939.
34. Lieblein, S. and Roudebush, W.H., "Low-Speed Wake Characteristics of Two-Dimensional Cascade and Isolated Airfoil Sections", NACA TN 3771, 1956.
35. Raj, R. and Lakshminarayana, B., "Characteristics of the Wake Behind a Cascade of Airfoils", Journal of Fluid Mechanics, Vol. 61, No. 4, 707-730, December 1973.
36. Raj, R. and Lakshminarayana, B., "Three-Dimensional Characteristics of Turbulent Rotor Wakes Behind Rotors of Axial Flow Turbomachinery", ASME Paper 75-GT-1, ASME Gas Turbine Conference, Houston, Texas, March 2-6, 1975.
37. Amiet, R., "Effects of Compressibility in Unsteady Airfoil Lift Theories", Symposium on Unsteady Aerodynamics, University of Arizona, Tucson, Arizona, March 18-20, 1975.
38. Kemp, N.H., "Closed Form Lift and Moment for Osborne's Unsteady Thin Airfoil Theory", AIAA Journal, Vol. 11, No. 9, 1358-1360, September 1973.
39. Kemp, N.H. and Homicz, G.F., "Approximate Unsteady Thin-Airfoil Theory for Subsonic Flow", to be published in AIAA Journal.
40. Amiet, R., "Compressibility Effects in Unsteady Thin-Airfoil Theory", AIAA Journal, Vol. 12, No. 2, 252-255, February 1974.

41. McCune, J.E., "A Three-Dimensional Theory of Axial Compressor Blade Rows - Application in Subsonic and Supersonic Flows", J. of Aerospace Sciences, Vol. 25, No. 9, 544-560, September 1958.
42. Okurounmu, O. and McCune, J.E., "Three-Dimensional Vortex Theory of Axial Compressor Blade Rows at Subsonic and Transonic Speeds", AIAA Journal, Vol. 8, No. 7, 1275-1283, July 1970.
43. Okurounmu, O. and McCune, J.E., "Lifting Surface Theory of Axial Compressor Blade Rows" Part I - Subsonic Compressor", AIAA Journal, Vol. 12, No. 10, 1363-1371, October 1974. "Part II - Transonic Compressor", AIAA Journal, Vol. 12, No. 10, 1372-1380, October 1974.
44. Lordi, J.A., "Noise Generation by a Rotating Blade Row in an Infinite Annulus", AIAA Paper No. 71-617, AIAA 4th Fluid and Plasma Dynamic Conference, Palo Alto, California, June 21-23, 1971.
45. Lordi, J.A., "Report on a Study of Noise Generation by a Rotating Blade Row in an Infinite Annulus", U.S. Air Force Office of Scientific Research, Scientific Report AFOSR TR-71-4185 (also available as Calspan Report No. AI-2836-A-1), May 1971.
46. Erickson, J.C., Jr., Lordi, J.A. and Rae, W.J., "On the Transonic Aerodynamics of a Compressor Blade Row", Calspan Report No. AI-3003-A-1, October 1971.
47. McCune, J.E. and Dharwadkar, S.P., "Lifting-Line Theory for Subsonic Axial Compressor Rotors", MIT Gas Turbine Laboratory Report No. 110, July 1972.
48. Namba, M., "Small Disturbance Theory of Rotating Subsonic and Transonic Cascades", 1st International Symposium on Airbreathing Engines, Marseille, France, June 19-23, 1972.
49. Namba, M., "Lifting Surface Theory for a Rotating Subsonic or Transonic Blade Row", Aeronautical Research Council, Great Britain, R & M 3740, November 1972.
50. Wu, Chung-Hua, "A General Theory of Three-Dimensional Flow in Subsonic and Supersonic Turbomachines of Axial-, Radial-, and Mixed-Flow Types", NASA TN 2604, January 1952.
51. Morse, P.M. and Feshbach, H., Methods of Theoretical Physics, McGraw-Hill Book Company, Inc., New York, 1953, Chapt. 7.
52. Reissner, H., "On the Vortex Theory of the Screw Propeller", J. Aeronautical Sciences, Vol. 5, No. 1, 1-7, November 1937.
53. Landahl, M., "Pressure Loading Functions for Oscillating Wings with Control Surfaces", AIAA Journal, Vol. 6, No. 2, 345-348, February 1968.



54. Mangler, K.W., "Improper Integrals in Theoretical Aerodynamics", Aeronautical Research Council C.P. 94, Great Britain, June 1951.
55. Woodcock, D.L., "A Comparison of Methods Used in Lifting Surface Theory, Supplement to the Manual on Aeroelasticity Part VI", AGARD Report 583, June 1971.
56. Landahl, M.T. and Stark, V.J.E., "Numerical Lifting Surface Theory - Problems and Progress", AIAA Journal, Vol. 6, No. 11, 2049-2060, November 1968.
57. Hildebrand, F.S., Methods of Applied Mathematics, 2nd Ed. Prentice-Hall, Englewood Cliffs, New Jersey, 1965, Chapt. 3.
58. Albano, E. and Rodden, W.P., "A Doublet-Lattice Method for Calculating Lift Distributions on Oscillating Surfaces in Subsonic Flow", AIAA Journal, Vol. 7, No. 2, 279-284, February 1969.
59. Watson, G.N., A Treatise On the Theory of Bessel Functions, 2nd Ed., Cambridge University Press, London, 1966.
60. Langan, T.L. and Wang, H.T., "Evaluation of Lifting Surface Programs for Computing the Pressure Distribution on Planar Wings in Steady Motion", Computers and Fluids, Vol. 2, No. 1, 53-78, March 1974.
61. Shames, I.H., Mechanics of Fluids, McGraw-Hill Book Company, Inc., New York, 1962, Chapt. 5.